Technical University of Munich
TUM School of Computation, Information and Technology

TM

# Fiber Bragg Grating Sensors for High Temperature Metal Casting and Health Monitoring of Metal Structures

Qiang Bian

Complete reprint of the dissertation approved by the TUM School of Computation,

Information and Technology of the Technical University of Munich for the award of the

Doktor der Ingenieurwissenschaften (Dr.-Ing.).

Chair:            Prof. Dr.-Ing. Norbert Hanik

Examiners:

    1.    Prof. Dr.-Ing. habil. Dr. h.c. A. W. Koch
    2.    Prof. Dr. rer.nat. Johannes Roths

The dissertation was submitted to the Technical University of Munich on 03.04.2023 and

accepted by the TUM School of Computation, Information and Technology on 21.09.2023.

# Contents

# Chapter 1

# Introduction

## 1.1  Motivation

In casting, to obtain high quality cast parts with reduced residual stresses, high fatigue strengths, and longer life cycles, critical in-situ information like temperature and strain is needed for optimizing the casting processes. Considering the high temperatures involved during casting processes, the typical temperature measurement method in casting uses thermocouples [1], which normally can only achieve single-point sensing. For temperature distribution measurement, several thermocouples with separate lead heads need to be deployed [2], which largely increases the complexity of the measurement system and might introduce huge disturbances during the casting and cooling process. In-situ strain information during casting is in general the basis for the calculation of residual stress and the traditional mechanical methods, which are mainly based on removal of partial material from the cast part, like hole-drilling [3], are destructive and can not achieve real-time measurement during casting. Nondestructive measurement methods like neutron diffraction has been reported for in-situ strain measurement during casting [4, 5], but they suffer from the drawbacks of poor time resolution, the difficulty of equipment mobility, and lower data reliability at temperatures higher than the solidus temperature [6]. Fiber Bragg gratings (FBGs) have been used to monitor temperature and strain during the aluminum casting [7, 8], whose highest temperature is ∼650 °C. Whereas, other metal materials with higher melting points and cast temperatures, for example, copper and steel, remain to be challenging.

The structure and properties of a metal cast are largely dependent on the solidification characteristics during the casting process. For example, the rigidity point, as one of the solidification characteristics, is a significant input parameter in solidification numerical

modeling because it indicates the temperature when thermal-induced deformations introduce internal stresses/forces during casting processes and it can be used in studying the cast defects such as solidification cracking [5]. Many approaches have been proposed to study the solidification characteristics of metal alloys. The traditional method is the thermal analysis technique using one or two thermocouples to record the temperature and to recognize the solidification characteristics from the cooling curve and its first/second derivative curves [9–11]. A mechanical method, also called rheological method, was applied to detect the rigidity point by using rotation impeller/rheometer to record the torque during casting processes [11, 12]. A X-ray microtomography method was introduced to obtain the points when dendrites nucleated and eutectic reaction happened by investigating the microstructural evolution of aluminum alloy during solidification [13]. An in-situ neutron diffraction method has also been reported to determine the rigidity point and the dendrite coherency point [14]. However, those above-mentioned methods mainly focus on one-point measurement, while several thermocouples are needed when measuring multi-point temperatures. Therefore, some new methods and new perspectives are needed to study the solidification properties at different positions during a casting process.

Structural health monitoring (SHM) will become a key issue in construction engineering and civil infrastructure safety. By monitoring the changes to materials and the geometric properties of structures such as bridges, pipelines and buildings, early warning of hazards can be achieved. Compared with those surface-attached sensors and nondestructive methods, embedded sensors can provide in-situ information at some critical locations from inside the structure in real time with a compact sensing system. Optical fiber sensors (OFSs) embedded in composite structures have been widely investigated in the past ten years [15–18], especially in the field of reinforced laminates [19]. For metallic structures, however, the embedding process is more challenging due to the much higher melting points of metals and the large mismatch of material properties. In addition to the laser-based embedding method [20–22] and the ultrasonic consolidation method [23, 24], the casting process has also been proposed to embed fiber sensors into metals [25]. The advantages of the casting method are obvious: Mass manufacturing is possible with the casting process, and those structures with complex and large shapes needed in the industry, like turbines and engines, can be fabricated. By placing the fiber sensors in advance into the right position of the cast model, these sensors can be easily embedded deeply inside metallic structures. Previous research has demonstrated that, with the casting processes, bare optical fibers can be embedded into aluminum [7]. Heilmeier et al. carried out tensile tests using aluminum cast specimens with embedded FBG strain sensors [26] and evaluated the strain transition properties between fibers and the cast parts by neutron diffraction [27]. Lindner et al. investigated the strain and temperature response of fiber embedded cast parts [28]. Apart from aluminum, however, optical fibers

have not been successfully embedded in other metallic materials, let alone a detailed study of their properties. Besides, how to decouple temperature and external strain in metallic structures is still a challenge. OFSs like FBGs are normally sensitive to both temperature and strain, so measures should be applied to distinguish between these two parameters when fibers are embedded into structures. To date, although some researches studied the temperature and strain behaviors of the embedded OFSs [29] or measured temperature and strain using OFSs, which were not fully surrounded by metals but epoxy glue [30], few researches related to temperature and strain decoupling of OFSs embedded in metallic structures have been reported [31].

The high temperature resistance of Type-I FBG is relatively low with its reflectivity showing a significant decay at temperatures over 200 °C [32], which limits its application prospect at high temperatures. High-temperature resistant FBGs like Type-II FBG, regenerated FBG (RFBG), and sapphire fiber Bragg grating (SFBG) have been proposed for sensing in the high-temperature environments over the past few decades. However, there are still several challenges existing when using those high-temperature resistant FBGs. For example, even though the grating strengths of RFBGs do not drop significantly at high temperatures, their Bragg wavelengths suffer from slow wavelength drifts when they are exposed to high temperatures over long time periods, affecting the long-term functionality of the sensors [33]. To date, there is no comprehensive theory that can explain all the drift behaviors, and the factors that affect the drift rates still need to be studied. In addition, in some harsh environments like casting, due to the high temperature and large compression involved [7, 8], it is necessary to use some optical fibers with better robustness for high-temperature resistant FBGs. For SFBGs, the most widely used demodulation system is based on multimode fibers [34], which seriously affects the measurement stability and accuracy, the number of multiplexing, and the adaptability to commonly used single-mode demodulation equipments. Besides, there is no detailed comparative study of silica fiber-based FBGs and SFBGs, so the differences between them and their respective strengths and weaknesses are still unclear.

## 1.2 Goal of thesis

In this work, the first task was to study the characteristics of high-temperature resistant FBGs, especially RFBGs. Large mode area (LMA) fibers with lower dopant concentration were used for RFBG fabrication so how the lower dopant concentration influenced generally the temperature sensitivity, drift rate, and long-term stability of RFBGs could be revealed. A comparative study of RFBGs and a SFBG was carried out to figure out the difference between the gratings fabricated on silica fibers and sapphire fibers, and

their respective strengths and weaknesses for high-temperature sensing.

The second task was to use RFBG sensors to monitor the casting process of aluminum alloy. The temperature and strain evolutions as well as distributions during casting processes were studied. The strain behaviors were compared with the typical solidification phases reported by the traditional monitoring methods to check whether the fiber optic smart casting method could provide a new perspective to investigate the casting process. Besides, casting monitoring was extended from aluminum to copper, with the maximum temperature increasing from 650 ℃ to 1100 ℃.

The third task was to achieve SHM of metal structures using embedded FBG sensors. A series of temperature and strain experiments were carried out using FBG sensors embedded in the structures made of aluminum alloys and copper alloys. Temperature response experiments and tensile tests were carried out respectively to better know the interaction between the embedded fibers and the surrounding alloys. A temperature and strain decoupling method was studied to achieve temperature and strain monitoring of the metal structure at the same time.

# Chapter 2

# Fundamentals

## 2.1 Optical fiber

### 2.1.1 Silica fiber

**Fiber structure and waveguide theory**

An optical fiber is a cylindrical dielectric light waveguide that can confine the electromagnetic wave in the form of light to achieve low-loss transmission based on the principle of total reflection. The basic structure of an optical fiber is a two-layer cylindrical made of silica-based medium, which consists of an inner core and a surrounding cladding [35]. The refractive index of the fiber core $n_{core}$ is slightly higher than that of the fiber cladding $n_{clad}$. This refractive index difference can be achieved by doping the fiber core with germanium dioxide ($GeO_2$) or aluminum oxide ($Al_2O_3$) to increase $n_{core}$, or doping the fiber cladding with fluorine or boron trioxide ($B_2O_3$) to decrease $n_{clad}$. In general, outside cladding, the optical fiber is coated by a buffer protecting it from moisture and physical damage. The coating material is usually UV-cured urethane acrylate composite or polyimide materials [36]. Fig. 2.1(a) shows the schematic diagram of an optical fiber. Optical fibers can be classified with different standards: According to the fiber core doping or refractive index distribution, fibers are divided into step index fibers and graded index fibers; according to the polarization-maintaining ability to the transmitted light, fibers are divided into polarization-maintaining (PM) fibers and non-polarization-maintaining fiber; according to the presence or absence of laser-active dopants in the fiber core, fibers are divided into active fibers and passive fibers; according to the number of supported transmission modes, fibers are divided into single-mode fibers and multi-mode fibers [37].

Single-mode fibers, also known as fundamental or mono-mode fibers, are designed to

permit only one light mode to propagate. They are capable of wide bandwidths (e.g., $> 40$ GHz), low transmission loss, and are universally used in telecommunication networks over 1 km, typically at low-loss wavelength region ranging from 1260 nm to 1625 nm. Corning SMF-28 fibers are one of the most widely used single-mode fibers in the industry and telecommunication fields. They are compatible and fully compliant with recommendation standard ITU-T G.652.D. [38]. A SMF-28 fiber has a 8.2 µm-diameter fiber core and a 125 µm-diameter fiber cladding [39]. The fiber core is doped with 3.5 mol% $GeO_2$, while the fiber cladding is pure silica. Fig. 2.1(b) shows the schematic diagram of the cross section of a SMF-28 fiber (Corning, SMF-28 Ultra Optical Fiber, SMF-28). Large mode area (LMA)
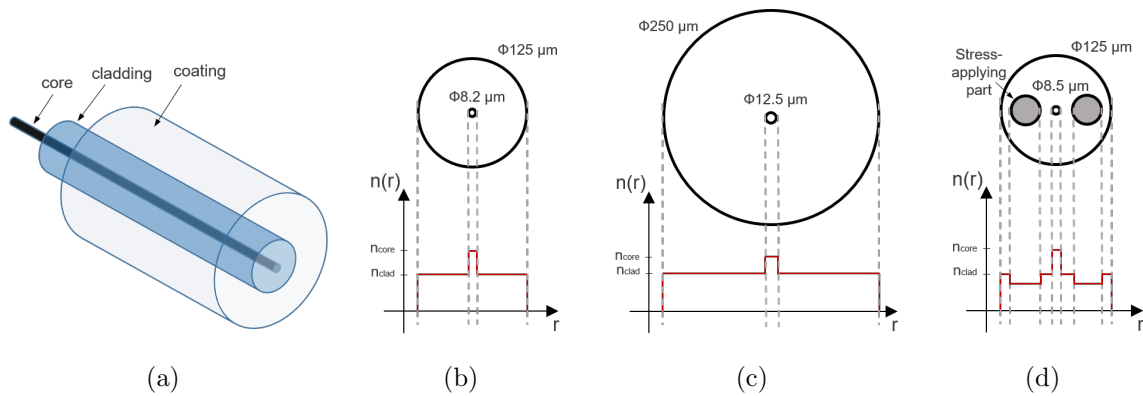


Figure 2.1: Schematic diagrams of (a) an optical fiber, the cross sections of (b) a SMF-28 fiber, (c) a LMA-250 fiber, (d) a PM-125 fiber.

fibers are a kind of single-mode fibers with a dopant concentration less than the standard telecom single-mode fiber (e.g., SMF-28 fiber), which can provide a larger effective mode area to lower the intensities at the same transmitted power and thus to reduce nonlinear effects. Active LMA fibers are used as gain media in fiber lasers and amplifiers. In addition to the active fibers, passive LMA fibers have been developed to enable mode-field-adapted transmission of the generated high-power wave. Fig. 2.1(c) shows the schematic diagram of the cross section of a passive LMA fiber (LIEKKI, Passive-12/250, LMA-250), whose core and cladding diameters are 12.5 µm and 250 µm, respectively.

PM fibers usually are also a kind of single-mode fibers. In many application fields, such as integrated-optic devices, optical fiber sensors based on interferometric techniques, and coherent optical communications, where there is a high requirement for fibers to transmit the complex amplitude (magnitude and phase) of a specific polarization (x or y direction), PM fibers are used. The circular cross sections of normal fibers are symmetric, while the cross sections of PM fibers are either elliptical or with stress-induced anisotropy of the refractive index. Fig. 2.1(d) shows the schematic diagram of the cross section of a Panda-Type PM fiber (Coherent, PM1550-XP: Panda-Type, PM-125), whose core and cladding

diameters are 8.5 µm and 125 µm, respectively. The structure eliminates the polarization degeneracy, thereby making the propagation constants of the linearly polarized waves on the two orthogonal axes different. The introduction of such phase mismatch finally reduces the coupling efficiency between the two orthogonal polarizations [40].

A step-index fiber can be regarded as a cylindrical dieletric waveguide specified by $n_{core}$ and $n_{clad}$. The refractive index difference between fiber core and cladding is slight, so the fractional refractive index change $\Delta$ is small:

$$\Delta \equiv \frac{n_{core}^2 - n_{clad}^2}{2n_{core}^2} \approx \frac{n_{core} - n_{clad}}{n_{core}} \ll 1, \tag{2.1}$$

which typically lies from 0.001 to 0.02 [40].

In guided ray theory, a ray incident from air into the fiber becomes a guided ray if the requirement of total internal reflection is met. By applying Snell's law at the air-core boundary, the acceptance angle of the fiber should be:

$$\theta_a \leq sin^{-1}\text{NA}, \tag{2.2}$$

where NA is the numerical aperture of the fiber, which is given by

$$\text{NA} = \sqrt{n_{core}^2 - n_{clad}^2} \approx n_{core}\sqrt{2\Delta}. \tag{2.3}$$

Here $n_{core} - n_{clad} \approx n_{core}\Delta$ and $n_{core} + n_{clad} \approx 2n_{core}$. In guided wave theory, an optical fiber is regarded as a cylindrical dielectric medium, so the electric and magnetic fields of supported guided waves (modes) can be obtained by using Maxwell's equations the boundary conditions imposed by the cylindrical dielectric core and cladding. In a cylindrical coordinate system, the Helmholtz equation is written as:

$$\frac{\partial^2 U}{\partial r^2} + \frac{1}{r}\frac{\partial U}{\partial r} + \frac{1}{r^2}\frac{\partial^2 U}{\partial \phi^2} + \frac{\partial^2 U}{\partial z^2} + n^2 k_o^2 U = 0, \tag{2.4}$$

where $U = U(r, \phi, z)$. The guided modes are waves traveling in the z direction with propagation constant $\beta$, so that the z dependence of $U$ is in the form of $e^{-j\beta z}$. They are periodic in the angle $\phi$ with period $2\pi$, so that they take the harmonic form $e^{-jl\phi}$, where $l$ is an integer ($l = 0, \pm 1, \pm 2,...$). Therefore, $U = U(r, \phi, z)$ can be written as $U(r, \phi, z) = u(r)e^{-jl\phi}e^{-j\beta z}$ and the radial profile $u(r)$ can be obtained from Eq. 2.4:

$$\frac{d^2 u}{dr^2} + \frac{1}{r}\frac{du}{dr} + \left(n^2(r)k_o^2 - \beta^2 - \frac{l^2}{r^2}\right)u = 0. \tag{2.5}$$

For simplification, two parameters $k_T$ and $\gamma$ are defined for core and cladding, respectively:

$$k_T^2 = n_{core}^2 k_o^2 - \beta^2, \tag{2.6}$$

$$\gamma^2 = \beta^2 - n_{clad}^2 k_o^2. \tag{2.7}$$

Here $k_T^2$ and $\gamma^2$ are both positive, and $k_T$ and $\gamma$ are both real. With this, Eq.2.5 can be separated into two Bessel differential equations for core and cladding:

$$\begin{aligned} \frac{d^2u}{dr^2} + \frac{1}{r}\frac{du}{dr} + \left(k_T^2 - \frac{l^2}{r^2}\right)u = 0, \quad r < a \quad \text{(core)} \\ \frac{d^2u}{dr^2} + \frac{1}{r}\frac{du}{dr} - \left(\gamma^2 + \frac{l^2}{r^2}\right)u = 0, \quad r > a \quad \text{(cladding)} \end{aligned} \tag{2.8}$$

The bounded solutions for the core are the Bessel functions of the first kind $J_l$ and for the cladding the modified Bessel functions of the second kind $K_l$:

$$u(r) \propto \begin{cases} J_l\left(k_T r\right), & r < a \quad \text{(core)} \\ K_l(\gamma r), & r > a \quad \text{(cladding)} \end{cases} \tag{2.9}$$

Fig. 2.2 shows two examples of the radial distribution $u(r)$ obtained from Eq. 2.9 for order $l = 0$ (left) and $l = 3$ (right), respectively. It can be seen that the parameters $k_T$
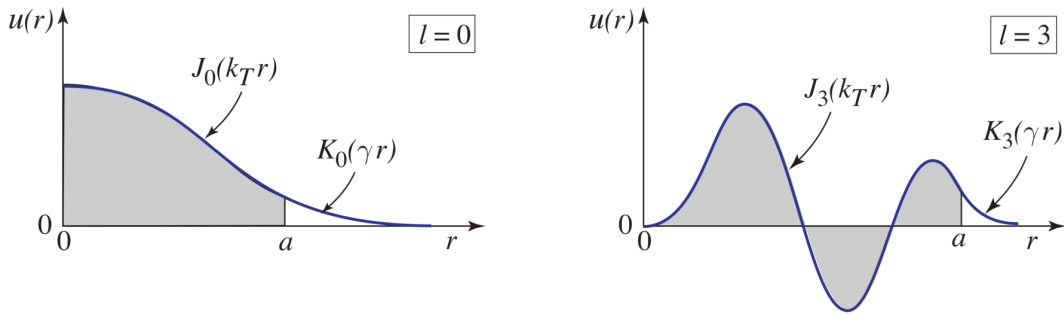


Figure 2.2: Examples of the radial distribution $u(r)$ for order $l = 0$ (left) and $l = 3$ (right) [40].

and $\gamma$ determine the change rate of $u(r)$ in the core and cladding. Larger $k_T$ corresponds to more oscillation of the radial distribution in the core, and larger values of $\gamma$ mean a more rapid decay in the cladding. Those two parameters can also be normalized based on Eqs. 2.6 and 2.7 by assuming $u = k_T a$ and $w = \gamma a$:

$$V = \sqrt{u^2 + w^2} = k_0 a \sqrt{n_{core}^2 - n_{clad}^2} = k_0 a \cdot \text{NA} = 2\pi \frac{a}{\lambda_o}\text{NA}. \tag{2.10}$$

Here, $V$ is called normalized frequency, which is an important parameter determining the number of guided modes and their propagation constants. When the cut-off condition $V < 2.405$ is met, only the fundamental $LP_{01}$ mode exists in the fiber, while other modes are all cut off. The fibers that met the cut-off condition are single-mode fibers. For a step-index multi-mode fiber with large $V$ parameter ($V \gg 1$), the number of supported guided modes $M$ can be estimated based on the normalized frequency $V$:

$$M = \frac{V^2}{2}. \tag{2.11}$$

**Silica fiber manufacturing**

Optical fiber manufacturing can be divided into two steps: Firstly, a preform is made by deposition methods. Secondly, the obtained preform is heated and stretched in a drawing tower to get final fibers [35].

A preform is a rod of glass, typically with a length of several meters long and a diameter of 10-50 mm. The refractive index profile has already been built into it. There are several alternative deposition methods to fabricate a preform, including outside vapor deposition, modified chemical vapor deposition, plasma chemical vapor deposition, vapor phase axial deposition, etc [41].
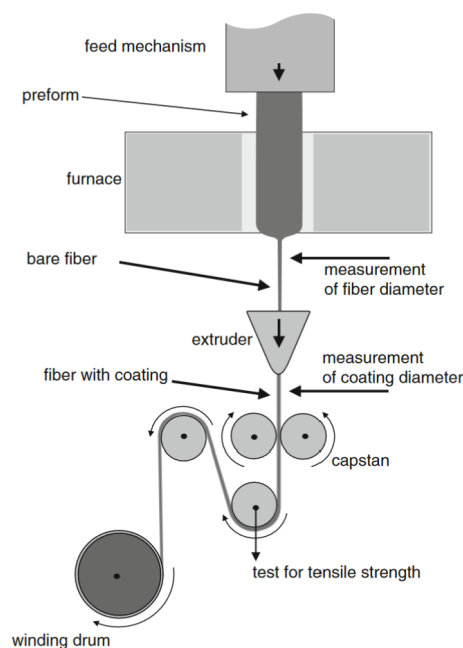


Figure 2.3: Schematic diagram of silica fiber fabrication process in a drawing tower [35].

A drawing tower is used to pull fibers from the obtained preform, as shown in Fig. 2.3. The preform is heated in the furnace to the temperature where the glass softens and begins to melt, i.e., 1950-2250 °C.

A thread of glass is caught and pulled into a fiber with a diameter of tens to hundreds of µm, most frequently 125 µm. For example, when the diameter is reduced to 200-fold, the length is increased to 40,000 times the original. The speed of advancing the preform into the heating zone is controlled to around hundreds of µm/s. After several hours, a preform of 1 m can be drawn into fibers of 40 km. During the whole drawing process, fiber diameter and other properties are monitored in real time for elaborate closed-loop control parameters so that the deviation of the fiber diameter can be maintained to within 0.1 µm. Then the bare fiber is cooled down, and a plastic coating is applied by an extruder. This process is also essential because the coating protects the bare fiber from physical extrusion and chemical corrosion and contributes to minimizing micro-bending loss. Acrylates and polyimides are used as the coating materials, also epoxides and silicones. After that, a test for tensile strength is carried out, and finally, the fiber is coiled on a spool using a winding drum [35].

## 2.1.2   Mechanical properties of fiber

### Residual stresses inside fiber

The intrinsic residual stresses inside the fibers mainly consist of two parts: mechanical stress and thermal stress [42–44]. Mechanical stress, also called draw-induced stress, results from the drawing tension applied to the fiber during the fiber drawing. In a conventional fiber with a pure-silica cladding and a germanium-doped core, the cladding has a higher viscosity and solidifies first during the drawing process. When the fiber cools down, the tension is concentrated in the high viscous cladding, while the low viscous core receives relatively smaller draw tension because it solidifies at lower temperatures. Mechanical equilibrium is established when the drawing process is finished, and the draw tension is removed: the mechanical stress in the cladding is partly relaxed but still tensile, while that in the core becomes compressive. On the other hand, the thermal stress comes from the fact that the core has a higher coefficient of thermal expansion (CTE) than the cladding due to the addition of dopants. Thus, during the drawing and cooling of the fiber, opposite to the mechanical stress, the thermal stress in the fiber core is tensile, while in the cladding, it is compressive [42, 43]. Those two different kinds of residual stresses act oppositely and can be used to compensate for each other to obtain high-quality fibers with very low total residual stresses [42].

For a conventional fiber with pure-silica cladding and germanium-doped core, the axial mechanical stress in the core $\sigma^m_{z,core}$ and the cladding $\sigma^m_{z,clad}$ can be expressed as [45]:

$$\sigma^m_{z,core} = -F(\frac{E_{core}}{A_{core}E_{core} + A_{clad}E_{clad}}), \qquad (2.12)$$

$$\sigma^m_{z,clad} = \frac{F}{A_{clad}}(\frac{A_{core}E_{core}}{A_{core}E_{core} + A_{clad}E_{clad}}), \qquad (2.13)$$

where $F$ is the draw tension, $A_{core}$ and $E_{core}$, $A_{clad}$ and $E_{clad}$, are the cross-sectional areas and Young's moduli for core and cladding, respectively.

The axial thermal stress in the core $\sigma^t_{z,core}$ and the cladding $\sigma^t_{z,clad}$ of the step-index optical fiber can be expressed as follows [46, 47]:

$$\sigma^t_{z,core} = -\frac{(\alpha_{core} - \alpha_{clad})\Delta T E}{1 - \nu}(1 - \frac{a^2}{b^2}), \qquad (2.14)$$

$$\sigma^t_{z,clad} = \frac{(\alpha_{core} - \alpha_{clad})\Delta T E}{1 - \nu}(\frac{a^2}{b^2}), \qquad (2.15)$$

where $\alpha_{core}$ and $\alpha_{clad}$ are the CTEs of fiber core and cladding, $E$ is Young's modulus, $\nu$ is Poisson's ratio, $a$ and $b$ are the diameters of fiber core and cladding, $\Delta T$ is the temperature difference between the ambient temperature $T_{ambient}$ and the glass transition temperature $T_g$ of the fiber core: $\Delta T = T_{ambient} - T_g$. It is reported that the CTE of glass, $\alpha$, is highly related to the dopant type and concentration. The relationship between CTE and dopant concentration can be expressed as follows [48]:

$$\alpha = \sum_i \frac{\alpha_i \rho_i x_i}{\rho}, \qquad (2.16)$$

where $\rho$ is the aggregate density in the silicate glass, $\alpha_i$, $\rho_i$, and $x_i$ are the CTE, the density, and the volume fraction of each constituent of the glass. Therefore, it can be expected that the dopant concentration influences the axial thermal stress.

The total residual stress in the fiber depends on the net effect of thermal stress and mechanical stress. Fig. 2.4 shows a typical cross-sectional residual stress profile measured by the Brace-Köhler compensator technique [43]. It can be seen that there are peaks at the core-cladding boundary, which are due to the OH impurities in this region. Those impurities lower the viscosity of the molten silica glass, so the core-cladding boundary region sustains a relatively small amount of the draw tension, similar to the core, and compressive stresses are formed in the boundary region after drawing.
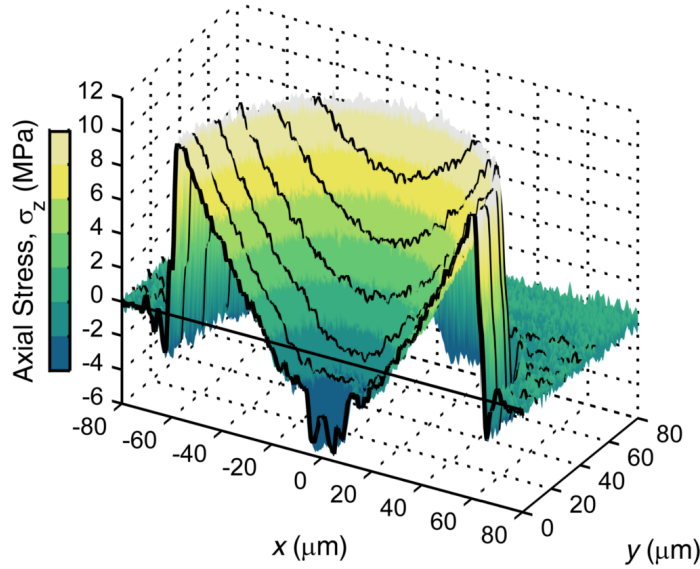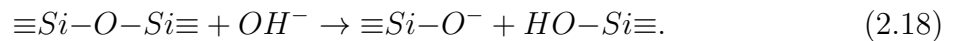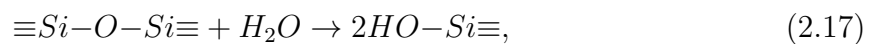
Figure 2.4: Typical cross-sectional axial stress profile in an unperturbed SMF-28 fiber measured by the Brace-Köhler compensator technique [43].

**Glass breakage and hot corrosion**

Cracks can occur in glass, which might precipitously cause glass fibers to break. For some kinds of cracks, fractures propagate across the glass with a speed of hundreds of m/s. For other tiny cracks, however, they may advance only at an imperceptible slow speed. It has been verified that its growth rate is only $10^{-14}$ m/s, corresponding to one snapping atomic bond per hour, or three years needed for 1 meter [35]. That means obvious damage is only visible after years, which gives people a false sense of safety before that. Actually, under high vacuum, tests show that pristine glass pieces can withstand tensions of more than 10 GPa, much larger than a lot of metal alloys. In the real environment, however, tensile strength degrades because of surface defects to 3-8 GPa [49]. Surface defects or contact with abrasives produce microscopic cracks in glass fibers, which are the breakthrough points for chemicals, especially for water. Water can exist in those cracks as both molecular water and hydroxyl. Even though silica is well known for its inertness at low temperatures, it undergoes the following reactions, resulting in a formation of immobile hydroxyl [50, 51]:

$$\equiv Si-O-Si\equiv \; + \; H_2O \rightarrow 2HO-Si\equiv, \tag{2.17}$$

$$\equiv Si-O-Si\equiv \; + \; OH^- \rightarrow \; \equiv Si-O^- + HO-Si\equiv. \tag{2.18}$$

These reactions break the bridging oxygen in the silica structures, which lets the cracks

grow gradually and finally compromise the mechanical integrity of the glass fiber. It has been reported that high humidity in the environment has a strong negative impact on silica fiber bending strength: a measurable decrease of a $\sim$2 GPa in the longitudinal modulus of silica glass was observed when the OH content increases from 200 ppm to 3000 ppm [52]. As for aging and fatigue, it has also been proved that temperature increase at a relatively constant humidity leads to the deterioration of mechanical properties of glass fiber, which is due to the higher reaction rate and the higher water diffusion rate.
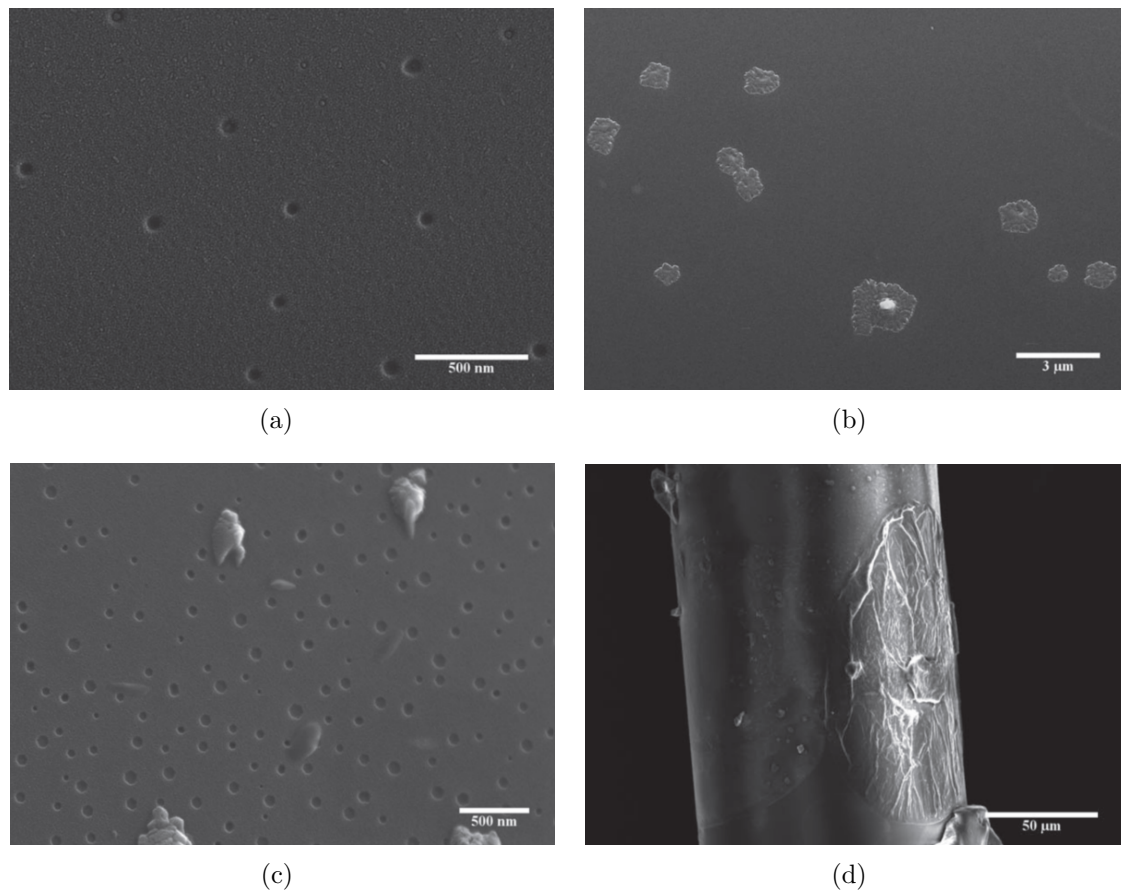


Figure 2.5: SEM images of the crystal distributions/crystalline regions of (a) a Furukawa silica glass fiber after a 144 h heat-treatment at 700 ℃ with 80 000×, (b) T-08 silica glass fiber after a 24 h heat-treatment at 700 ℃ with 10 000×, (c) a Suprasil 2 silica glass fiber after a 22 h heat-treatment at 600 ℃ with 50 000×, (d) a Suprasil 2 silica glass fiber after an extended 2200 h heat-treatment at 200 ℃ with 800× [51].

However, for fibers treated at high temperatures, immobile hydroxyl reactions/water diffusion is not the only cause of fiber strength degradation: surface crystallization plays an important role as well. When the temperatures are above 250 ℃, the devitrification of silica glass occurs, and the resulting crystal is cubic $\beta$-cristobalite, which transforms to the tetragonal $\alpha$-cristobalite when the silica glass is later cooled down to room temperature

[53]. Due to the volume mismatch/CTE difference between the crystal grain and glass matrix while cooling from the high crystal growth temperatures to room temperature, interfacial stresses occur, leading to the strength degradation of silica fiber [51].

Figs. 2.5(a) to 2.5(d) show the scanning electron microscope (SEM) images of the crystal distributions of different kinds of silica fiber after heat treatment at high temperatures. The growth rate of the crystalline layer was proved to be strongly dependent on several factors, such as temperature [54], impurity content of the glass [51, 55], stoichiometry of the silica [56], and water vapor pressure of the atmosphere [57].

It has been concluded that, generally, surface crystallization may be mainly responsible for fiber strength degradation at temperatures in excess of $\sim$800 °C, while immobile hydroxyl reactions/water diffusion into the glass surface may be primarily responsible for the mechanical weakening at lower temperatures [51].

The strength degradation of silica glass fiber due to heat treatment at high temperatures is also known as hot corrosion. It makes silica fibers fragile and brittle, which is one of the most challenging issues in using silica fibers in high-temperature environments. The basic fracture mechanics analysis shows that the product of the mechanical strength $\sigma$ and the square root of the flaw size $\sqrt{c}$ is a constant: $\sigma\sqrt{c} = k$ [51]. Considering the fact that the size of a flaw, which could also be regarded as crack depth [58] or crystalline region [51], is time-dependent, it is easy to conclude that the mechanical strength degradation of silica fiber is related to the temperature treatment time: the longer the time at high temperatures, the weaker the mechanical strength.

## Properties at high temperatures

Given the increasing demand for using all-optical fiber sensors in high-temperature environments, some basic mechanical properties of silica fiber need to be studied. The volume of fused silica increases with temperature, while its CTE is only $5.5 \times 10^{-7}$/°C, much smaller than the CTEs of other materials like copper and aluminum. This anomalous behavior can be explained by the existence of "two or more distinctly different atomic arrangements coexisting in a homogeneous equilibrium in ratios that vary with temperature and pressure" [59]. The atomic arrangements characteristics of fused silica at low temperatures (structure-I) have a larger volume and weaker cohesive forces than those associated with higher temperatures (structure-II). When the temperature increase, the amount of structure-II increases, the smaller volume of which counteracts but does not totally overcome the normal expansion caused by temperature increase. It has been reported that from room temperature to 900 °C, mechanical properties of fused glass, like elastic moduli and Poisson's ratio, increase almost linearly with temperature [60], which can also be explained by the above theory: it is more difficult to stretch the material when

stronger cohesive forces and a more compact structure exist. However, for glasses doped with other materials, the properties of these composite systems are more complicated, and strong nonlinear behaviors have been observed [60]. Considering the fact that the core of silica fiber is doped with germanium, it is expected that the mechanical properties of silica fiber also show unique changes as temperature increases.

The silica optical fiber behaves in a fully elastic behavior at lower temperatures in a fully viscous manner at higher temperatures, while viscoelastic behavior at intermediate temperatures [61]. The best description of the viscosity of optical fiber is given by the two-exponential equation [49, 62]:

$$\eta = ATe^{(\frac{E_{a1}}{RT})}[1 + Be^{(\frac{E_{a2}}{RT})}], \qquad (2.19)$$

where $T$ is temperature in K, $R$ is the molar gas constant, A and B are fitted pre-exponential scaling factors based on Arrhenius fit. $E_{a1}$, and $E_{a2}$ are constants. This equation can be used in a wide temperature range, as it involves a temperature-dependent pre-exponential term. Actually, at high temperatures, the activation energy $E_a$ meets $E_a = E_{a1} + E_{a2}$, while $E_a = E_{a1}$ at low temperatures [62]. This equation has been found as a direct consequence of the defect model of viscous flow [74]: The defects involved in flow are SiO molecules resulting from broken silicon-oxygen bonds, so the SiO molecules and five-coordinated silicon atoms involved in viscous flow derive from broken bonds [63]. The higher the concentration of broken bonds is, the lower the viscosity is expected [62].

Shao et al. [49] studied the viscosity of silica fibers over 1000-1150 °C. The viscosity follows the Arrhenius expression well, with derived activation energy for the viscous flow of $E_a = 450$ KJ $\cdot$ mol$^{-1}$. However, the viscosity was slightly lower than those obtained for bulk fused quartz. The annealing and strain temperatures for an optical fiber were derived as 1114 °C and 1010 °C, both lower than those of fused quartz/silica, respectively. Lindner et al. [61] studied the temperature periods where the transition from purely elastic to viscoelastic behavior happens. It was found that the fiber showed an elastic behavior at and below ∼600 °C, and a viscoelastic behavior started at ∼700 °C and above.

**Glass transition**

Silicate glasses are one of the most commonly used oxide amorphous materials, which are usually produced by rapid cooling and the elementary particles inside are in a disordered pattern [62]. When the temperature increase, the amorphous-state features change gradually like liquid.

To distinguish the glass-liquid change phenomena, the term "glass transition" has been frequently used. Not like viscosity, which is a continuous function of temperature, the glass

transition, however, is accompanied by explicit discontinuities in the derivative parameters like the specific heat or CTE. The glass transition is the gradual and reversible transition in amorphous material (e.g., fused quartz) from a hard state into a viscous state when the temperature is heated up. The glass transition temperature $T_g$ characterizes the temperature ranges over which the glass transition happens, which is always lower than the melting temperature $T_m$. The CTE, heat capacity, shear modulus, viscosity, and many other properties of material differ substantially below and above $T_g$. For fused silica, its $T_g$ is around 1200 °C [64], while the $T_g$ of glass fiber is regarded at the same level [49], even though theoretically it should be slightly lower because of doping in the fiber core. It is noticeable that the glass viscous flow of silica fibers can occur under load at temperature regimes close to or over glass transition temperature, leading to a drastic change in sensing performance.

### 2.1.3   Sapphire fiber

Sapphire is a kind of mineral corundum, consisting of aluminum oxide in the form of $\alpha$-$Al_2O_3$ and trace amounts of iron, titanium, chromium, etc. In its corundum structure, the oxygen positions approximate to hexagonal close packing, with trivalent aluminum cations occupying two-thirds of the octahedral sites [65]. Generally, single crystal fiber based on $\alpha$-$Al_2O_3$ is called single crystal sapphire fiber, or sapphire fiber, directly.
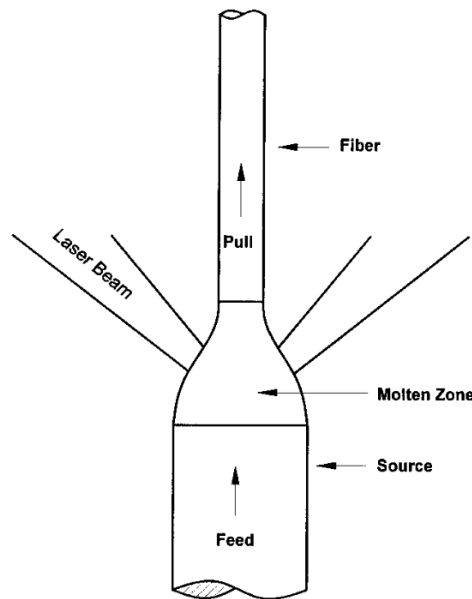


Figure 2.6: Schematic diagram of laser-heated pedestal-growth (LHPG) method [67].

For the growth of sapphire fibers, there are mainly two methods used. One is called the edge-defined film-fed growth (EFG) method [66]. Another one is called the laser-heated pedestal-growth (LHPG) method [67], the schematic diagram of which is shown in Fig. 2.6.

Typically, a $CO_2$ laser beam is focused onto the tip of a source rod to provide a uniform and ultra-clean heat region. The head of the source rod is molten, and a seed fiber is dipped into the molten zone and slowly pulled upward to grow single-crystal sapphire fiber along it. The LHPG method is the most promising way available to obtain high-optical-quality sapphire fibers, and it is now widely used in the fabrication of commercial sapphire fibers.

The refractive index of sapphire fiber as a function of wavelength for an ordinary ray follows a Sellmeier equation [68, 69]:

$$n^2 - 1 = \frac{1.4313493\lambda^2}{\lambda^2 - 0.0726631^2} + \frac{0.65054713\lambda^2}{\lambda^2 - 0.1193242^2} + \frac{5.3414021\lambda^2}{\lambda^2 - 18.028251^2}. \tag{2.20}$$

Fig. 2.7 shows the calculated refractive index of sapphire as a function of transmission light wavelength according to Eq. 2.20, and Table 2.1 shows the parameters of a single crystal sapphire. Sapphire fiber shows some superior properties, such as high melting point, high hardness, resistance to chemical corrosion, and a wide spectral range of light transmittance, which makes it a good alternative for sensors in various harsh environments, including ultra-high temperatures.
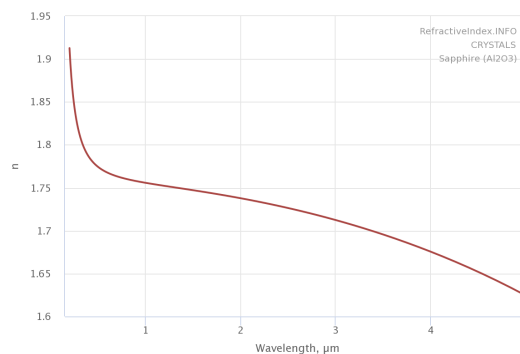


Figure 2.7: Refractive index of sapphire as a function of transmission light wavelength [68, 69].

Table 2.1: Parameters of a single crystal sapphire [70].

| Parameter | Value |
|---|---|
| Melting point | 2040 °C |
| Coefficient of thermal expansion | $7.7 \times 10^{-6}$ /° C (20-500 °C) |
| Thermal coefficient of refractive index | $13 \times 10^{-6}$ /° C |
| Hardness | 525 Knoop, Mohs 9 |
| Tensile strength | 275 to 400 MPa (40–58 kpsi) |
| Compressive strength | 2.0 GPa (300 kpsi) |
| Young's modulus | 345 GPa ($50 \times 10^6$ psi) |
| Effective NA | 0.12 |

## 2.2   Fiber Bragg grating (FBG)

FBG is a kind of wavelength-specific reflector inside an optical fiber created by a periodic refractive index modulation in the optical fiber's core along the z-axis over the length $L$. Fig. 2.8 shows the schematic structure of a FBG. A broad spectrum light is injected into fiber, and only those wavelengths close to the Bragg wavelength $\lambda_B$ can be reflected, while others will be transmitted.
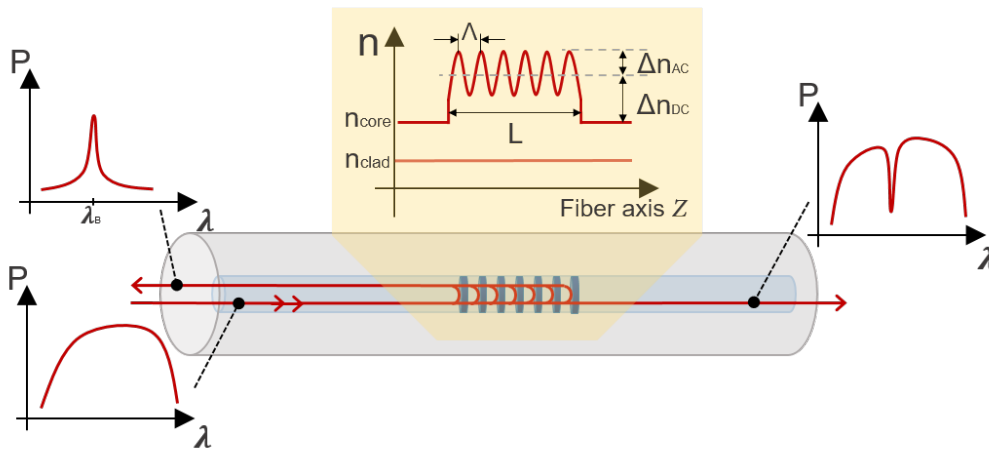


Figure 2.8: Schematic structure of a FBG.

The periodic refractive index modulation of FBG can be expressed as follows:

$$n(z) = n_{eff} + \Delta n_{eff}(z) = n_{eff} + \Delta n_{DC} + \Delta n_{AC} \cdot sin(\frac{2\pi z}{\Lambda}), \qquad (2.21)$$

where $n_{eff}$ is the effective refractive index of the fiber, $\Delta n_{eff}(z)$ is the effective refractive index change along the z-axis, $\Lambda$ is the grating period, $\Delta n_{AC}$ is the strength of the refractive index modulation along the z-axis (AC component), and $\Delta n_{DC}$ is the mean value of the refractive index change over $L$ due to the grating inscription (DC component). In fact, there are many types of $\Delta n_{eff}(z)$ to fabricate FBGs with different functions, as shown in Fig. 2.9.

The reflected wavelength ($\lambda_B$), called the Bragg wavelength, is defined by the relationship,

$$\lambda_B = 2\bar{n}\Lambda = 2(n_{eff} + \Delta n_{DC})\Lambda \approx 2n_{eff}\Lambda, \tag{2.22}$$

where $\bar{n}$ is the averaged refractive index over the whole grating period and can be approximated as $n_{eff}$.
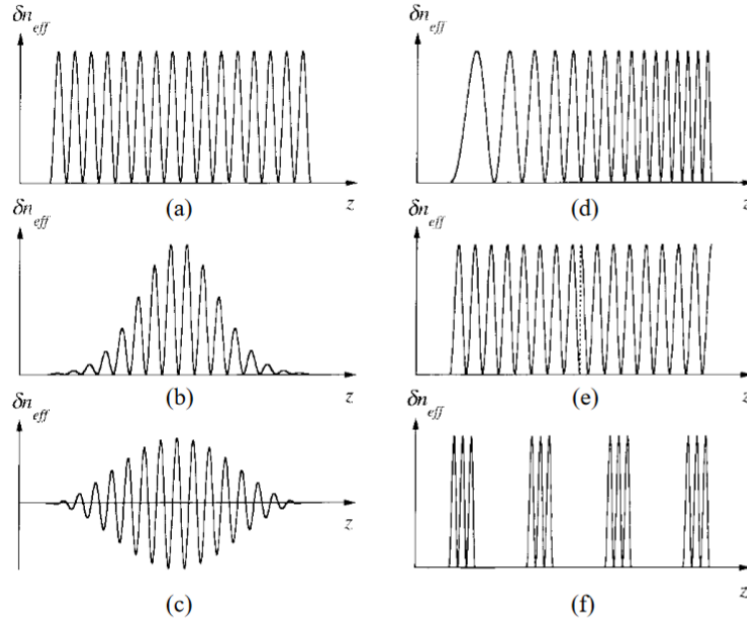


Figure 2.9: Common types of $\Delta n_{eff}(z)$ for FBGs: (a) uniform with positive-only index change, (b) Gaussian-apodized, (c) raised-cosine-apodized with zero-dc index change, (d) chirped, (e) discrete phase shift ($\pi$), and (f) superstructure [71].

## 2.2.1 Principle of FBG

**Coupled-mode theory**

Coupled-mode theory (CMT) has been applied extensively in guided-wave optics as a mathematical tool for the analysis of electromagnetic wave propagation [72], and it can also be applied to analyze the refraction spectrum of FBG [71]. In an ideal waveguide

with no grating perturbation, the transverse component of the electric field can be written as a superposition of j-th modes together:

$$\vec{E_t}(x,y,z,t) = \sum_j [A_j(z)e^{i\beta_j z} + B_j(z)e^{-i\beta_j z}] \times \vec{e_{jt}}(x,y)e^{-i\omega t}, \tag{2.23}$$

where $A_j(z)$ and $B_j(z)$ are the amplitudes of the j-th mode transmitting along the forward (+z) and backward (-z) directions, $\vec{e_{jt}}(x,y)$ represents the transverse mode field. For a Bragg grating in a single-mode fiber, the dominant interaction is the reflection of the fundamental froward mode into the fundamental counter-propagating mode near the Bragg wavelength. "Synchronous approximation" [73] can be made by neglecting other trivial coupling, and the following equations can be obtained:

$$\frac{dA(z)}{dz} = -i\hat{\sigma}A(z) - i\kappa B(z), \tag{2.24}$$

$$\frac{dB(z)}{dz} = i\hat{\sigma}B(z) + i\kappa A(z), \tag{2.25}$$

where $\hat{\sigma}$ is the "DC" self-coupling coefficient, $\kappa$ is the "AC" coupling coefficient, which can be expressed as follows when the grating is uniform [71]:

$$\hat{\sigma} = \beta - \frac{\pi}{\Lambda} + \sigma = 2\pi n_{eff}(\frac{1}{\lambda} - \frac{1}{\lambda_B}) + \frac{2\pi}{\lambda}\Delta n_{DC}, \tag{2.26}$$

$$\kappa = \frac{\pi}{\lambda}\Delta n_{AC}. \tag{2.27}$$

Closed-form solutions can be found for Eqs. 2.24 and 2.25 when appropriate boundary conditions are met. The reflectivity of the uniform fiber grating with a length of $L$ can be obtained, by assuming the forward (+z) wave incident from $z = -\infty$ ($A(-L/2) = 1$) and no backward (-z) wave when $z \geq L/2$ ($B(L/2) = 0$). The amplitude reflection coefficient $\rho$ and $R$ the reflectivity can be shown as follows [71, 74]:

$$\rho = \frac{-\kappa \sinh(\sqrt{\kappa^2 - \hat{\sigma}^2}L)}{\hat{\sigma}\sinh(\sqrt{\kappa^2 - \hat{\sigma}^2}L) + i\sqrt{\kappa^2 - \hat{\sigma}^2}\cosh(\sqrt{\kappa^2 - \hat{\sigma}^2}L)}, \tag{2.28}$$

$$R = \frac{\sinh^2(\sqrt{\kappa^2 - \hat{\sigma}^2}L)}{\cosh^2(\sqrt{\kappa^2 - \hat{\sigma}^2}L) - \frac{\hat{\sigma}^2}{\kappa^2}}. \tag{2.29}$$

According to Eqs. 2.26 and 2.27, both $\hat{\sigma}$ and $\kappa$ are wavelength-dependent, $\rho$ and $R$ are wavelength-dependent as well. Fig. 2.10 shows the theoretical spectra according to the coupled-mode theory and equations above under different $\Delta n_{AC}$ with $L = 3$ mm, $n_{eff} = 1.45$ and $\Delta n_{DC} = 0.01$. For Eq. 2.29, the maximum reflectivity $R_{max}$ is [71, 75]:
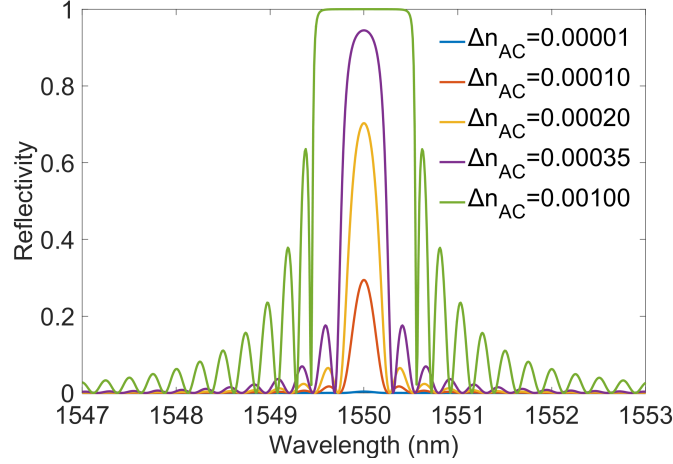
Figure 2.10: Theoretical spectra according to the coupled-mode theory about under different $\Delta n_{AC}$ with $L = 3$ mm, $n_{eff} = 1.45$ and $\Delta n_{DC} = 0.01$.

$$R_{max} = \tanh^2(\kappa L), \tag{2.30}$$

and it can be achieved when $\hat{\sigma} = 0$, which corresponds to the wavelength value:

$$\lambda_{max} = (1 + \frac{\Delta n_{DC}}{n_{eff}})\lambda_B, \tag{2.31}$$

For the bandwidth of a uniform FBG, one method is to measure the wavelength range between the first zeros on either side of the maximum reflectivity. According to Eq. 2.29, the first zeros bandwidth $\Delta\lambda_0$ can be obtained [71]:

$$\frac{\Delta\lambda_0}{\lambda} = \frac{\Delta n_{AC}}{n_{eff}}\sqrt{1 + (\frac{\lambda_B}{\Delta n_{AC}L})^2}, \tag{2.32}$$

In the "weak-grating limit", where $\Delta n_{AC}$ is very small ($\Delta n_{AC} \ll \frac{\lambda_B}{L}$), we could find [71]:

$$\frac{\Delta\lambda_0}{\lambda} \approx \frac{\lambda_B}{n_{eff}L} = \frac{2\Lambda}{L} = \frac{2}{N}, \tag{2.33}$$

where $N$ is the number of the grating planes. Here, the bandwidth of a weak FBG is "length-limited". The longer the length $L$ is, the narrower the bandwidth will be.

While, in the "strong-grating limit", when $\Delta n_{AC}$ is very large ($\Delta n_{AC} \gg \frac{\lambda_B}{L}$), we could find [71]:

$$\frac{\Delta\lambda_0}{\lambda} \approx \frac{\Delta n_{AC}}{n_{eff}}. \tag{2.34}$$

In this case, the light will not transmit through the entire length of the FBG, and thus

the bandwidth can be regarded to be independent of length and directly proportional to the refractive index modulation.

Another method to define the bandwidth of a FBG is to measure the full width at half-maximum (FWHM) $\Delta\lambda_{FWHM}$. Actually, for strong gratings, the bandwidth is similar whether to measure the wavelength range, at the first zeros, or at the FWHM. As shown as the green line ($\Delta n_{AC}$=0.001) in Fig. 2.10, in this case, it can be regarded that $\Delta\lambda_{FWHM} \approx \Delta\lambda_0$.

**Strain and temperature sensitivities of FBG**

FBGs are inherently sensitive to temperature and strain because both $n_{eff}$ and $\Lambda$ vary as temperature and strain alter, as shown as follows [76]:

$$
\begin{aligned}
\Delta\lambda_B(T,\varepsilon) &= 2\left(\Lambda\frac{\partial n_{eff}}{\partial T} + n_{eff}\frac{\partial \Lambda}{\partial T}\right)\Delta T + 2\left(\Lambda\frac{\partial n_{eff}}{\partial \varepsilon} + n_{eff}\frac{\partial \Lambda}{\partial \varepsilon}\right)\varepsilon \\
&= \Delta\lambda_B(T) + \Delta\lambda_B(\varepsilon),
\end{aligned}
\tag{2.35}
$$

where $\Delta T$ is the temperature change, $\varepsilon$ is the applied strain, $\Delta\lambda_B(T)$ represents the temperature-induced Bragg wavelength change, and $\Delta\lambda_B(\varepsilon)$ represents the wavelength change caused by strain.

For the temperature-induced Bragg wavelength change, when ignoring the negligible waveguide effect, we could obtain:

$$
\begin{aligned}
\Delta\lambda_B(T) &= 2\left(\Lambda\frac{\partial n_{eff}}{\partial T} + n_{eff}\frac{\partial \Lambda}{\partial T}\right)\Delta T = \lambda_B\left(\frac{1}{n_{eff}}\frac{\partial n_{eff}}{\partial T} + \frac{1}{\Lambda}\frac{\partial \Lambda}{\partial T}\right)\Delta T \\
&\approx \lambda_B(\zeta + \alpha)\Delta T,
\end{aligned}
\tag{2.36}
$$

where $\zeta$ is the thermo-optic coefficient and $\alpha$ is the CTE.

However, it has been found that there is a nonlinear relationship between $\Delta\lambda_B(T)$ and temperature in a wide temperature range [8]. The wider the temperature range is, the more obvious the nonlinearity appears. A polynomial function of temperature $T$ can also be used to represent $\Delta\lambda_B(T)$:

$$
\Delta\lambda_B(T) = \sum_{i=0}^{n} a_i T^i,
\tag{2.37}
$$

where $a_i$ are polynomial coefficients.

For the strain-induced Bragg wavelength change $\Delta\lambda_B(\varepsilon)$, it can be transformed into the

following equation when the waveguide effect is ignored:

$$\Delta\lambda_B(\varepsilon) = 2\left(\Lambda\frac{\partial n_{eff}}{\partial\varepsilon} + n_{eff}\frac{\partial\Lambda}{\partial\varepsilon}\right)\varepsilon \approx 2\Lambda\left[-\frac{n_{eff}^3}{2}\Delta\left(\frac{1}{n_{eff}^2}\right)\right] + 2n_{eff}\varepsilon_{zz}L\frac{\partial\Lambda}{\partial L}. \quad (2.38)$$

If the elastic-optical coefficients of the material $p_{ij}$ are introduced, we can obtain the following equation:

$$\Delta\left(\frac{1}{n_{eff}^2}\right) = (p_{11} + p_{12})\,\varepsilon_{rr} + p_{12}\varepsilon_{zz}. \quad (2.39)$$

The fiber is axisymmetric and $\frac{\partial\Lambda}{\Lambda}\frac{L}{\partial L} = 1$, so by combining the Eqs. 2.22, 2.38, and 2.39, we can obtain:

$$\Delta\lambda_B(\varepsilon) = \lambda_B\left\{-\frac{n_{eff}^2}{2}\left[(p_{11} + p_{12})\,\varepsilon_{rr} + p_{12}\varepsilon_{zz}\right] + \varepsilon_{zz}\right\}. \quad (2.40)$$

Considering the fact that $\left|\frac{\varepsilon_{rr}}{\varepsilon_{zz}}\right| = v$ for a free fiber, this equation can be finally transferred as follows:

$$\Delta\lambda_B(\varepsilon) = \lambda_B\left\{-\frac{n_{eff}^2}{2}\left[-(p_{11} + p_{12})\,v_{fiber} + p_{12}\right] + 1\right\}\varepsilon_{zz} = \lambda_B k_\varepsilon\varepsilon_{zz}, \quad (2.41)$$

where $k_\varepsilon$ is the relative strain sensitivity, also called k-factor. In most common cases, we get $p_{11} = 0.116$, $p_{12} = 0.255$, $v_{fiber} = 0.16$, and $n_{eff} = 1.4473$, so $k_\varepsilon$ is calculated to be 0.795, which has also been verified experimentally [77]. For Bragg wavelength at 1550 nm, the strain sensitivity is 1.23 pm/$\mu\varepsilon$. It should be noticed that, in general, $k_\varepsilon$ is regarded as a constant for strain sensing. However, in a wide temperature range over several hundred degrees, it has been found that $k_\varepsilon$ is temperature-dependent [78]. According to [60], Poisson's ratio $\nu_{fiber}$ increases with temperature, and the temperature dependence can be approximately expressed with a linear function:

$$\nu(T) = \nu_{0,fiber} + \frac{d\nu_{fiber}}{dT}\Delta T, \quad (2.42)$$

where $\nu_{0,fiber}$ is the Poisson's ratio at 0 °C and $\frac{d\nu_{fiber}}{dT}$ is the temperature sensitivity of Poisson's ratio. Therefore, the relative strain sensitivity $k_\varepsilon$ can be written as [78]:
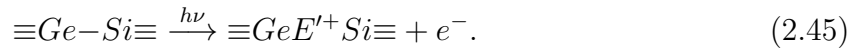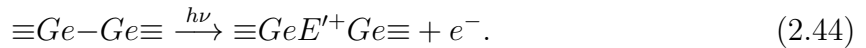
$$k_\varepsilon(T) = \{1 - \frac{n_{eff}^2}{2}[p_{12} - (\nu_{0,fiber} + \frac{d\nu_{fiber}}{dT}\Delta T)(p_{12} + p_{11})]\}. \quad (2.43)$$

## 2.2.2   Type-I FBG

**Refractive index modulation mechanism**

Type-I FBGs are the most widely used FBGs, whose refractive index modulation is typically introduced using UV light. Interference patterns are created by optical setups and UV lasers, which provide the necessary periodicity (usually in the form of a sinusoid) on the nanometer scale for FBGs. The fiber is placed in the interference pattern region, and the refractive index of fiber in this region is modulated due to the photo-chemical process [79].

For germanium-doped silica fibers, "wrong bonds" like Ge-Ge defect and Ge-Si defect are formed during the fiber drawing process or ionizing radiation. These defects are called germanium oxygen deficient centers (GODCs) and are believed to be responsible for the photosensitivity of germanium-doped silica fibers. When a UV light at around 245 nm irradiates a GODC, a single photo ionizes the wrong band to form a GeE' center [76]. It promotes an electron into the conduction band, as expressed in the equations below:

$$\equiv Ge-Ge\equiv \xrightarrow{h\nu} \equiv GeE'^{+}Ge\equiv + e^{-}. \tag{2.44}$$

$$\equiv Ge-Si\equiv \xrightarrow{h\nu} \equiv GeE'^{+}Si\equiv + e^{-}. \tag{2.45}$$

The promoted electron in the conduction band will either recombine with the GeE' center immediately to produce luminescence, or diffuse through the matrix until it is trapped by a $Ge(1)$ or $Ge(2)$ center to form $Ge(1)^{-}$ or $Ge(2)^{-}$ center, respectively. The $Ge(1)^{-}$ and $Ge(2)^{-}$ centers, also called "electron traps", are composed of an electron trapped at a four coordinated Ge substitutional for Si in the SiO2 tetrahedral network, with the $Ge(1)^{-}$ center being coordinated to four O–Si bonds, and the $Ge(2)^{-}$ center to one O–Ge and three O–Si bonds. Fig. 2.11 shows those common defects in germanium-doped silica fibers and the defects caused by UV irradiation.

Several models have been proposed to further explain the final refractive index changes after the formation of GeE'. The "color center" model, which believes that refractive index modulation is due to the increased polarizability from the GeE' defect, is one of the most popular ones. It is first noticed and further supported by the evidence that a strong absorption occurs for those fibers at a wavelength range of 240-250 nm (around 5 eV), which is exactly the absorption wavelength of Ge-Ge and Ge-Si defects. As a comparison, the absorption wavelength for pure silica is much more challenging, at around 138 nm (around 9 eV) [76] [83].

In addition to the color center model, other hypotheses based on the formation of built-in periodic space-charge electric fields by the photoexcitation of defects (dipole model), laser
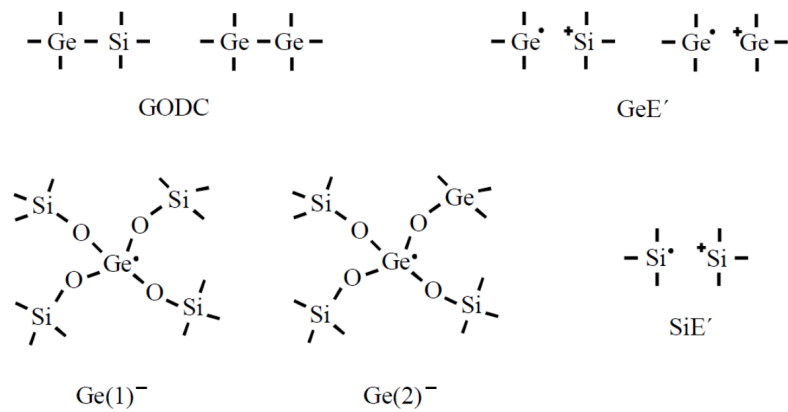
Figure 2.11: Common defects in germanium-doped silica fibers and the defects caused by UV irradiation [80–83].

irradiation-induced density changes (compaction model), and the alleviation of built-in thermoelastic stresses in the fiber core (stress-relief model), have also been proposed [76].

**Hydrogen loading**

Considering that the germanium dopant concentration (typically 3.5 mol% for SMF-28 fibers) and the corresponding number of GODC is limited, it would be advantageous if the photosensitivity of fiber could be further improved. Hydrogen loading is the most widely used method for photosensitivity enhancement. Hydrogen molecules will diffuse into glass fibers by putting fibers in a hydrogen atmosphere under high pressure. High temperature also helps the hydrogen diffusion, but it also reduces the solubility [84]. Those hydrogen molecules react in the glass at normal Si-O-Ge sites, producing hydroxyl (OH groups) [85], and these reactions can be driven either thermally or photolytically.

The inscription of FBGs in hydrogen-loaded fibers undoubtedly involves both thermal and photolytic mechanisms. With hydrogen loading, it is now possible to inscribe strong FBGs in those fibers with low dopant concentrations. Fig. 2.12 shows the reflectivity evolutions of FBGs in hydrogen-loaded, hydrogen out-diffused and pristine SMF-28 fibers as a function of the introduced inscription fluence [86]. It can be seen that the reflectivities of FBGs in those hydrogen-loaded fibers increase much faster than those in pristine and out-diffused fibers under the same inscription fluence. About 1000 times the fluence is needed for pristine and out-diffused fibers to achieve the same grating strength as hydrogen-loaded fibers. This result also shows that the enhanced photosensitivity due to hydrogen loading is not a permanent effect, and as the hydrogen diffuses out, the photosensitivity decreases to normal.
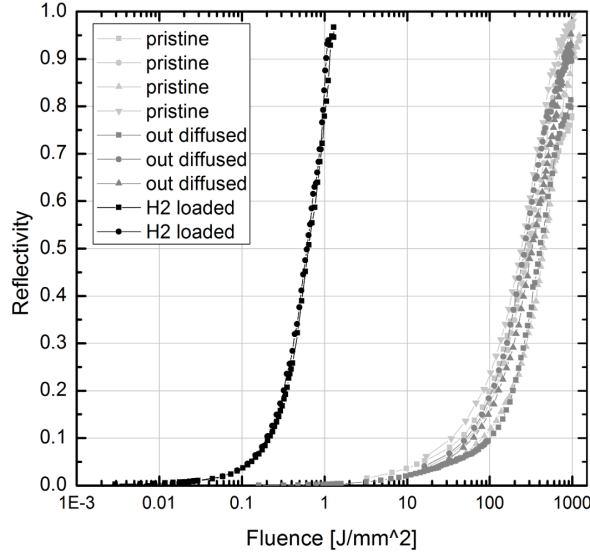
Figure 2.12: Reflectivity evolutions of FBGs in hydrogen loaded, hygrogen out-diffused and pristine SMF-28 fibers [86].

**Decay of Type-I FBG at high temperatures**

The high-temperature resistance of Type-I FBG is relatively low. When the temperature is above 100 ℃, the refractive index modulation of Type-I FBG decays gradually because the UV-induced photo-chemical process mentioned before is reversible at high temperatures. The decay of the UV-induced refractive index follows a "power-law" function of time [32]:

$$\eta' = \frac{1}{1 + At^{\alpha'}}, \tag{2.46}$$

where $\eta'$ is the normalized UV-induced refractive index change, factor $A$ and exponent $\alpha'$ are both dependent on temperature.

Fig. 2.13(a) shows the decay of Type-I FBG as a function of time at 350 and 550 ℃. Here, the normalized ICC is the abbreviation of the integrated coupling constant, and it is proportional to the UV-induced index change, and the solid lines are fits based on Eq. 2.46. It can be seen that, at a constant high temperature, the UV-induced refractive index decays rapidly at the beginning and reaches saturation gradually. Decay at higher temperatures is more rapid and to a greater extent, corresponding to larger values of $A$ and $\alpha'$ in Eq. 2.46.

Erdogan et al. proposed a theoretical model to explain the decay mechanism, whose schematic diagram is shown in Fig. 2.13(b). Electrons excited from GODC by UV irradiation are assumed to be trapped in $Ge(1)^-$ and $Ge(2)^-$ in the form of a continuous (Gaussian) distribution of trap states rather than a single trap level. $E_d$ is the demarca-
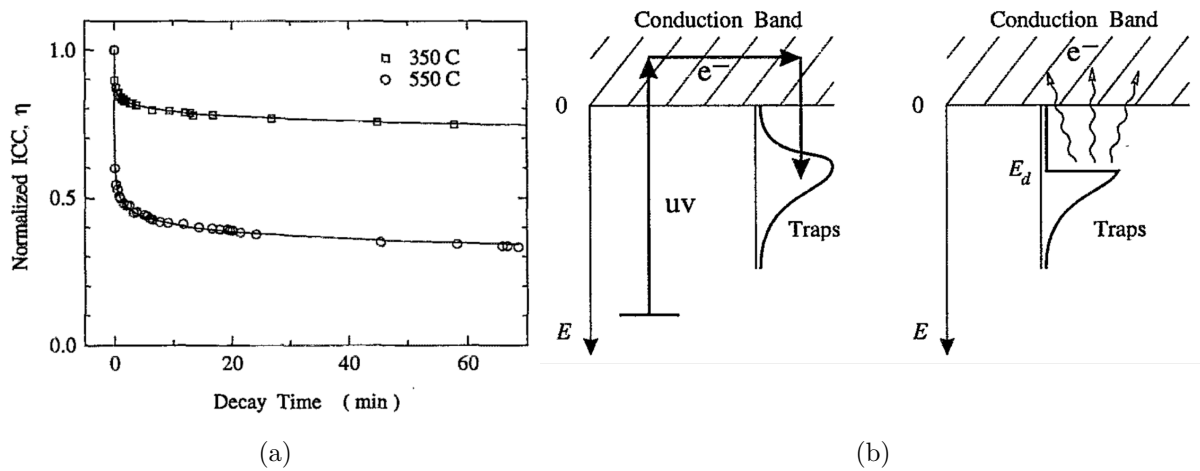
Figure 2.13: (a) Decay of Type-I FBG as a function of time at 350 and 550 ℃. (b) Schematic diagram of the model for decay mechanism of Type-I FBGs at high temperatures [32].

tion energy to separate those electrons into two groups: at high temperatures, some of the electrons at shallower traps ($E < E_d$) will be excited via thermal excitation, while others at deeper traps ($E > E_d$) remain. The detrapping rate $v(E)$ is dependent on the temperature $T$ and the depth of the trap state $E$, and it can be expressed as follows:

$$v(E) = v_0 e^{-\frac{E}{k_B T}}, \tag{2.47}$$

where $k_B$ is the Boltzmann constant.

## 2.3 Metal casting

### 2.3.1 Phase diagram

A phase diagram is a kind of chart used to show conditions (temperature, volume, pressure, etc.) at which thermodynamically distinct phases (solid, liquid, gaseous states, etc.) occur and coexist at equilibrium in physical chemistry, metallurgy, foundry, and materials science [87].

The simplest phase diagrams are 2-dimensional pressure–temperature diagrams of a single simple substance, such as water and carbon dioxide. Fig. 2.14 shows a typical phase diagram of water. The triple point is when the three phases gas, liquid, and solid coexist. The critical point is when the substance is indistinguishable between liquid and gaseous states. The dotted green line shows the anomalous behavior of water. The green line

represents the transition between liquid and solid states (melting point). The blue line
represents the transition between gaseous and liquid states (boiling point). The red line
is for the sublimation point. It can be seen how those points vary with pressure.
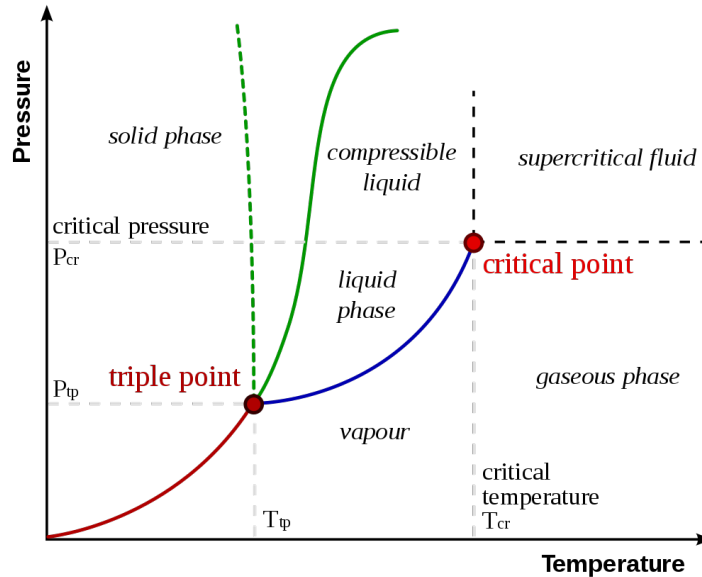


Figure 2.14: Typical phase diagram of water [87].

## 2.3.2   Solidification of eutectic mixtures

When there is more than one pure component/substance present in a material, concentra-
tion becomes a critical variable. Phase diagrams with more than two dimensions can be
constructed to show the effect of more than two variables on the phase of the mixed mate-
rial. Binary phase diagrams, which present temperature against the relative concentration
of two substances in binary mixed materials, are commonly used in metal casting. Metal-
lurgists use them to predict what phases should be present in an alloy equilibrium and to
interpret the micro-structure of metal alloys observed under a metallographic microscope
[88].

Fig. 2.15 shows the phase diagram of lead(Pb)-tin(Sn) alloy as an example. Pb and tin
have different crystal structures, and Pb atoms are much larger than Sn atoms, so these
two metals are only partially soluble in each other when in the solid state. No more than
19.2 wt./% of solid Sn can dissolve in solid Pb, and no more than 2.5 wt./% of solid Pb
can dissolve in solid Sn. Alloy 1 in Fig. 2.15, it is an eutectic mixture with an eutectic
composition (61.9 wt./% Sn, 38.1 wt./% Pb) for which complete liquification occurs at a
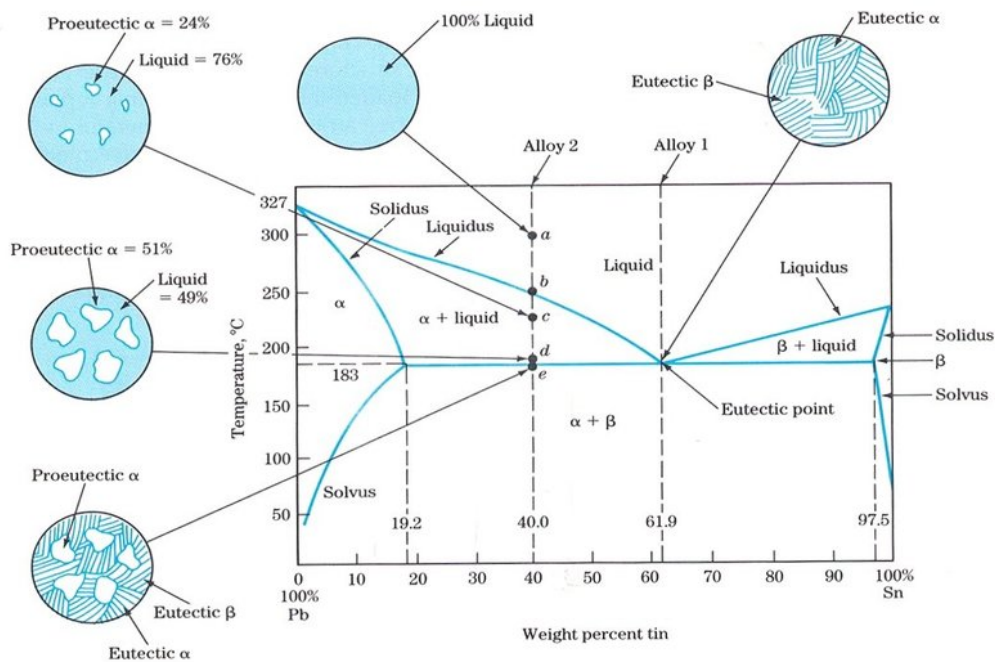lower temperature (the eutectic temperature 183 ℃) than any other composition, making

Figure 2.15: Phase diagram of Pb-Sn alloys with sketches of the microstructure observed depending on the composition of the alloy [89].

this mixture useful as solder. At the eutectic temperature, $\alpha$-phase (19.2 wt./% Sn) and $\beta$-phase (97.5 wt./% Sn) Sn-Pb could be obtained at the same time. Alloy 2 is a mixture with 40 wt./% Sn, for temperatures above the liquidus line, the mixture is a completely intermixed liquid. Below the liquidus line, there will be some solid $\alpha$-phase Sn-Pb (12 wt./% Sn proeutectic), and the rest is a mixture of Sn-Pb liquid. As temperature decreases, the amount of solid $\alpha$-phase Sn-Pb in the liquid-solid mixture ($\alpha$+liquid) increases, and the percentage of Sn in the $\alpha$-phase increases as well until the temperature reaches 183 °C. Then, in this case, the percentage of Sn in the $\alpha$-phase becomes 19.2 wt./%, and the rest part is an eutectic mixture, which follows the rule as Alloy 1.

Fig. 2.16 shows the binary aluminum(Al)-silicon(Si) phase diagram. It is a relatively simple binary system where there is very little solubility at room temperature for Si in Al and for Al in Si. Thus, the terminal solid solutions are nearly pure Al and Si under equilibrium conditions. The melting points of Al and Si are, respectively, 660 and 1414 °C. The Al-Si phase diagram can be divided into two regions: the aluminum-rich region and the silicon-rich region. In the aluminum-rich region, the primary solid phase is $\alpha$-Al and the liquid phase is denoted as L. In the silicon-rich region, the primary solid phase is $\beta$-Si and the liquid phase is also denoted as L. At intermediate compositions and temperatures,

various intermetallic phases form, such as Al-Si eutectic, hypereutectic, and hypoeutectic phases. The eutectic phase(reaction) occurs at 12.6 wt./% Si and ~557 °C.
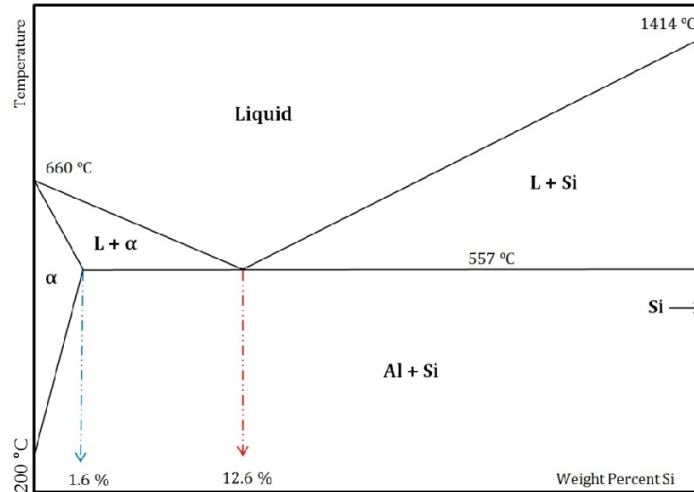


**Figure 2. The schematic phase diagram of Al-Si.**

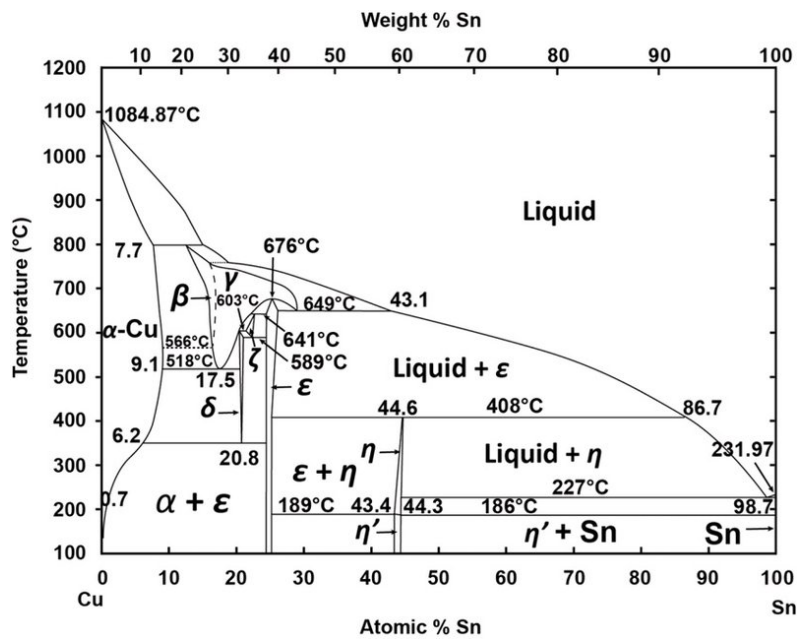Figure 2.16: Phase diagram of Al-Si alloys [90].



Figure 2.17: Phase diagram of Cu-Sn alloys [91].

As a comparison, the phase diagram of copper(Cu)-tin(Sn) is much more complicated, as shown in Fig. 2.17. Several peritectic and eutectoid transformations, whose products are $\alpha$, $\beta$, $\gamma$, $\delta$, $\varepsilon$ and other phases can be found. The binary system contains various phases, especially at the copper-rich region. Bronzes, as the most famous Cu-Sn alloy,

typically have Sn content between 1 and 9 at.% for technical application. Those alloys are mostly employed for mechanical working and characterized with $\alpha$ structural solution. An increase in Sn content in the bronzes that are cooled under standard conditions causes the formation of heterogeneous structure $\alpha$ and other structures, such as brittle $\delta$ phase [92].

# Chapter 3

# High-temperature resistant FBG and fiber optic smart cast

## 3.1 High-temperature resistant FBG

As mentioned in Section 2.2.2, Type-I FBGs decay at high temperatures due to the reversible UV-induced photo-chemical process. To avoid this problem, in the past few decades, other high-temperature resistant FBGs have been proposed, including regenerated FBGs, Type-II FBGs in silica fibers and sapphire fibers, which will be introduce in this section.

### 3.1.1 Regenerated fiber Bragg grating (RFBG)

Regenerated fiber Bragg gratings (RFBGs) are another type of FBGs independent of Type-I FBGs. They are produced by putting pre-treated seed gratings (Type-I FBGs) in a thermal annealing process at hundreds of degrees Celsius. The reflectivity of a seed grating decays to almost zero gradually and then regrows to a relatively low level, which is the origin of the term "regenerated". To date, there is no comprehensive explanation for the mechanisms of the regeneration effect. Two alternative theories, the chemical composition theory and the crystallization theory have been established, as reviewed recently by Polz et al. [93].

In 1997, Fokine et al. proposed the chemical composition theory to interpret the regeneration phenomenon first observed in a hydrogen-loaded germanium-fluorine co-doped fiber [94], whose schematic diagram is shown in Fig. 3.1(a). According to Section 2.2.2, hydroxyl (OH groups) are formed during the UV inscription in the illuminated areas of hydrogen-loaded fibers. At high temperatures, chemical reactions happen between OH

groups and fluorine, producing hydrogen-fluoride (HF), which then diffuses out of the core. It is believed that the refractive index modulation is caused by a fluorine depletion in the UV-illuminated areas [95]. It was later found that RFBGs can also be fabricated



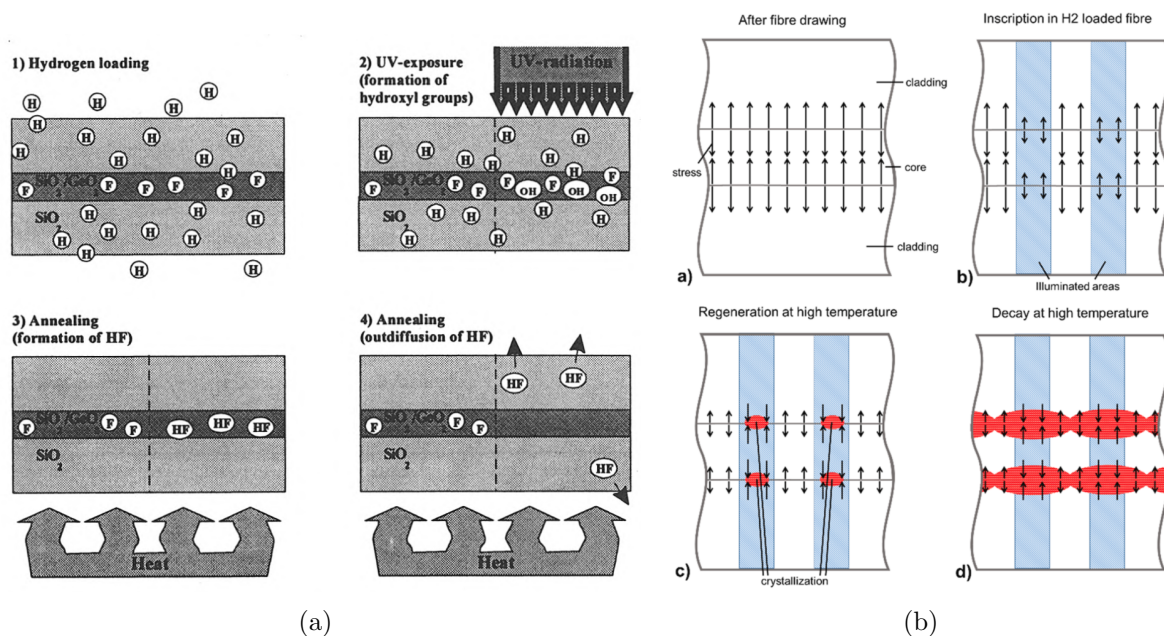(a)                                                    (b)

Figure 3.1: Schematic diagrams of (a) chemical composition theory [94], (b) crystallization theory [93].

in fibers without fluorine dopant. Fokine thought there was a reduced amount of oxygen in the illuminated areas due to the water formed by OH groups [96].

In 2008, Canning et al. proposed the crystallization theory to interpret the formation of RFBG [97]. As shown in Fig. 3.1(b), due to the property difference between fiber core and cladding, radial tensile stress is introduced in the core-cladding interface in the fiber drawing process. The tensile stress can be relaxed in the UV-illuminated areas during the inscription process due to the formation of OH groups. High temperature can further release the radial tensile stress in the core-cladding interface and even turn those in the illuminated areas into compressive radial stress. Compressive stress, together with high temperature, leads to glass crystallization, and crystals like cristobalite and tridymite with higher density and refractive index are formed in the previously-illuminated areas. It should be noticed that these crystals can continuously grow into the non-illuminated areas at and above regeneration temperatures, which further slowly decreases the reflectivity, as shown in the last diagram of Fig. 3.1(b).

Both theories are supported by different experimental observations, and neither can explain all the regeneration phenomena [93]. However, since both theories are related to the

formation of OH groups, it is believed that hydrogen loading plays an important role in
the RFBG fabrication process. Fig. 3.1.1 shows the reflectivity evolutions of the FBGs
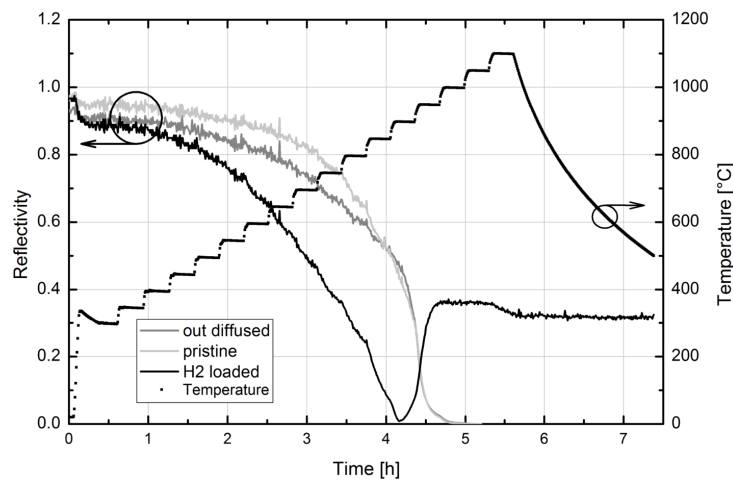in hydrogen-loaded, pristine, and out-diffused fibers during the heat treatment process.
It can be seen that FBGs in pristine and in out-diffused fibers decay with similar ther-
mal stability and do not regenerate, while only the FBG in the hydrogen-loaded fiber
has shown regeneration, which seems to prove that the formation of OH groups is really
important for RFBG. In addition to hydrogen loading, the dopant concentration [98], the



Figure 3.2: Reflectivity evolutions of the FBGs in hydrogen-loaded, pristine and out-
diffused fibers during the heat treatment process [86].

strength/length of seed grating [99, 100], the applied tensile stress [101], the annealing
temperature [102], and the heat treatment process (isochronal annealing, isothermal an-
nealing, etc.) [103] are all found to influence the quality of the fabricated RFBG. For
example, the regeneration temperature is found to be lower for fibers with higher dopant
concentration due to the lower glass transition temperature of the fiber core [104].

Due to the advantages of corrosion resistance, immunity to electromagnetic interference,
and wavelength multiplexing capability, RFBGs-based temperature sensors are regarded
as an alternative to the traditional high-temperature monitoring method - thermocou-
ples. RFBGs for high-temperature applications have been investigated in the past twenty
years. Aslund et al. monitored temperature distribution within the reaction zone during
the fabrication of optical fiber preforms using RFBG sensors [105]. Rinaudo et al. placed
RFBG temperature sensors near the surface of concrete specimens and tested them under
the ISO 834 fire curve conditions for building fire [106]. Haddad et al. tested RFBG
temperature sensor arrays in a reentry plasma environment and a wind tunnel, respec-
tively, and integrated them with ROTEX-T structure for atmospheric reentry experiments
[107]. Alberto et al. coated RFBGs with diamond coatings with hot filament chemical

vapor deposition method and monitored the temperature evolution during the coating
process [108]. Corre et al. used RFBG arrays to measure the temperature distribution
of plasma-facing units during tokamak plasma operation [109]. Lindner et al. placed
RFBG temperature sensors inside cast mold and monitored the temperature distribution
during an aluminum solidification process [8]. Dutz et al. demonstrated the capability
and reliability of RFBG sensor arrays for temperature monitoring in chemical reactors by
comparing the two-year measurement results with that from thermocouples [110]. Dutz
et al. also used RFBG arrays to map the radial temperature profiles in the exhaust-gas
diffusor of the gas turbine with high spatial and temporal resolution [111, 112]. RFBGs
can also be used for sensing other physical parameters. Polz et al. fabricated RFBGs in
polarization-maintaining fibers and achieved simultaneous measurement for temperature
and force [113]. Li et al. used phase-shifted RFBGs to develop an in-situ laser-ultrasonic
visualization method for the detection of the artificial defect in the SiC plate at high
temperatures [114]. Besides, investigations have also been carried out using RFBGs in
fiber-based devices, like distributed Bragg reflector fiber lasers operated at high temper-
atures [115].

There are several challenges when using RFBGs in a high-temperature and harsh environ-
ment. Firstly, owing to the corrosion effects on the fiber surface, as mentioned in Section
2.1.2, the fibers become brittle after regeneration and high-temperature annealing [116],
largely decreasing the mechanical strength and durability of the sensors. Experiments
have shown that the fracture stress (tensile strength) of fiber underwent the regeneration
and annealing process dropped to ∼0.17 GPa [61]. As a comparison, As a comparison,
the fracture stress of normal fibers is 5∼6 GPa [51, 117].

To protect RFBGs sensors from fracture, some packaging and coating methods have been
proposed. The most popular packaging method is to insert RFBGs into glass [118], or
metal capillaries [8, 110–112, 119]. Recoating fibers after the regeneration process has also
been studied, including coating fibers with diamond [108], polyimide [120], silver [121],
and other metal alloys [122]. Besides, it has also been proved that special fibers with
250 µm had similar fracture stress (0.18 GPa) as standard fibers but four times larger
tensile force tolerance because of the twofold fiber diameter, which could also improve the
robustness of fiber sensors [61].

The second challenge for using RFBG at high temperatures is that, even though the
grating strengths of RFBGs do not drop significantly at high temperatures, their Bragg
wavelengths suffer from slow wavelength drifts when exposed to high temperatures over
long periods, affecting the long-term functionality of the sensors.

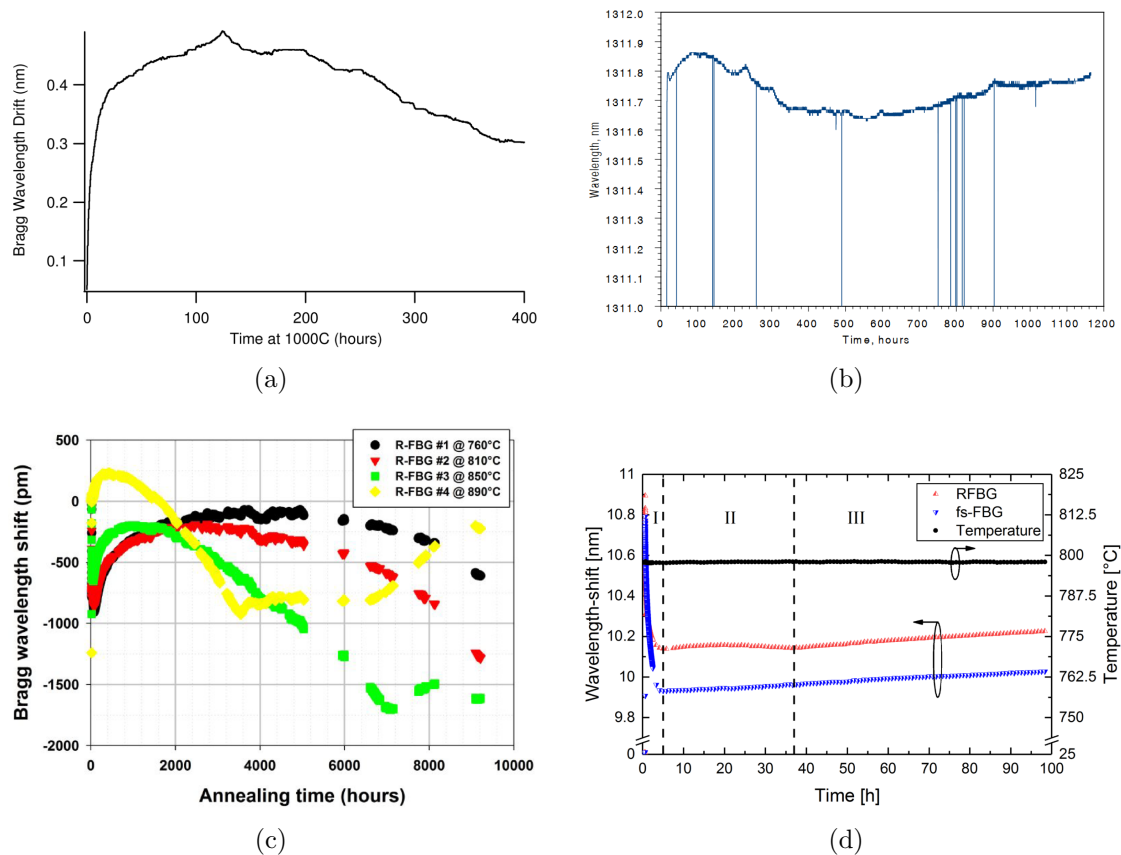Several long-term stability tests have been carried out for RFBGs at high temperatures. In

Figure 3.3: Evolutions of the Bragg wavelength drifts of (a) a RFBG at 1000 °C for 400 hours [123], (b) a RFBG at 1000 °C over 1000 hours [124], (c) RFBGs at 710, 810, 850, and 890 °C over 9000 hours [125], (d) a RFBG (Type-I FBG as seed grating) and a Type-II FBG [111].

2004, Juergens et al. annealed RFBG at 1000 °C for 400 hours, and the Bragg wavelength experienced a red drift of ∼480 pm during the first 125 hours and then a 190 pm blue drift during the remaining hours [123], as shown in Fig. 3.3(a). Then in 2011, Adamovsky et al. packaged RFBG sensors into ceramic tubes and annealed them at 500 °C for 500 hours and at 1000 °C over 1000 hours, successively. Fig. 3.3(b) shows an example of the Bragg wavelength evolution over 1000 hours at 1000 °C [124]. The Bragg wavelength underwent a ∼100 pm red drift in the first 50 hours at 1000 °C, then a ∼200 pm blue drift in the next 300 hours, relatively stable fluctuation during the subsequent 400 hours, a ∼100 pm red drift again over the remaining hours. In 2013, Laffont et al. also annealed RFBGs for 9000 hours at 760, 810, 850, and 890 °C, respectively. They found that the reflectivities were relatively stable, while wavelength drifts behaved differently at different temperatures, which may be attributed to the viscosity change of the silica substrate and to packaging issues [125]. As shown in Fig. 3.3(c), for RFBGs at 760 °C and 810 °C,

the Bragg wavelengths underwent red drifts in the first 2000 hours, remained relatively constant for another 2000 hours and then experienced blue drifts in the remaining hours. For RFBGs at 850 and 890 ℃, the time durations of the first three phases were shorter, and another red drift followed afterward. Dutz et al. carried out a two-year test by putting RFBG sensors into chemical reactors, with temperatures ranging from 150 to 500 ℃ and the temperature deviations caused by wavelength drifts were only from 0 ℃/year to 2.3 ℃/year [110]. No obvious wavelength drift was found by Laffont et al. for RFBG sensors immersed in hot sodium (∼500 ℃) for 2.5 hours, either [119]. In addition, Dutz et al. also observed that the drift behaviors of RFBG and Type-II FBG were very similar at 800 ℃ for 100 hours, as shown in Fig. 3.3(d), indicating that the fiber properties themselves rather than the grating types mainly determined the wavelength drift [111].

Several factors have been mentioned to interpret the drift behavior, like residual stress relaxation [33, 126], change of $T_g$ [127], dopant diffusion [128], and fiber contraction or densification [47, 102], but part of them are mutually contradictory. Besides, due to the reduced viscosity of silica at elevated temperatures above 600 ℃ [78], small internal and external forces can lead to plastic deformations of the fiber and thus to wavelength drifts of the RFBG.

### 3.1.2 Type-II FBG in silica fiber

Ultrafast lasers, typically in the visible or near infrared (NIR) spectral range, are used to inscribe FBGs in silica fibers either by using phase mask method [129], or point-by-point (PbP) method [130]. The use of visible or NIR radiation means the photo excitation in the silica band gap is a multiphoton process and therefore highly localized, leading to a much stable refractive index modulation of the grating. Considering the modulation mechanism of these gratings is different from that of Type-I FBGs, they are called Type-II FBGs.

The energy band gap for a standard telecom fiber is usually assumed to be around 7.1 eV [131]. Fig. 3.4 shows the scheme of photo excitation pathways in standard telecommunication optical fibers. They can be divided into three groups: 1. Single-photon absorption at wavelengths of 248 and 193 nm, where the single photon is absorbed by the defects in germanium-doped fibers, and the light intensity absorbed is linearly dependent on the incident light intensity. 2. Two-photon absorption at wavelengths of 267, 264, and 211 nm, where the instantaneous absorption is achieved by exciting an electron into an intermediate energy level with the first photon and almost simultaneously moving it to a conduction band using the second one. 3. Multi-photon absorption at wavelengths of 800 and 514 nm, where several photons are absorbed simultaneously at a very high irradiation intensity provided by ultrafast lasers [79]. Type-II FBGs are usually inscribed by
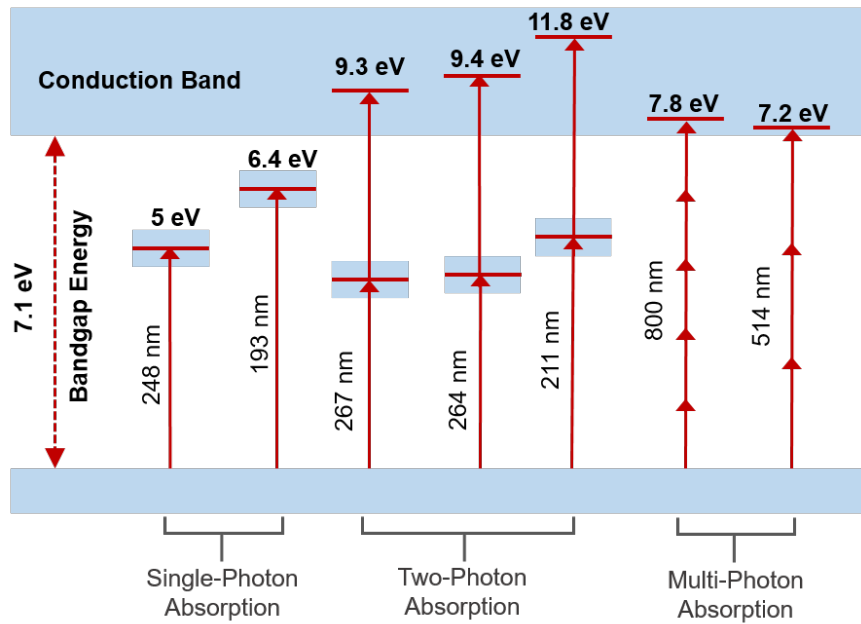
Figure 3.4: Scheme of photo excitation pathways in standard telecommunication optical fibers, adapted from [79].

femtosecond laser based on multi-photon absorption, so they are also called femtosecond laser-inscribed FBGs (fs-FBGs). When the pulse intensity exceeds a threshold value (typically in the order of $10^{13}$ W/cm² at the wavelength of 800 nm [132]), electrons are excited to the conduction band by means of multi-photon absorption, and they absorb further kinetic energy and excite further charge carriers via collision processes, which in turn largely increases the absorption efficiency. This avalanche effect leads to the formation of a hot electron plasma, and the material is ionized [129, 133].

The subsequent transfer of electron energy to the atomic cores or ions leads to three-dimensional micro-structural modifications of the glass structure. Cavities or voids are formed by micro-explosions when the pressure in absorption volume significantly exceeds Young's modulus of the glass materials [134]. These structural changes correspond to the negative refractive index change. Unlike the UV-induced refractive index change, which is revisable at high temperatures, the refractive index modulation of Type-II FBG is much more stable at high temperatures. Grobnic et al. demonstrated that Type-II FBG had a remarkable thermal stability up to 1000 °C for 150 hours. A reflectivity decay and a permanent drift of Bragg wavelength were observed at temperatures of 1050 °C or greater [135]. It has been shown by Lu et al. that pre-annealing at high temperatures (5 hours at 1100 °C) contributed to the high-temperature stability and the Type-II FBGs were stable up to 1200 °C during 20 hours [126]. It should be noticed that the reflectivities of

Type-II FBGs typically showed slight losses during the initial strength before stabilizing [135, 136].

### 3.1.3   Type-II FBG in sapphire fiber

The multi-photon absorption also applies to other materials, so Type-II FBGs can be inscribed in materials with higher melting points to achieve better high-temperature performance. As mentioned in Section 2.1.3, sapphire fiber has a good application prospect at high temperatures and harsh environments due to its properties like high melting point (2040 ℃), high mechanical strength, and resistance to chemical corrosion. Type-II FBGs inscribed in sapphire fibers based on multi-photon absorption are also called sapphire fiber Bragg gratings (SFBGs) [137]. Similar to the inscription of Type-II FBG in silica fiber, there are typically two different methods for inscribing SFBGs: phase mask method and PbP method. In the recent years, line-by-line (LbL) scanning method has been proposed as an improvement on PbP method [138].

In 2004, the first SFBG was inscribed by Grobnic et al. using a 800 nm femtosecond laser and the phase mask method. The diameter of the sapphire fiber was 150 μm and the SFBG was a fifth-order grating with a pitch period of 2.14 μm, whose microscope image is shown in Fig. 3.5(a). It was heated up to 1500 ℃ and no detectable grating strength reduction was observed [137]. In 2009, Busch et al. also used the phase mask method to fabricate a second-order SFBG with a period of 1.758 μm. It achieved temperature measurement up to 1745 ℃, with repeatability better than 1 ℃ [139]. However, the reflection spectra suffered from very strong distortion during the temperature steps, as shown in Fig. 3.5(b).

The Bragg wavelength of the SFBG obtained by the phase mask method depends on the fixed pitch of phase mask used, so different phase masks need to be fabricated for different wavelengths, which limits their application in multi-point (quasi-distributed) sensing. PbP method, with a simple and flexible fabrication process for adjusting parameters, has been used for SFBG fabrication by Yang et al. in 2017 [34]. Fig. 3.6(a) shows the schematic diagram of PbP method. The sapphire fiber is mounted on a five-axis translation stage and it moves along the axial direction at a constant scanning speed ($V_s$) during the inscription. Laser pulses with a constant repetition rate ($f_{rep}$) are adjusted by a half-wave plate (HWP) and a linear polarizer (LP), and focused by an oil-immersion objective. The pitch period of inscribed SFBG can be easily adjusted by adjusting the relationship between $V_s$ and $f_{rep}$ ($\Lambda = V_s/f_{rep}$). Fig. 3.6(b) and 3.6(c) show the microscopic images of a SFBG inscribed by the PbP method. The diameter of the sapphire fiber was 125 μm and the SFBG was a fourth-order grating with a pitch period of 1.776 μm.
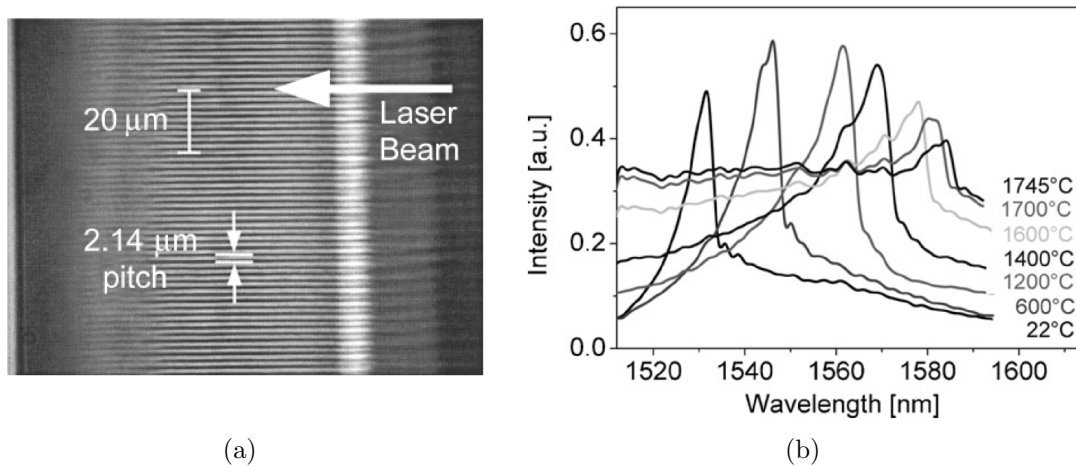
Figure 3.5: (a) Microscope image of the SFBG [137], (b) Reflection spectra of sapphire fiber Bragg gratings at temperatures up to 1745 °C [139].

SFBGs with different Bragg wavelengths can be easily fabricated by adjusting the inscription parameters during the PbP method, which makes it possible to obtain SFBG arrays for distributed sensing. However, due to the small absorption region by a single laser pulse, the regions with refractive index modulation are also small, which makes it difficult to obtain a SFBG with high reflectivity. To increase the reflectivity, PbP method has been improved to LbL method by Xu et al. in 2018 [138]. This method combined points into lines by scanning from the direction perpendicular to the fiber axis, largely increasing the modulation area. A 5-point SFBG array was inscribed using the LbL method, whose schematic diagram and reflection spectra from both sides are shown in Fig. 3.7. In 2019, Guo et al. improved the LbL method to fabricate a SFBG with 15% reflectivity and carried out a temperature cycle in the range from 30 °C to 1600 °C [140]. In the same year, Xu et al. proposed a multi-layer structure by LbL method to further improve the reflectivity. It was found that the refractive index modulation area of the SFBG was enlarged by double layers and the reflectivity increased to 34.1% [141].

It should be noticed that a sapphire fiber is normally a single crystal without internal structure as a normal silica fiber. It can be regarded as a kind of multi-mode fiber with sapphire as core and air as cladding. Based on Eq. 2.11, the number of modes $M$ inside sapphire fiber can be estimated. For single-crystal sapphire fibers, by assuming a constant refractive index of 1.746 for sapphire according to Eq. 2.20 and simplifying the hexagonal shape of the cross section as a circular shape, it can be calculated that, at 1550 nm, the $M$ is around 23000 for the 75 µm-diameter, 15000 for 60 µm-diameter, 10000 for the 50 µm-diameter, and 6000 for the 40 µm-diameter sapphire fibers, respectively. Therefore, SFBGs normally have very broad reflection spectra containing thousands of modes, whose

(a)



(b)



(c)
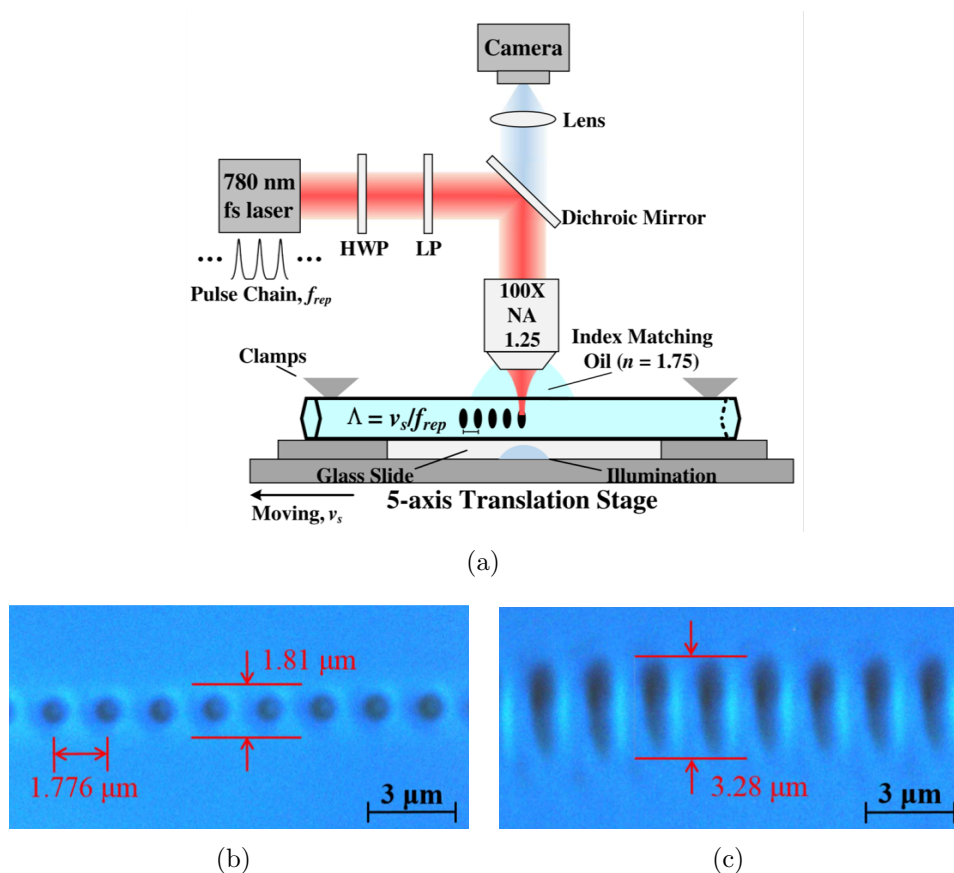
Figure 3.6: (a) Schematic diagram of PbP method for SFBG inscription (fs, femtosecond; HWP, half-wave plate; LP, linear polarizer.). Microscopic images of the SFBG inscribed by PbP method from (b) a top view and (c) a side view [34].

bandwidths are a few nanometers and shapes are susceptible to external disturbances.

Researches have been carried out to obtain clear and stable reflection spectra with narrow bandwidth from SFBGs. Grobnic et al. "butt-coupled" tapered single-mode fiber and sapphire fiber through a five-axis precision stages to obtain single-mode/low-order mode spectra from SFBGs, whose FWHM could reach 0.33 nm [142]. Zhan et al. proposed a method by bending sapphire fiber to filter high-order modes and obtained a resonant peak bandwidth less than 2 nm [143]. However, those two methods mentioned above are difficult to be applied in practice due to harsh implementation conditions. Yang et al. reduced the diameter of a sapphire fiber to 9.6 µm by wet-hot acid etching, achieving a reduced FWHM of the spectrum from SFBG with less fiber modes [144]. Recently, Guo et al. used a single-mode coupler to measure the reflection spectrum from sapphire fiber with helical gratings. Some high-order modes were filtered out through this coupling method, which resulted in the reduction of FWHM. However, the left modes were easily influenced by the external disturbance due to the mismatch between single-mode fiber and sapphire
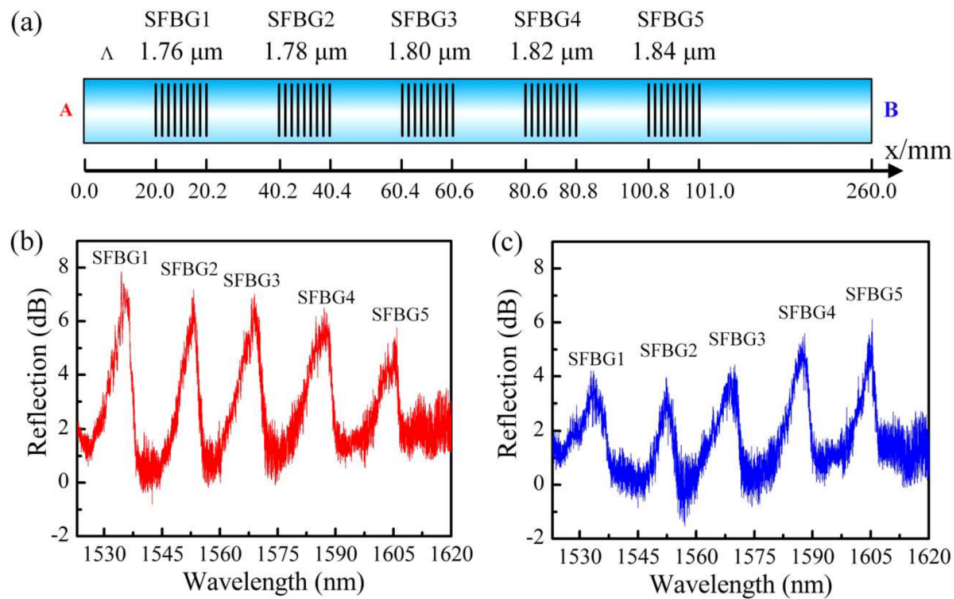
Figure 3.7: (a) Schematic diagram of a 5-point SFBG array fabricated by LbL method. Reflection spectra of the SFBG array measured from (b) end A, and (c) end B [138].

fiber [145]. A sapphire fiber with a FBG array spliced with a single-mode fiber was mentioned in [146], and the signal of FBG array as a function of distance could be clearly detected via an optical backscatter reflectometer when the properly aligned splicing point was achieved, while the author did not introduce the spectral quality of FBG and the mode filtering effect. Wang et al. designed a multi-layer recessed cladding structure and wrote a single-mode waveguide with a Bragg grating in a sapphire fiber, thereby realizing the single-mode output of the sapphire fiber grating, and obtaininged a reflection peak with a bandwidth less than 0.5 nm [147]. This method required complicated manufacturing process and it was difficult to achieve a long-distance waveguide writing due to the ultra-high loss.

## 3.2 Fiber optic smart casting

In the past decades, investigations have been carried out using the optical fiber sensors to monitor the casting, called fiber optic smart casting. Roman et al. conducted a series of experiments using optical frequency domain reflectometry to achieve the thermal mapping of metal casting mold for continuous casting. This distributed optical fiber sensing method based on Rayleigh scattering could provide temperature measurements along the optical fiber with a high spatial resolution (0.65 mm) and a fast measurement rate for casting (25 Hz) [148, 149]. The highest temperature they measured with this method could reach

710 °C [150].

FBGs, as one of the most widely used optical fiber sensors, have been applied to monitor the casting processes. Thomas et al. embedded FBG sensors inside a nickel coating layer that was electroplated onto the continuous cast mold to monitor the transient temperature and heat flux behavior of casting molds [151]. Lieftucht et al. embedded twelve fibers, each containing ten temperature FBG sensors at different positions of the mold in a continuous casting to monitor heat flux density distribution and estimate liquid steel level [152]. Spierings et al. achieved high-density temperature measurement for slab casting by embedding a large number of FBG temperature sensors in a copper mold plate, so the fluid flow and temperature distributions at different casting conditions (steel grades) can be obtained [153].

The Institute for Measurement Systems and Sensor Technology, Technical University of Munich (TUM) and the Photonics Laboratory, Munich University of Applied Sciences (MUAS) have used FBG sensors to monitor aluminum casting processes in cooperation with the Chair of Metal Forming and Casting, TUM. Weraneck et al. showed that Type-I FBGs could sustain in direct contact with aluminum and measure the strain evolution during solidification. Different lengths of the gratings were applied, and it was shown that shorter gratings resulted in more accurate measurements [7]. It should be noticed that the performance of Type-I FBGs dropped at high temperatures, including reflectivity decay and wavelength drift. To solve this problem, fs-FBGs and RFBGs with improved high-temperature resistance were further used. Heilmeier et al. used fs-FBGs to monitor in-situ strains during aluminum casting processes and calibrated the results by neutron diffraction method [6]. Lindner et al. used a regenerated RFBG temperature sensor array to monitor the temperature distribution during an aluminum alloy casting process. Position-depending delays of solidification-induced temperature rises were observed, which were interpreted as the movement of the solidification front inside the cast material. In addition, the results showed that the temperatures measured by RFBGs and a reference thermocouple had excellent agreements and RFBGs had almost no reflectivity decay or wavelength drift after the casting [8].

However, there are still many issues to be studied. Fibers with higher strength are needed for casting monitoring due to the huge compression during the cooling and the hot corrosion caused by high temperature. FBGs are inherently sensitive to temperature and strain, so the method to decouple strain from temperature during casting needs to be more accurate. Strain distribution information during casting process has not been well studied, and the correlation between the strain information and the solidification characteristics is still unknown. Moreover, previous research only focuses on aluminum casting, the maximum temperature of which is around 650 °C. While other metal materials with higher

melting points and cast temperatures, such as copper and steel, remain challenging.

## 3.3 Fiber optic smart structures

In the recent years, optical fiber sensors have been applied in structural health monitoring (SHM) in civil infrastructures [154–156], energy power [157, 158], aerospace [112, 159], and downhole applications [160]. Compared with those surface-attached sensors and nondestructive methods, embedded sensors can provide in-situ information at critical locations inside the structure in real time with a compact sensing system. Optical fiber sensors embedded in composite structures have been widely investigated in the past ten years [15–18], especially in the field of reinforced laminates [19]. For metallic structures, however, the embedding process is more challenging due to the much higher melting points of metals and the large mismatch of material properties. Laser-based embedding methods, like laser layered manufacturing [20, 21] and selective laser melting [22], have been applied in this field. In general, a metallic jacket, nickel, or silver, for instance, needs to be coated onto fibers in advance to act as a conductive layer, but debris and gaps can still be found at the interface after embedding [29]. Besides, correct laser properties must be appropriately selected to ensure fusing the metal powder without damaging the optical fibers, demanding significant efforts [21, 29]. Another embedding method, called ultrasonic consolidation (UC) [23] or ultrasonic additive manufacturing (UAM) [24], has become a hot topic in recent years. Optical fibers can be bonded with metal foils layer by layer using ultrasonic oscillation [161]. The UC technique can also be combined with laser techniques to modify the surface of metal foils, achieving accurate placement and reduced distortion [162]. The relatively low-temperature requirement is an important feature of this method. However, specific foil thickness, width, and surface roughness are required to achieve valid bonding [163]. The casting process has also been proposed to embed fiber sensors into metals [25]. The challenges of this method include the high melting points of metals, the melt impurity in casting, and the high contraction during the cooling down process. Nonetheless, the advantages of the casting method are apparent. Mass manufacturing is possible with the casting process, and those structures with complex and large shapes needed in the industry, like turbines and engines, can be fabricated. By placing the fiber sensors in advance into the proper position of the cast model, these sensors can be easily embedded deeply inside metallic structures.

As mentioned in the last subsection, the Institute for Measurement Systems and Sensor Technology, TUM and the Photonics Laboratory, MUAS have used FBG sensors for casting monitoring in the past several years. Those FBG strain sensors in bare fibers survived after the casting processes, which could be further used as metal-embedded fiber

sensors for structural health monitoring in metal structures. Heilmeier et al. carried out tensile tests using aluminum cast specimens with embedded FBG strain sensors [26] and evaluated the strain transition properties between fibers and the cast parts by neutron diffraction [27]. Lindner et al. investigated the strain and temperature response of fiber-embedded aluminum cast parts [28]. However, FBGs have not been embedded in other metallic materials other than aluminum. Besides, temperature and external strain decoupling is still an issue that needs to be solved.

# Chapter 4

# Investigations on the high-temperature characteristics of RFBG

Among the various types of FBGs developed, RFBG shows significant advantages of high-temperature resistance, easy fabrication, and ability to achieve accurate and multipoint sensing [93].

In this chapter, investigations have been carried out to know the characteristics of RFBG better. The RFBG fabrication process was introduced. The influence of dopant concentration on the wavelength drift and the temperature sensitivity was investigated. An one-year wavelength drift measurement was carried out to study the long-term stability of RFBG at high temperatures. The characteristics of SFBG was also investigated and compared with RFBG, including the wavelength drift at 900 ℃ and the temperature sensitivities in different temperature ranges.

## 4.1 Characteristics of RFBG

### 4.1.1 Fabrication of RFBG

Type-I seed FBGs are needed for the fabrication of RFBGs, as mentioned in Section 3.1.1. In our research, UV irradiation and phase mask method are used to inscribe Type-I FBGs. Fig. 4.1 shows the schematic diagram of the FBG inscription setup in the Photonics Laboratory. An excimer-laser (MLI-200KrF FBG, MLase AG, Germering, Germany) emits UV light pulses at 248 nm, with a pulse duration around 10 ns, a pulse energy up to 16 mJ, and a repetition rate up to 200 Hz. The light beam is directed

via two mirrors so it can be aligned perpendicular to the fiber.  A cylindrical lens with
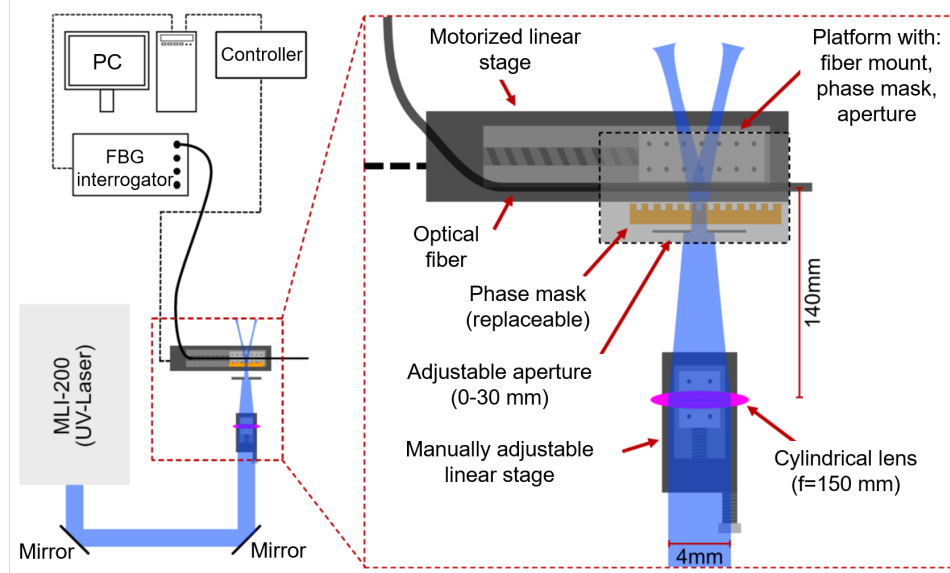


Figure 4.1: Schematic diagram of the FBG inscription setup in the Photonics Laboratory [61].

a focal length of 150 mm is used to focus the light beam on the fiber core, and it is mounted on a manually adjustable linear stage, so the energy density can be slightly adjusted by changing the lens position. A manual aperture whose horizontal width can be individually adjusted with two micrometer screws from 0 to 30 mm is used to customize the length of FBG. Finally, the light beam is incident on a phase mask, and a near-field fringe pattern is produced by the interference of the plus and minus first-order diffracted beams. The interference pattern photoimprints a refractive-index modulation in the core of a photosensitive optical fiber (hydrogen-loaded fiber or highly germania-doped fiber) placed in near contact (100-200 µm) to the phase mask. To avoid burning, the coating of the fiber is removed mechanically with a stripper or chemically with acetone in advance. Each phase mask has a fixed pitch period corresponding to a specific Bragg wavelength. Different phase masks should be used to inscribe FBGs with different Bragg wavelengths. When FBGs with longer grating lengths ($> 4$ mm) need to be fabricated, scanning inscription rather than stationary inscription is required because the size of the focused light beam is only $\sim 4$ mm. The scanning inscription, which refers to scanning the light beam across the aperture and the phase mask at a constant speed, can be achieved via a motorized linear stage. It should be noticed that the distance between the fiber and the phase mask is also a critical parameter due to the low spatial coherence of the UV light used, so another manually adjustable linear stage is used for adjusting this distance to achieve a high contrast fringe pattern.

With the FBG inscription setup, Type-I seed FBGs with different grating strengths and Bragg wavelengths can be obtained in different fibers (single-mode fibers and PM fibers with different diameters). A FBG interrogator is connected to the fiber to monitor the inscription situation of the seed grating in real time. Typically, the seed gratings for RFBGs are fabricated in hydrogen-loaded standard telecom single-mode fibers (Corning, SMF-28). For some specific needs, seed gratings can also be fabricated in hydrogen-loaded LMA fibers with 125 µm (LIEKKI, Passive-12/125, LMA-125) and 250 µm diameters (LIEKKI, Passive-12/250, LMA-250). Detailed information on these fibers can be found in Table 4.1. Compared to SMF-28 and LMA-125, LMA-250 needs more shots to achieve a grating with the same strength. It should be noticed that a LMA-250 fiber has a diameter of 250 µm, making it not directly compatible with commercial single-mode demodulation systems. A splicing technology using the filament splicing unit (LFS4000, Vytran Thorlabs UK Ltd, Exeter, Great Britain) has been developed in the Phtonics Laboratory to splice LMA-250 together with SMF-28. Fig. 4.2 shows a microscope picture of a splicing region between a LMA-250 fiber and a SMF-28 fiber. There is some loss at the splicing region due to mode field mismatch, but the signal is still strong enough for sensing.

Table 4.1: Specifications of the optical fibers.

| Fiber type | Core diameter (µm) | Cladding diameter (µm) | NA | GeO$_2$ content | Source |
|---|---|---|---|---|---|
| SMF-28 | 8.2 | 125 | 0.14 | 3.5 mol% | [39, 164] |
| LMA-125 | 12.5 | 125 | 0.08 | 1.5 mol% | [165] |
| LMA-250 | 12.5 | 250 | 0.08 | 1.5 mol% | [165] |
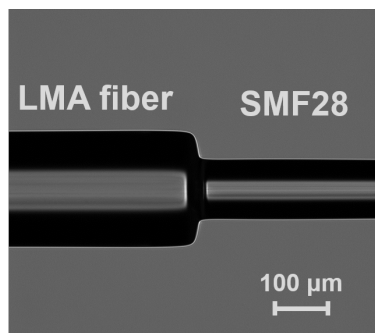


Figure 4.2: Microscope picture of a splicing region between a LMA-250 fiber and a SMF-28 fiber.

After inscription, the seed gratings are put into high-temperature environments for further heat treatments. In the Photonics Laboratory, two different furnaces can be used for this

purpose: a high-temperature tube furnace (ROS 20/250/12, IBF Industrie Beratung Finke
Nürnberg, Germany), and a high-temperature calibration furnace (Isotech Pegasus Plus
1200 S, Isothermal Technologie Ldt. Merseyside, Great Britain). In some experiments, an
additional hydrogen out-diffusion process, usually carried out in the temperature range
of 80-100 °C, is performed to avoid the influence of residual hydrogen inside fibers. But
it is not mandatory because, even without this process, the hydrogen will be removed at
the very beginning of the subsequent high-temperature regeneration process. Then, the
seed gratings are heated up to high temperatures for regeneration and annealing.
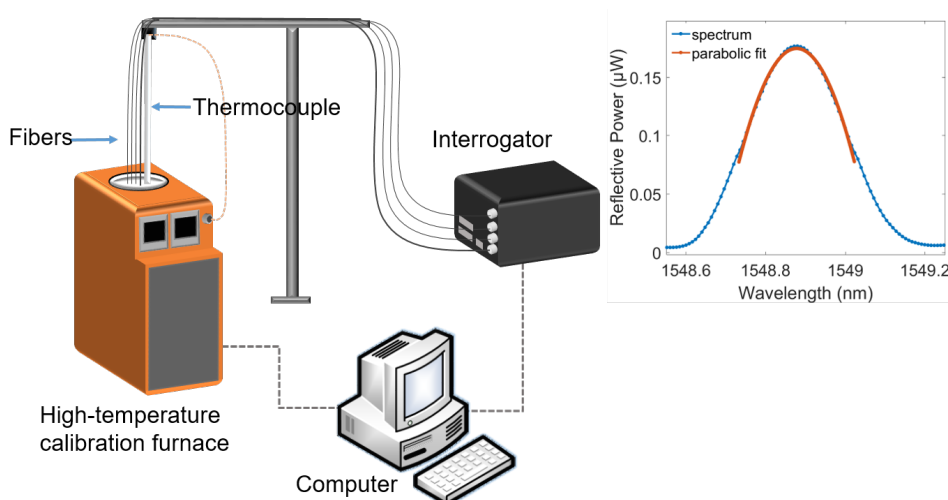


Figure 4.3: Schematic diagram of a regeneration and annealing process.

In the following part of this subsection, the experimental results from an isothermal re-
generation and annealing process of seed gratings in a SMF-28, two LMA-125, a LMA-250
fibers, will be shown. In this experiment, the coatings of these fibers were removed in
advance by acetone. All seed gratings in these fibers were inscribed by the phase mask
method mentioned above and had the same grating length of 3 mm, the same Bragg wave-
length at 1550 nm, and the same reflectivity of 90 %. A hydrogen out-diffusion process had
been carried out at 80 °C for 110 hours before regeneration. After out-diffusion, the fibers
were directly placed into the high-temperature calibration furnace Pegasus Plus 1200S,
whose temperature was already at 900 °C. Fig. 4.3 shows the schematic diagram of the re-
generation and annealing process. A Type-R thermocouple (TP-Temperature-Products,
Freigericht, Germany) was placed together with the RFBGs for highly accurate reference
temperature measurements. A FBG interrogator (si255, Micron Optics, Atlanta, USA)
with a low pass filtering function was used to record the information from those gratings
in real time. A peak-finding algorithm based on the parabolic fit (power lower limit for
fitting: 50 % of peak) was used to determine the Bragg wavelength, as an example shown

in the inset. During the whole regeneration and annealing process of 48 hours duration, the temperature was kept isothermal at 900 ℃.

The right axis of Fig. 4.4 shows the temperature evolution recorded by the Type-R thermocouple, and the left axis shows the reflectivity evolutions of the seed gratings. All the reflectivities decreased dramatically at the beginning of the regeneration process due to the decay of Type-I FBG. After ∼20 minutes, the seed gratings vanished in succession, and RFBGs appeared afterward. In addition, it can be seen from the inset that the SMF-28 reached the vanishing point slightly faster than the LMA-125 and LMA-250. This was because the regeneration process and regeneration temperature were highly related to the dopant concentration: The fibers with higher dopant concentration were expected to have a lower regeneration temperature, i.e., to achieve regeneration easier. In this experiment, the fibers were put into the same temperature environment, so the seed FBG in the SMF-28 fiber with higher germanium concentration (3.5 mol%) achieved regeneration earlier than the others in LMA fibers (1.5 mol%).
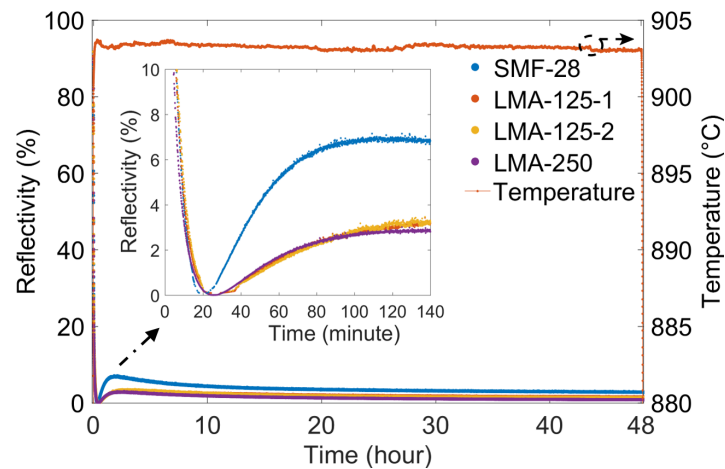


Figure 4.4: Evolutions of the temperature and the reflectivities of the seed gratings in SMF-28, LMA-125, and LMA-250 fibers during 48 hours isothermal regeneration and annealing process at 900 ℃.

There was no more reflectivity increase after ∼100 minutes, and the reflectivities became relatively stable after ∼10 hours. Until then, from seed gratings to RFBGs, the reflectivities decreased from 90 % to 3 % for SMF-28, both 1.5 % for LMA-125 and LMA-250. The remaining hours during the heat treatment were used for annealing the RFBGs to reduce the wavelength drift. The wavelength characteristics will be discussed in the next section.

### 4.1.2 Wavelength drift of RFBG at high temperatures

As mentioned in Section 3.1.1, one of the biggest challenges for RFBGs is that their Bragg wavelengths suffer from slow wavelength drifts when they are exposed to high temperatures over long time periods, affecting the long-term functionality of the sensors. Therefore, it is necessary to study the wavelength drift behavior of RFBG at high temperatures. This section will introduce several investigations made on this topic.

**Influence from dopant concentration on wavelength drift rate**

Fig. 4.5(a) shows the evolutions of the actual Bragg wavelengths of seed FBGs in SMF-28, LMA-125, and LMA-250 fibers in the same isothermal regeneration and annealing process mentioned in Section 4.1.1. It can be seen that, for all types of fibers, the Bragg wavelengths underwent blue drifts at the beginning of the regeneration and annealing process, followed by red drifts for the rest of the annealing procedure. In order to have a closer look at the wavelength drift, normalized offsets were set for the Bragg wavelengths of all RFBGs, when the wavelengths reached the local minimum and the positive drifts started, as shown in Fig. 4.5(b). Dutz et al. [111] divided the Bragg wavelength evolution of the RFBG in a SMF-28 fiber during the 800 °C isothermal regeneration process into three phases. These phases can also be found for the RFBG in the SMF-28 fiber in our experiment. As shown in Fig. 4.5(b), in phase I, the Bragg wavelength showed a negative drift, as mentioned before. Then, in phase II, the wavelength drift turned positive, and there was a local maximum value in wavelength. In phase III, the drift behavior changed, and the slope remained almost constant.
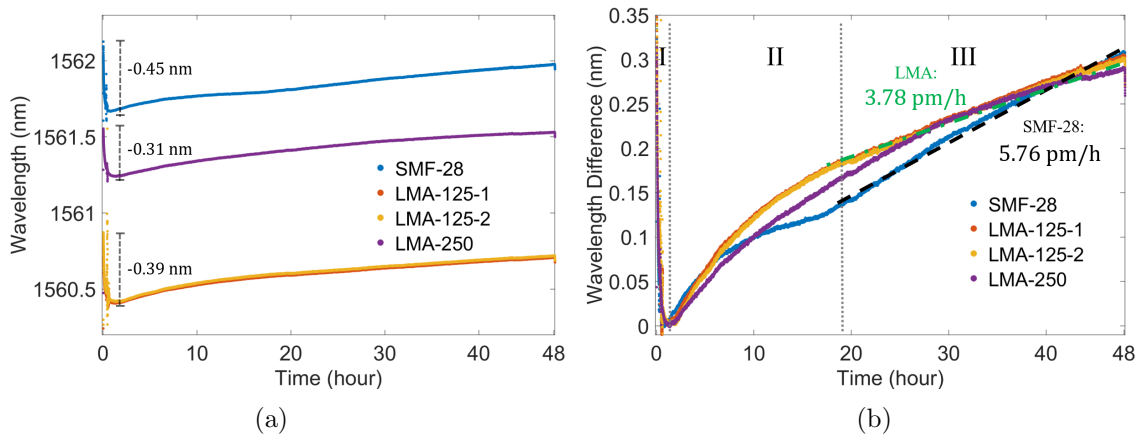


Figure 4.5: Evolutions of the Bragg wavelengths of seed FBGs in SMF-28, LMA-125, and LMA-250 fibers during 48 hours isothermal regeneration and annealing process at 900 °C: (a) actual Bragg wavelengths, (b) wavelength differences with normalized offsets at the start of the positive drift.

It is believed that at elevated temperatures, Bragg wavelength drifts might be highly related to the residual stress relaxation inside the fiber [33, 102]. Here, the blue drift in phase I was attributed mainly to the relaxation of mechanical stress because this kind of stress acted compressively in the fiber core region and could be released at high temperatures [42, 127]. This behavior was predominantly a characteristic of the optical fiber employed and depended only marginally on the type of the grating, as a standard single-mode fiber with a fs-FBG also showed this initial negative drift when it was heated up [111]. The negative wavelength drifts for the SMF-28 fiber are ∼0.45 nm, for the LMA-125 fibers ∼0.39 nm, and for the LMA-250 fiber ∼0.31 nm, respectively. According to Eqs. 2.12 and 2.13, the drift difference between different fibers comes from different Young's moduli, fiber sizes, and signally different draw tensions during fiber draw processes.

In the further annealing process, thermal stress relaxation might be the dominant factor for the wavelength drift of RFBGs. In phase III, the SMF-28 showed a drift rate of ∼5.76 pm/h. However, for LMA fibers, the wavelength progression after phases I was slightly different to SMF-28 fiber. In phase II, the wavelength behavior of LMA fibers was a continuous evolution with no local maximum value. In phase III, LMA-125 and LMA-250 fibers showed quite similar behavior and almost the same drift rate, with a value of ∼3.78 pm/h, which was much lower than that of the SMF-28 fiber.
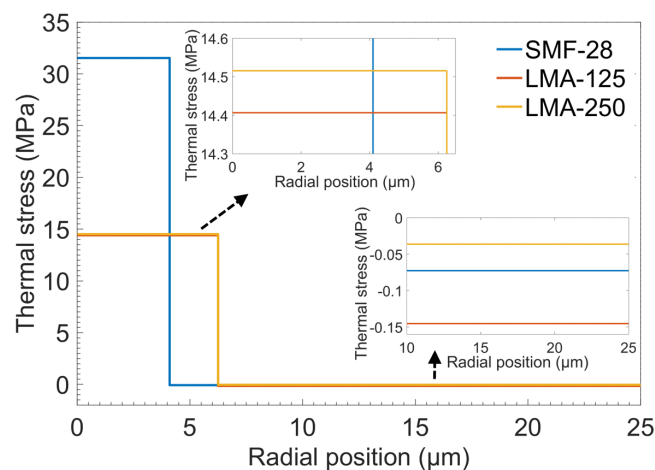


Figure 4.6: Thermal stress profiles of SMF-28, LMA-125, and LMA-250 fibers.

Thermal stress relaxation might be the reason for the different drift rates in phase III. According to Eqs. 2.14 and 2.15, and the parameters in Tables 4.1 4.2, the thermal stress profiles of SMF-28, LMA-125, and LMA-250 fibers can be calculated, as shown in Fig. 4.6. It can be seen from the calculated results that the dopant concentration of $GeO_2$ has a much more significant impact on the thermal stress compared with the fiber size (diameter). The thermal stress inside the core of a LMA fiber is much smaller than that

Table 4.2: Parameters of the optical fibers with RFBG.

| Parameters | | Value | Source |
|---|---|---|---|
| $\alpha_{core}$ | SMF-28 | $9.7 \times 10^{-7}$ /°C | calculated based on Eq. 2.16 |
| | LMA | $7.3 \times 10^{-7}$ /°C | calculated based on Eq. 2.16 |
| $\alpha_{clad}$ | | $5.5 \times 10^{-7}$ /°C | [48, 76] |
| $E$ | | 74.9 GPa | [78] |
| $\nu$ | | 0.16 | [60] |
| $\Delta T$ | SMF-28 | -850 °C | [47] |
| | LMA | -900 °C | |

of a SMF-28 fiber. This can be easily accepted: considering the fact that LMA fibers have lower dopant concentration, the properties of core and cladding are more similar.

According to the thermal stress profiles, the theoretical calculation shows a very slight thermal stress difference between the LMA fibers with different diameters, whereas the thermal stress of the SMF-28 fiber is much larger than that of the LMA fibers. During the annealing process, the thermal stresses inside fibers were gradually relaxed, and the fiber with larger thermal stress exhibited a higher drift rate. Stress relaxation might not be the only cause of the drift behavior, but it should be one of the major ones.

It should be noticed that the loaded hydrogen would also influence the axial stress inside the fiber [166] and thus disturbs the wavelength drift behavior. The purpose of the hydrogen out-diffusion process carried out before regeneration was to eliminate this influence. After 110 hours at 80 °C, no further negative wavelength drift due to hydrogen out-diffusion was observed. In addition, the temperature inside the furnace had already been heated to 900 °C before placing the fibers into it, so the disturbance from temperature-induced wavelength changes caused by gradual heating was also excluded.

In summary, our results show that, in the regeneration and annealing process of RFBGs, the regeneration efficiency and the characteristics of wavelength drift were highly related to the dopant concentration. Compared with SMF-28, the RFBGs in the LMA fibers with a lower dopant concentration had a lower drift rate in the annealing process, the reason of which might contribute to the lower residual thermal stresses of LMA fibers.

**Long-term wavelength drift measurement**

In the last experiment, the wavelength drift behavior of RFBGs at high temperatures was studied on a time scale of tens of hours. While on longer time scales like hundreds or thousands of hours, even at a low rate, the wavelength drift could accumulate into

Table 4.3: Information on the Type-I seed FBGs for the long-term wavelength drift measurement.

| Fiber | $\lambda_B$(nm) | Reflectivity | $\Delta$n$(10^{-4})$ |
|---|---|---|---|
| SMF-28 | 1550.690 | 90% | 4.54 |
| LMA-250-1 | 1549.942 | 85% | 3.52 |
| LMA-250-2 | 1550.076 | 90% | 4.60 |

a significant change, leading to a large temperature information deviation. Besides, as mentioned in Section 3.1.1, the long-term drift behaviors at high temperatures are more complicated. It has been reported that the Bragg wavelength showed a blue drift [33] after a red drift or even another red drift afterward [125] when the fibers were annealed at high temperatures over hundreds or thousands of hours. Here, in this subsection, I will introduce the research results from an one-year wavelength drift measurement of RFBGs at high temperatures and give some explanations for their wavelength behaviors.

Type-I seed FBGs were inscribed in a SMF-28 and two LMA-250 fibers using the phase mask method (scanning). Detailed information on the seed gratings are shown in Table 4.3. The high-temperature calibration furnace Pegasus Plus 1200S was used to provide the high-temperature environment for those gratings, and the Type-R thermocouple was used for temperature reference. The schematic diagram is similar like Fig. 4.3, but another interrogator (sm125, Micron Optics, Atlanta, USA) was used to record the information from the gratings.

To know the wavelength drift behavior of RFBGs and to eliminate disturbance factors, this research consisted of three parts: hydrogen out-diffusion process, regeneration and annealing process, and long-term stability test. The hydrogen out-diffusion process was carried out after the inscription of seed gratings. The fibers were put into the calibration furnace at 80 °C for 118 hours. All the Bragg wavelengths of seed gratings experienced negative drifts and finally approached saturation levels. It took around 30 hours for the SMF-28 fiber to saturate, while 110 hours for the LMA-250 fibers due to the larger diameter. After the hydrogen out-diffusion process, the fibers were taken out of the furnace.

For the regeneration and annealing process, the calibration furnace was heated up to 900 °C and lasted 2 hours. After that, the fibers were put back into the furnace for the isothermal heat treatment at 900 °C. RFBGs were formed in the first hour, and the following time was used for annealing. The whole process lasted 115 hours. The Bragg wavelength evolutions during the 115-hour regeneration and annealing process are shown in Fig. 4.7(a). The Bragg wavelength underwent an initial negative drift at first half an hour
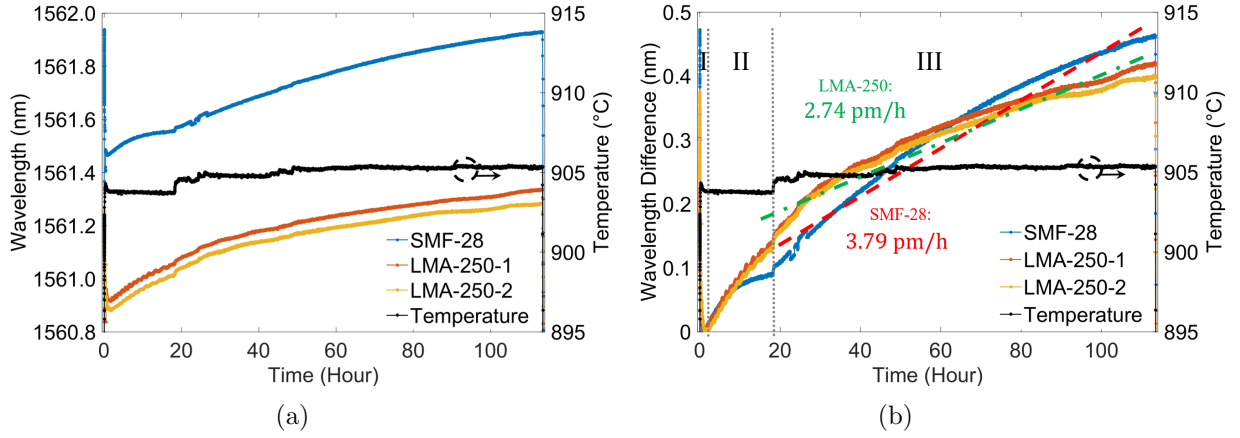
Figure 4.7: Evolutions of the Bragg wavelengths of seed FBGs in a SMF-28, and two LMA-125 fibers during 115 hours isothermal regeneration and annealing process at 900 °C: (a) actual Bragg wavelength, (b) wavelength differences with normalized offsets at the start of the positive drift.

(phase I), and then the drift turned positive. To better know the positive drift behavior of RFBGs in the annealing process, normalized offsets were set when the local minimum wavelengths were reached, and the positive drifts started, as shown in Fig. 4.7(b). It can be seen that, in phase III, the RFBGs in LMA-250 fibers (3.79 pm/h) showed a lower drift rate compared with the RFBG in SMF-28 fiber (2.74 pm/h). It is worth noting that the obtained drift rates were all lower than those in the same kinds of fibers in the last section (Influence from dopant concentration on wavelength drift rate), and this was not due to experimental differences. If only the drift rates within 48 hours were examined, the results would be similar. However, as time gradually increased, the drift rate gradually decreased, eventually decreasing the average drift rates calculated by the overall time. After the 115-hour isothermal regeneration and annealing process, the long-term stability test was carried out. The reflective powers, Bragg wavelengths as well as spectra of each RFBG were recorded by the interrogator sm125. The temperature of the calibration furnace was set to 600 °C and kept stable for around one year (368 days). Due to the usage of the interrogator in other experiments and the software interruption problem (For a few times, the furnace stopped working because of the software interruption, then it was restarted and heated back to 600 °C), the data acquisition was paused several times for the remaining working time during the long-term stability test, so the data package during the whole year was separated into 8 files from "20-02-11" to "21-03-08". Even though there were some interruptions in the data acquisition, the temperature provided by the calibration furnace was relatively stable throughout the year. The temperature evolution recorded by the thermocouple is shown in Fig. 4.8. The reflective powers of
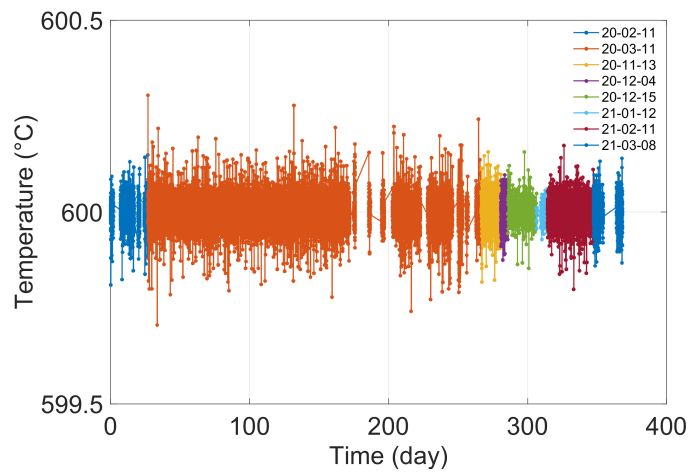
Figure 4.8: Evolution of the temperature during the long-term stability test.
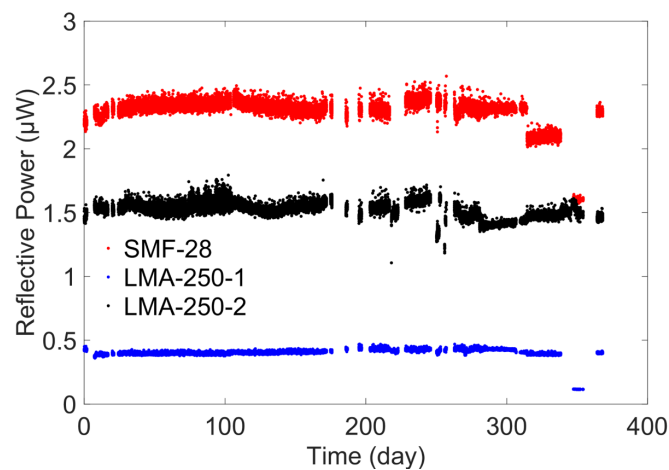


Figure 4.9: Evolutions of the refractive powers of the RFBGs during the long-term stability test.

three RFBGs are shown in Fig. 4.9. It can be seen that there was almost no change in the reflective power of three RFBGs over 300 days. The sudden power decreases of RFBGs in SMF-28 and LMA-250-1 on the 340th day were due to the reconnection problem between the pigtail and the interrogator, and they can be neglected.

Here, the main focus was on the wavelength drift behaviors of the RFBGs, and the wavelength differences were obtained by subtracting the initial Bragg wavelengths when the test started from the actual Bragg wavelengths of each RFBG. The Bragg wavelengths of the RFBGs in these fibers all showed positive drifts in the long-term stability test. As shown in Fig. 4.10, the drift of the RFBG in SMF-28 showed a monotonous increase with a drift rate of 0.243 nm/year (0.0277 pm/h) and reached a saturated level after 250 days.
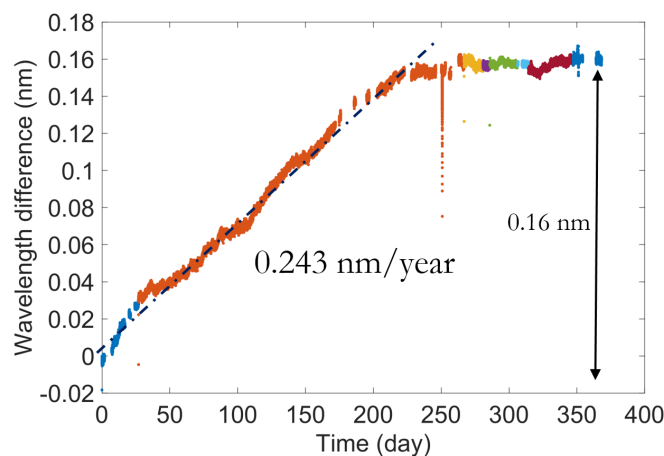
Figure 4.10: Evolution of the Bragg wavelength of the RFBG in SMF-28 fiber during the long-term stability test.

There was almost no change in the wavelength drift for the RFBG in SMF-28 during the last 100 days. The final wavelength drift after one year was +0.16 nm.

Unlike the RFBG in SMF-28, the drift rate of the RFBGs in LMA fibers showed a noticeable and sudden change during the long-term stability test, both for LMA-250-1 and LMA-250-2. As shown in Fig. 4.11(a) and Fig. 4.11(b), the drift rates were relatively low at the first 100 days (region I), whose values were 0.058 nm/year (0.0066 pm/h) for LMA-250-1, and 0.073 nm/year (0.0083 pm/h) for LMA-250-2, respectively. After 110-130 days, the drift rates suddenly increased (region II), which were 0.407 nm/year (0.0464 pm/h) and 0.329 nm/year (0.0376 pm/h), respectively. After 300 days, the wavelength drifts of the RFBGs in LMA fibers also reached saturated levels. The final wavelength drifts after one year were +0.12 nm for LMA-250-1 and +0.14 nm for LMA-250-2. It is worth noting that the spectrum of the RFBG in LMA-250-2 suffered from deformation (double peaks) due to interference from the etalon effect. In order to avoid the data misreading of the peak-finding algorithm, after recording the spectra, a low-pass filtering LabVIEW program was used. The unfiltered and filtered spectra before the test (at room temperature) and during the test after 181 hours were shown in Fig. 4.12. More information can be found in [167].

The Bragg wavelength evolutions of the RFBG in LMA-250-2 before and after the low-pass filtering are shown in Fig. 4.13. Compared with the results before the low-pass filtering, the drift rate after the low-pass filtering was slightly lower: 0.061 nm/year (0.0070 pm/h) for the first 100 days and 0.281 nm/year (0.0321 pm/h) afterward. The final wavelength drift after one year was still +0.14 nm. A summary of the wavelength behavior in this long-term stability test is shown in Table 4.4.
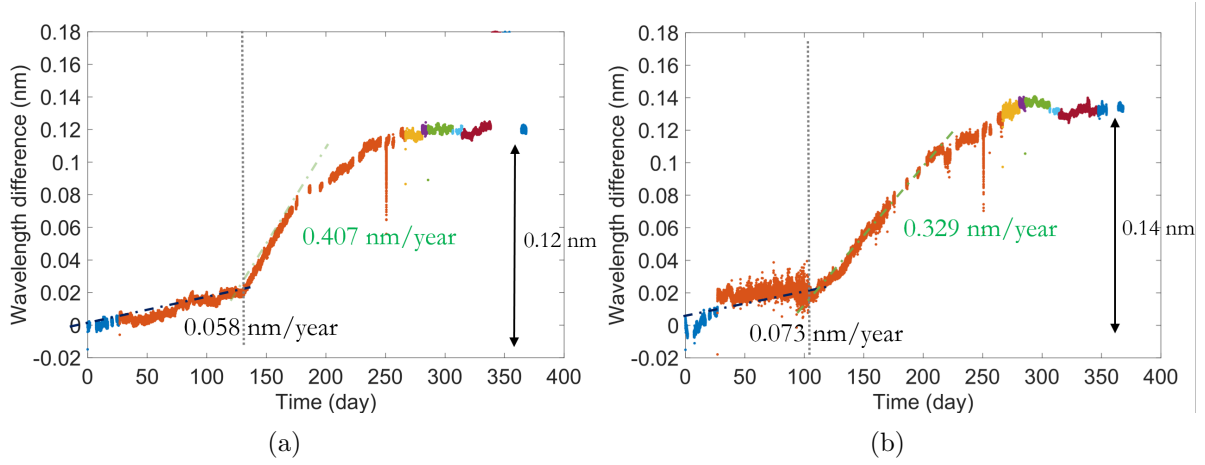
Figure 4.11: Evolutions of the Bragg wavelengths during the long-term stability test of the RFBGs in (a) LMA-250-1, (b) LMA-250-2.
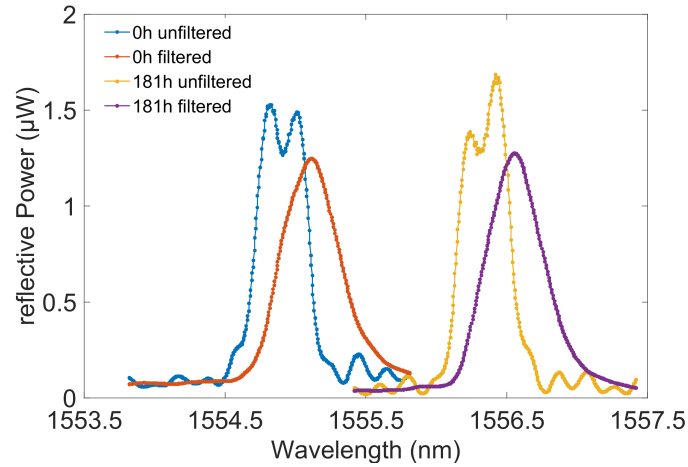


Figure 4.12: Unfiltered and filtered spectra of the RFBG in LMA-250-2 before and during the test.

Table 4.4: Summary of wavelength drift rates of RFBGs in the long-term stability test.

| RFBG | SMF-28 | LMA-250-1 | LMA-250-2 | LMA-250-2 filtered |
|---|---|---|---|---|
| Region I (nm/year) | 0.243 | 0.058 | 0.073 | 0.061 |
| Region II (nm/year) | 0.243 | 0.407 | 0.329 | 0.281 |
| Final drift (nm) | 0.16 | 0.12 | 0.14 | 0.14 |

The results of the long-term stability test at 600 °C showed that there was almost no change in the reflective powers of all RFBGs, and RFBGs could work over long-term periods at least up to this temperature level. For the wavelength drift, all the wavelength
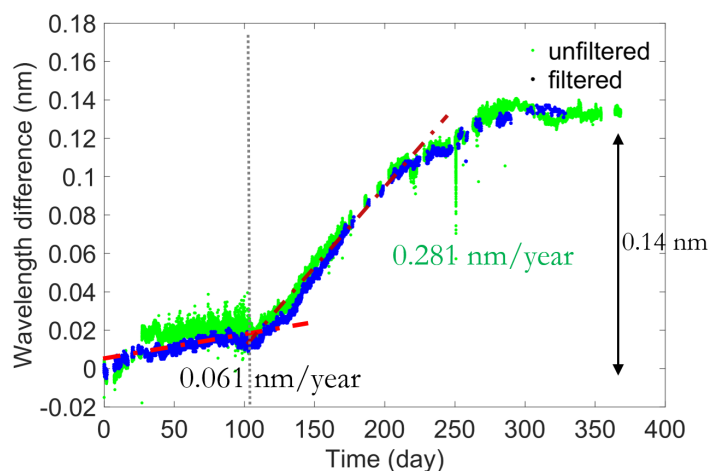
Figure 4.13: Evolution of the Bragg wavelength of the RFBG in LMA-250-2 before and after low pass filtering during the long-term stability test.

drifts reached the saturation level in a range from +0.12 nm to +0.16 nm. Before the saturation, the drift rate of the RFBG in SMF-28 fiber was almost constant, while the drift rate of RFBGs in LMA fibers can be divided into two regions. In the first 100 days, the drift rate was relatively low, one order lower than that of the SMF28 fiber. As discussed in the above two subsections, it is believe that the drift behaviors are related to the residual stress relaxation inside fiber [33, 102]. The RFBG in a LMA fiber with a lower dopant concentration is expected to have a lower drift rate at high temperatures due to its lower residual stresses. However, a sudden increase in the drift rate occurred in the second region for LMA fibers, with a value in the same order as SMF-28. Hot corrosion might be a possible reason for this sudden increase. As mentioned in Section 2.1.2, chemical reactions happen between water and silica at high temperatures, resulting in the formation of immobile hydroxyl. The cracks and defects on the fiber surface are deepened by these reactions and accumulate gradually until mechanical strength degeneration occurs. In this case, the residual stresses inside the fiber are largely affected. Besides, dopant diffusion might also contribute because other researchers have found that the 40% germanium concentration in the fiber core was diffused to the fiber cladding after 85 days at temperatures above 900℃. In this case, the residual stresses between the core and cladding would also be affected [168]. It should be noticed that the final drifts of RFBGs in LMA fibers were still smaller than that of RFBGs in SMF-28 fiber.

In summary, our research in this subsection showed that, compared with the RFBG in SMF-28 fiber, the RFBGs in LMA fibers have obviously lower wavelength drift and improved long-term functionality when the total working time is less than 100 days at 600 ℃. As a comparison, other reported long-term stability tests were normally carried

out at higher temperatures ranging from 760 ℃ to 1000 ℃ [123–125]. As mentioned in Section 3.1.1, in those tests, the red drifts were usually followed by subsequent blue drifts, which might be due to the reduced viscosity of silica at temperatures higher than 600 ℃.

### 4.1.3 Temperature sensitivity of RFBG

RFBGs are usually used for high-temperature sensing, which could be regarded as an alternative to thermocouples. For temperature distribution measurement, several thermocouples with separate lead heads need to be deployed [2], largely increasing the complexity of the measurement system and might be limited by space. While, for RFBGs, with the capacity of wavelength multiplexing, it is easily to achieve multipoint temperature measurement just in a single fiber. Here, in this section, the research on the temperature sensitivity of RFBG will be introduced.

**Temperature calibration process**

Normally, after the regeneration and annealing process, a temperature calibration process from room temperature to high temperatures is needed to obtain the temperature sensitivity of the fabricated RFBGs, i.e., the relationship between Bragg wavelength and temperature. As mentioned in Section 2.2.1, in a wide temperature range, it has been found that there is a nonlinear relationship between $\Delta\lambda_B(T)$ and temperature [8] and a polynomial function, Eq. 2.37, can be used to represent $\Delta\lambda_B(T)$.

In the Photonics laboratory, after extensive experiments, a generalized fifth-order polynomial calibration function is found to be the best choice for RFBG temperature sensors working in a wide temperature range (typically from room temperature to 800 ℃) [8, 111]:

$$\Delta\lambda_B(T) = a_1 T + a_2 T^2 + a_3 T^3 + a_4 T^4 + a_5 T^5, \tag{4.1}$$

because other polynomials with lower orders show more significant residuals between the calibration data points and the fitted polynomial functions, and no further significant improvements can be achieved by higher orders.

This generalized fifth-order polynomial calibration function can be used for all RFBGs on the same type of fiber produced by the same fabrication process. For every individual RFBG, its actual Bragg wavelength at temperature $T$ satisfies the following relationship with temperature:

$$\lambda_B(T) = \lambda_B(0) + a_1 T + a_2 T^2 + a_3 T^3 + a_4 T^4 + a_5 T^5, \tag{4.2}$$
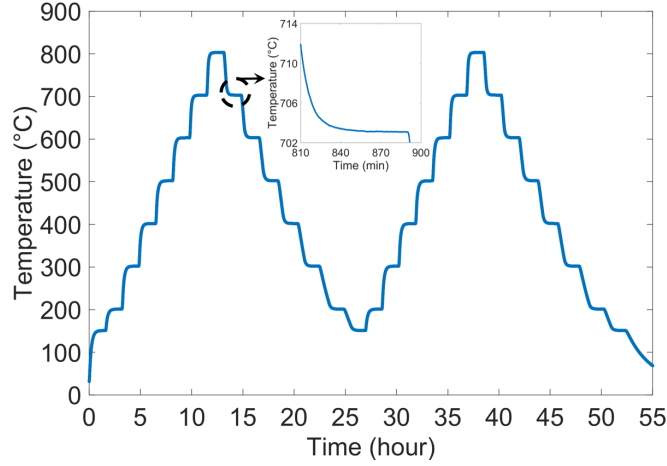
Figure 4.14: Temperature evolution during a standarized temperature calibration process from room temperature to 800 ℃.

where $\lambda_B(0)$ represents the Bragg wavelengths of the RFBG at 0 ℃, and it can be calculated by using an additional measured data point $(T_{RT}, \lambda_{RT})$ at room temperature for reference [110].

The Photonics Laboratory also proposed a standardized temperature calibration process to obtain the polynomial coefficients $a_1$ to $a_5$. From 150 ℃ to 800 ℃, the fibers with RFBGs are placed in the high-temperature calibration furnace Pegasus Plus 1200S with the Type-R thermocouple placed together for temperature reference. The Bragg wavelengths are recorded by an interrogator in real time. There are two repeated temperature cycles, and, in each cycle, fifteen temperature steps (150 ℃, 200 ℃, 300 ℃, 400 ℃, 500 ℃, 600 ℃, 700 ℃, 800 ℃, 700 ℃, 600 ℃, 500 ℃, 400 ℃, 300 ℃, 200 ℃, and 150 ℃) need to be carried out, with each step lasting for 90 minutes. Fig. 4.14 shows the temperature evolution during a standardized temperature calibration process recorded by the reference thermocouple. Due to the thermal mass of the calibration furnace, it takes a long time until temperature equilibrium is reached at each target temperature, as shown in the inset. Therefore, the data in the last 10 minutes of each step are chosen as useful data. Besides, an additional temperature calibration point is used when the furnace is at room temperature.

The room temperature measurement is carried out using a Peltier-driven calibration device, the temperature of which is controlled to a set value of $\sim$20 ℃. The reference temperature was provided with a commercial PT100 resistive temperature sensor (JUMO GmbH & Co. KG, Fulda, Germany) with an uncertainty better than 0.02 ℃. The calibration device consists of a copper block with drilled holes, so the RFBGs and the PT100 can be inserted into them before the measurement.

**Influence from dopant concentration on temperature sensitivity**

According to Eq. 2.16 and the theoretical calculations in Table 4.2, the CTE of glass is highly related to the dopant concentration, $\alpha_{core}$ of a SMF-28 fiber $(9.7 \times 10^{-7}$ /°C) is expected to be larger than that of a LMA fiber $(7.3 \times 10^{-7}$ /°C). While Eq. 2.36 tells us that the temperature sensitivity of FBG depends on the CTE of fiber, so dopant concentration is expected to influence the temperature sensitivity of FBG, especially in a wide temperature range.

To figure out the influence of dopant concentration, RFBGs fabricated in SMF-28, LMA-125, and LMA-250 fibers by the regeneration and annealing process mentioned in Section 4.1.1 were used for the standardized temperature calibration process. Since those RFBGs had been annealed at 900°C for 48 hours, almost no drift or hysteresis was found in the Bragg wavelength during the calibration process in two cycles. Fig. 4.15(a) shows the temperature-induced Bragg wavelength change $\Delta\lambda_B(T)$ of the RFBGs in those fibers. The polynomial fit method is used to obtain the fit coefficients of the polynomial calibration functions for RFBGs, whose values are shown in Table 4.5. The fit coefficients of the RFBG in the LMA-125 fiber are the mean of the two sets of results from LMA-125-1 and LMA-125-2.
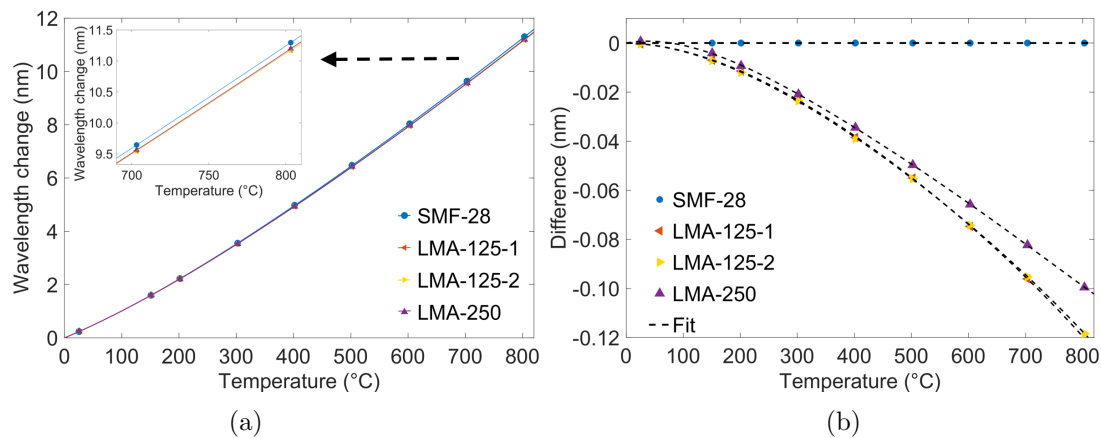


Figure 4.15: (a) Temperature-induced Bragg wavelength change $\Delta\lambda_B(T)$ of the RFBGs in SMF-28 and LMA fibers. (b) $\Delta\lambda_B(T)$ difference between RFBGs in the LMA fibers and the SMF-28 fiber.

For a more intuitive display, the $\Delta\lambda_B(T)$ differences between the RFBGs in LMA fibers and SMF-28 fiber, $\Delta\lambda_{B,LMA}(T) - \Delta\lambda_{B,SMF28}(T)$, are shown in Fig. 4.15(b). It can be seen that the temperature sensitivity of the RFBG in SMF-28 fiber was higher than that of LMA fibers because of the higher dopant concentration and the larger CTE of the SMF-28 fiber core. Besides, it can also be found that the temperature sensitivity of the

Table 4.5: Fit coefficients of the polynomial calibration function for the RFBGs in SMF-28, LMA-125, and LMA-250 fibers from room temperature to 800 ℃.

| Coefficients | SMF-28 | LMA-125 | LMA-250 |
|---|---|---|---|
| $a_1$ (nm/℃) | $9.01 \times 10^{-3}$ | $9.00 \times 10^{-3}$ | $9.05 \times 10^{-3}$ |
| $a_2$ (nm/℃$^2$) | $1.23 \times 10^{-5}$ | $1.20 \times 10^{-5}$ | $1.17 \times 10^{-5}$ |
| $a_3$ (nm/℃$^3$) | $-1.28 \times 10^{-8}$ | $-1.26 \times 10^{-8}$ | $-1.18 \times 10^{-8}$ |
| $a_4$ (nm/℃$^4$) | $8.82 \times 10^{-12}$ | $8.73 \times 10^{-12}$ | $7.87 \times 10^{-12}$ |
| $a_5$ (nm/℃$^5$) | $-2.61 \times 10^{-15}$ | $-2.63 \times 10^{-15}$ | $-2.25 \times 10^{-15}$ |

RFBG in LMA-125 fiber was slightly higher than that in LMA-250. The larger pure silica cladding diameter of LMA-250 led to a slightly lower CTE of the whole fiber.

## 4.2 Characteristics comparison between RFBG and SFBG

In cooperation with the College of Physics and Optoelectronic Engineering, Shenzhen University, a SFBG sensor was obtained. In this section, two RFBGs and the SFBG were put into the same high-temperature environment for annealing and temperature calibration, so their high-temperature characteristics could be compared.

### 4.2.1 Fabrication of SFBG sensor

**SFBG inscription**

The obtained SFBG was inscribed in Shenzhen University by the femtosecond laser LbL scanning method [138]. The grating period $\Lambda$ was set to be 1.332 µm, and the order of grating $m$ was 3. According to the phase matching condition $m\lambda_B = 2n_{eff}\Lambda$, the Bragg wavelength was around 1550 nm. The grating length was 2.67 mm. Fig. 4.16(a) shows the microscope picture of the inscribed SFBG, and Fig. 4.16(b) shows the picture of the SFBG sensor. The diameter of the sapphire fiber was 60 µm and the length of the whole sapphire fiber was 9.8 cm. The SFBG was 0.8 cm away from the fiber end. The other side of sapphire fiber was spliced with a silica fiber, whose splicing method will be introduced right after.

**Splicing Sapphire fiber**

For SFBGs in sapphire fibers, to date, the most widely used measurement system is based on multimode fibers [34, 137–139, 145, 169, 170]. In general, dozens of meters of graded-
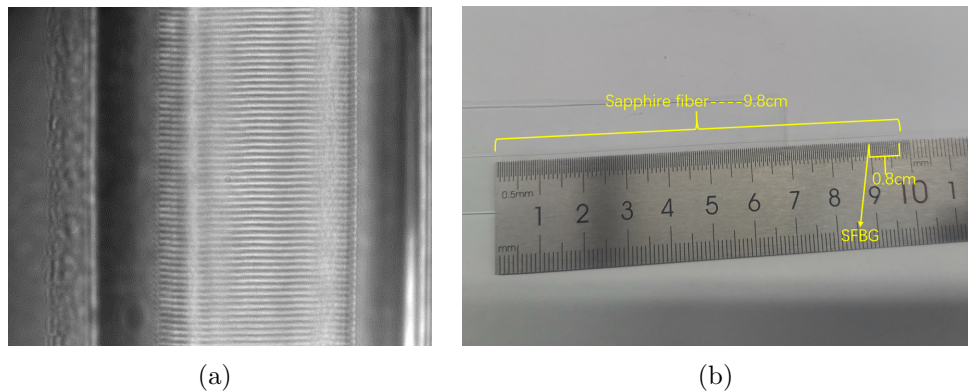
Figure 4.16: (a) Microscope picture of the inscribed SFBG by the femtosecond laser LbL scanning method. (b) Picture of the SFBG sensor obtained from Shenzhen University.

index multimode fibers as the lead-in fibers are applied to effectively excite all guided modes, resulting in a relatively stable reflection spectrum [34, 138, 139, 170]. However, commercial measurement demodulation systems, like FBG interrogators, are generally based on standard single-mode fibers.

In cooperation with Shenzhen University, we have invested a fiber splicing technology based on mode field matching to splice a sapphire fiber and a standard single-mode fiber together.
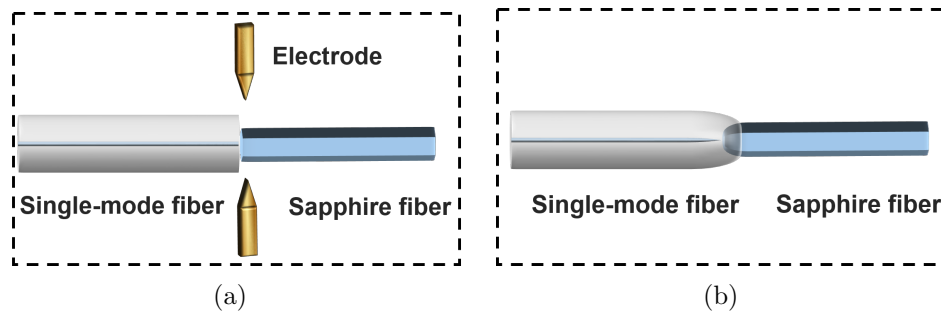


Figure 4.17: Schematic diagrams of the mode field matching splicing technology (a) before, and (b) after the splicing.

Fig. 4.17(a) and 4.17(b) show the schematic diagrams of the mode field matching splicing technology before and after the splicing, respectively. A polished sapphire fiber and a cleaved single-mode fiber are spliced together by a fiber fusion arc splicer. When the fusion splicing starts, the single-mode fiber softens under the action of the arc. The sapphire fiber, with a smaller diameter than the single-mode fiber, is pushed toward it by the pusher motor. The end face of the sapphire fiber deforms under a certain amount of discharge, and a conical structure with a decreasing diameter is formed at the sapphire

fiber tip. Then, the softened single-mode fiber wraps around the conical sapphire fiber, forming a tapered region from the single-mode fiber to the sapphire fiber. Finally, a new structure with overlapped double cones is formed. In this structure, the tapered region from the single-mode fiber to the sapphire fiber helps expand the mode field diameter of the single-mode fiber. The decreasing diameter of the conical sapphire fiber means less supported modes and also a better mode field matching.

Fig. 4.18(a) shows the microscope picture of a splicing region between a SMF-28 fiber and a 60 µm-diameter sapphire fiber. The internal structure of this splicing region can be observed when a few drops of refractive index oil are dipped on it, as shown in Fig. 4.18(b). With the same splicing technology, another sapphire fiber with a diameter of 75 µm was splicing to another SMF-28, whose internal structure is shown in Fig. 4.18(c).



(a)                              (b)                              (c)
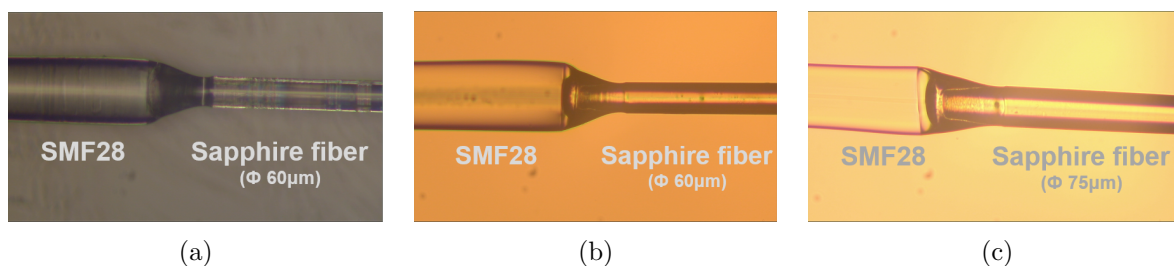
Figure 4.18: (a) Microscope picture of a splicing region between a SMF-28 fiber and a 60µm-diameter sapphire fiber. Internal structure of the splicing regions between a SMF28 fiber and (b) a 60 µm-diameter sapphire fiber, (c) a 75 µm-diameter sapphire fiber

Due to the high-order mode suppression in the splicing region, a quasi-single-mode reflection spectrum from SFBG could be obtained. The mode field matching splicing technology could provide good adaptability for SFBG sensors to the commonly used single-mode demodulation systems, like FBG interrogators.

## 4.2.2 Wavelength drift comparison between RFBG and SFBG

As already shown in Section 4.1.2, the characteristics of wavelength drift were highly related to the fiber properties like dopant concentration and residual stress between core and cladding. For a sapphire fiber, considering its unique structure: a pure crystal without cladding structure, the drift characteristics of SFBGs in sapphire fibers might be vastly different from those RFBGs in silica fibers. A comparative study based on this topic may have some reference value for the wavelength drift behavior mechanism of RFBGs or even other silica fiber-based FBGs. In this subsection, two RFBGs and the SFBG obtained from Shenzhen University were put in the same high-temperature environment for isothermal annealing, and compared their Bragg wavelength behaviors.

To compare the wavelength drift characteristics, two Type-I seed FBGs with 90 % reflectivity, 3 mm length, and 1550 nm Bragg wavelength were inscribed in hydrogen-loaded SMF-28 fibers by the phase mask method. The coatings of the two fibers had been removed in advance with acetone to avoid burning. The two seed FBGs and the SFBG were put together and placed into the high-temperature furnace Pegasus Plus 1200S. The interrogator si255 was used to record the spectra and the Bragg wavelengths of those gratings. A hydrogen out-diffusion process was carried out first to eliminate the effect of hydrogen on wavelength drift. The temperature in the calibration furnace was kept at 100 °C for 24 hours until no further negative drift could be observed from seed FBGs in SMF-28 fibers, while there was no wavelength drift in the SFBG at all in the out-diffusion process. After that, the temperature in the calibration furnace was directly heated up to 900 °C and kept at this temperature for 48 hours to anneal those fibers. For the spectrum
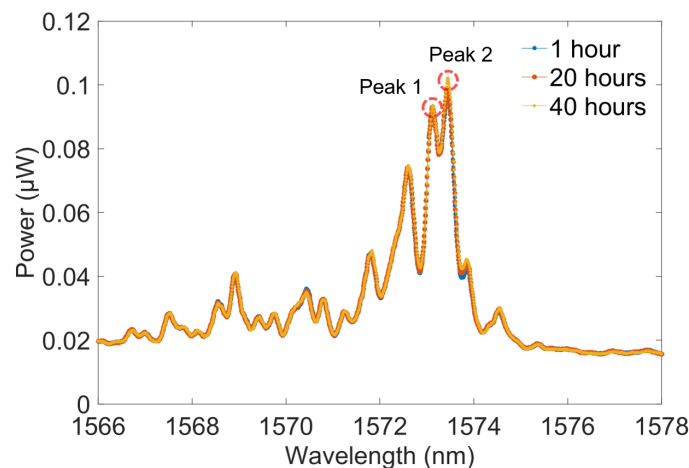


Figure 4.19: Reflection spectra of SFBG during 900 °C annealing process at different times.

of SFBG, although the mode field matching splicing technology could achieve a certain degree of high-order mode suppression, several low-order modes still existed in the reflected light, resulting in the relatively complex spectral shape of the SFBG. Fig. 4.19 shows the reflection spectra of the SFBG during the 900 °C annealing process at different times (after 1 hour, 20 hours, and 40 hours). The spectrum showed several peaks, but the spectrum shape was stable during the whole annealing process. The two peaks with the highest two reflective powers were marked as "Peak 1" and "Peak 2", and their Bragg wavelengths were recorded simultaneously by the interrogator during the whole process.

At the beginning of the annealing process, regeneration started in two seed FBGs, and they became RFBGs, so they are called "RFBG 1" and "RFBG 2" in the following part. The evolutions of actual Bragg wavelengths of the RFBGs and the SFBG during the 900 °C
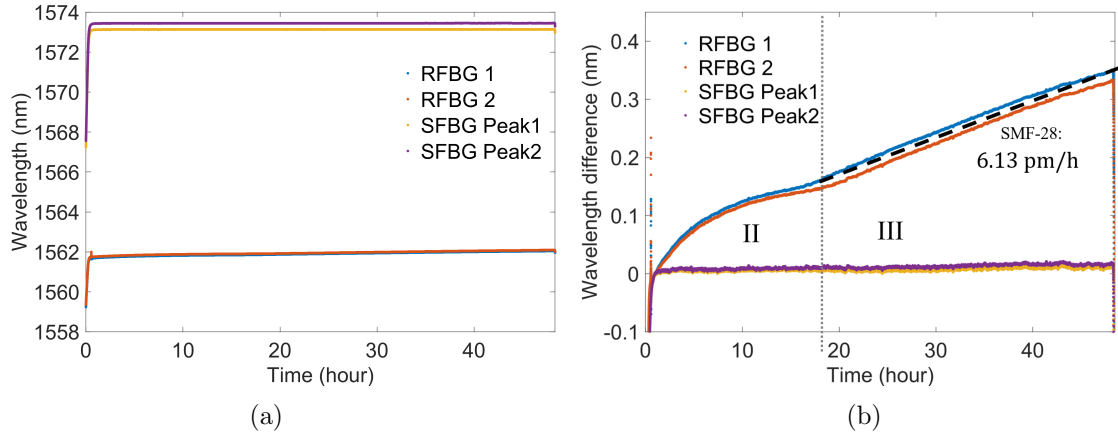
Figure 4.20: Evolutions of the Bragg wavelengths of the RFBGs and the SFBG during 48 hours isothermal annealing process at 900 °C: (a) actual Bragg wavelength, (b) wavelength differences with normalized offsets when the temperature stabilized to 900 °C.

annealing are shown in Fig. 4.20(a). Due to the higher CTE of sapphire, the temperature-induced Bragg wavelength change of SFBG was much larger than those of RFBGs. For better comparison, we set normalized offsets for the Bragg wavelengths of those gratings when the temperature stabilized to 900 °C, as shown in Fig. 4.20(b). As shown in Fig. 4.20(b), for the RFBGs in SMF-28 fibers, local maximum values in wavelength can be found in phase II, and the drift rates of the two RFBGs were almost identical, with a value of ∼6.13 pm/h. For the SFBG in sapphire fiber, the Bragg wavelengths of the two peaks were quite stable, and no noticeable wavelength drift can be found. Two possible reasons can be used to explain this phenomenon: Firstly, the properties of sapphire are stable at this temperature level. As mentioned in Section 2.1.3, sapphire fiber has a high melting point (2040 °C) and high glass transition temperature [142], so 900 °C is not challenging for sapphire fiber. Secondly, as mentioned in the last subsection, the drift behavior of RFBG might be highly related to the residual stresses inside silica fiber formed by the property difference between the fiber core and cladding. However, a sapphire fiber is just an unclad single crystal, so no obvious residual stress should exist in sapphire fiber. Our research results further support the residual stress relaxation theory for wavelength drift.

## 4.2.3 Temperature sensitivity comparison between RFBG and SFBG

In Section 4.1.3, the results have shown that the dopant concentration influenced the temperature sensitivity by changing the CTE of fiber. For optical fibers made of different materials, the fiber properties are expected to have a big difference. A SFBG in a sapphire
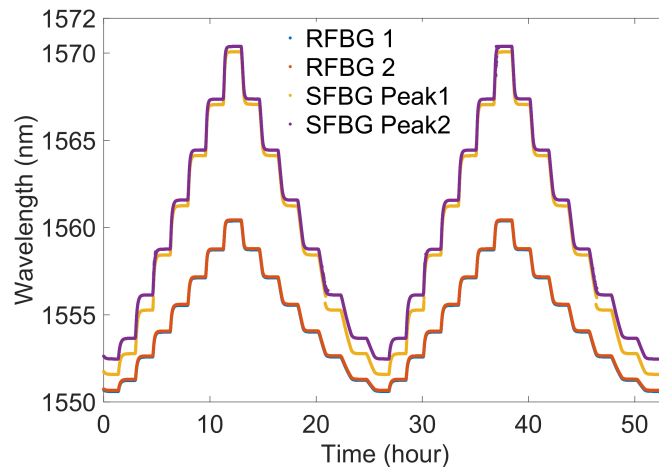
Figure 4.21: Bragg wavelengths evolutions of the RFBGs and the SFBG during temperature calibration process from room temperature to 800 °C.

fiber might show a completely different temperature sensitivity, compared with the silica fiber-based FBGs. In this subsection, the temperature sensitivities of RFBG and SFBG were compared in two temperature ranges successively: one from room temperature to 800 °C and one from room temperature to 1200 °C. Here, the temperature calibrations were carried out using the two RFBGs and the SFBG mentioned in the last subsection right after the annealing.

The first calibration process from room temperature to 800 °C was the same as the standardized calibration process mentioned before, which included two repeated temperature cycles, each with fifteen temperature steps. An additional temperature calibration point was used when the furnace was at room temperature. The Bragg wavelength evolutions of the two RFBGs and the SFBG (two peaks) during the temperature calibration process are shown in Fig. 4.21. It can be seen that, for all the FBGs, there was no obvious drift found in wavelength during the calibration process.

It is worth noting that the shape of the SFBG spectrum was different at different temperatures: the intensities of some side peaks increased or decreased at different temperatures, but they were relatively stable when the temperature was constant. The possible reason for this phenomenon might be the imperfect inscription quality, i.e., the writing position of SFBG was skewed, and it was not in the center of the sapphire fiber. The change of the effective refractive index of the sapphire fiber at different temperatures might result in a difference in the strength of corresponding reflected modes from the SFBG and then undermine the multi-mode suppression effect at the splicing region. The spectra of SFBG in the first temperature cycle of the temperature calibration process from step No.1 to No.15 are shown in Fig. 4.22.
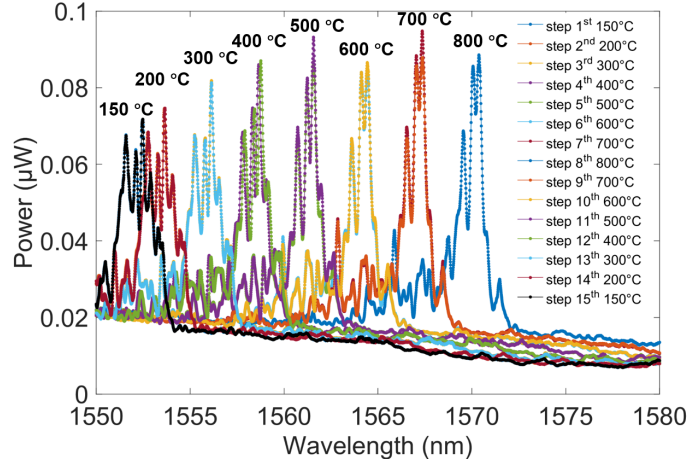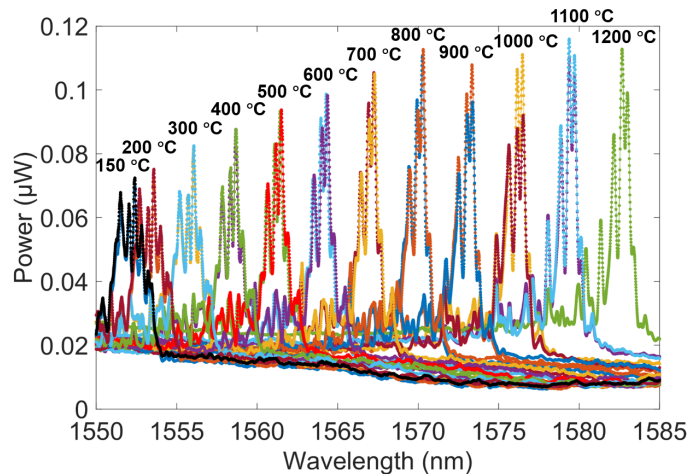
Figure 4.22: Spectra of SFBG in the first temperature cycle of the temperature calibration process from 150 ℃ to 800 ℃.

It can be seen that, compared with the temperature range from 400 ℃ to 800 ℃, the second-highest peak of SFBG was different in the temperature range from 150 ℃ to 300 ℃, which led to the Bragg wavelength misreading for the Peak 1 of SFBG. This means that the peak-finding algorithm recognized the first obvious peak of the SFBG spectrum when the temperature was in the range from 150 ℃ to 300 ℃, while it switched to the second obvious peak when the temperature was in the range from 400 ℃ to 800 ℃. This also explained the disturbance of the wavelength evolution of Peak 1 (yellow line) from step No. 3 to No. 4, and from step No. 12 to No. 13 in Fig. 4.21. While Peak 2 was always the highest peak, and the peak-finding algorithm worked well with it.

Due to this reason, only the wavelength of Peak 2 was used for the polynomial fit of SFBG temperature sensitivity. The temperature-induced Bragg wavelength changes $\Delta\lambda_B(T)$ of the RFBGs and the SFBG (Peak 2) are shown in Fig. 4.23. It can be seen that the temperature sensitivity of SFBG is much higher than that of RFBG. Considering the fact that the CTE of sapphire $(7.7 \times 10^{-6})$ is one order larger than the CTE of silica $(5.5 \times 10^{-7})$, this result is expected. The fit coefficients of 5th-order polynomial calibration functions are shown in Table 4.6.

The second calibration process from room temperature to 1200 ℃ followed afterward. The calibration process was similar to the first calibration process, but each cycle included twenty-three temperature steps (150 ℃, 200 ℃, 300 ℃, 400 ℃, 500 ℃, 600 ℃, 700 ℃, 800 ℃, 900 ℃, 1000 ℃, 1100 ℃, 1200 ℃, ...). The Bragg wavelength evolutions of the two RFBGs and the SFBG (two peaks) during the second temperature calibration process are shown in Fig. 4.24.
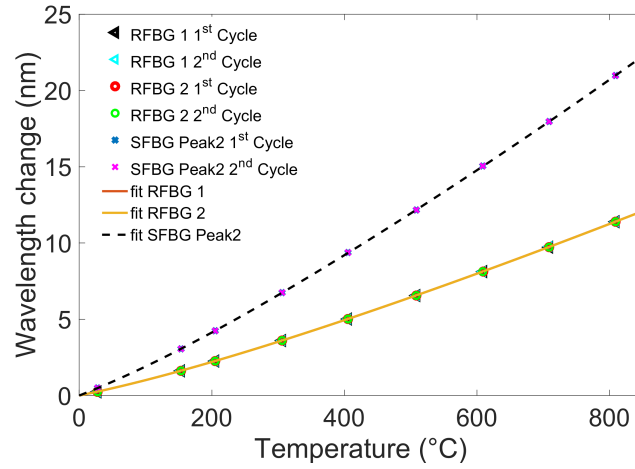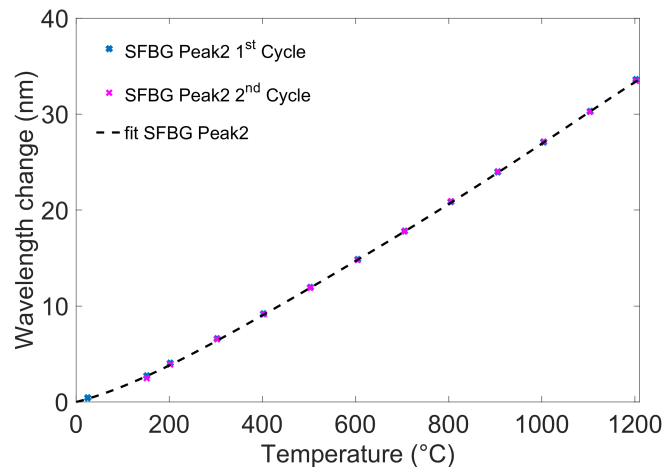
Figure 4.23: Bragg wavelength changes of RFBGs and SFBG, and the corresponding fittings in the temperature calibration from room temperature to 800 ℃.

Table 4.6: Fit coefficients of the polynomial calibration function for the RFBGs and SFBG in the temperature calibration from room temperature to 800 ℃.

| Coefficients | RFBG 1 | RFBG 2 | SFBG |
|---|---|---|---|
| $a_1$ (nm/℃) | $8.94 \times 10^{-3}$ | $8.96 \times 10^{-3}$ | $1.70 \times 10^{-2}$ |
| $a_2$ (nm/℃$^2$) | $1.28 \times 10^{-5}$ | $1.26 \times 10^{-5}$ | $2.27 \times 10^{-5}$ |
| $a_3$ (nm/℃$^3$) | $-1.43 \times 10^{-8}$ | $-1.37 \times 10^{-8}$ | $-2.56 \times 10^{-8}$ |
| $a_4$ (nm/℃$^4$) | $1.07 \times 10^{-11}$ | $9.85 \times 10^{-12}$ | $1.76 \times 10^{-11}$ |
| $a_5$ (nm/℃$^5$) | $-3.47 \times 10^{-15}$ | $-3.05 \times 10^{-15}$ | $-4.76 \times 10^{-15}$ |

It can be seen that the wavelength drifts of RFBGs turned negative from positive when the temperature exceeded 1000 ℃. The drift rates were -15.1 pm/h at 1000 ℃ and -37.5 pm/h at 1100℃, both at least one order of magnitude greater than that at 900 ℃ (+ 5.1 pm/h). Significant wavelength drifts of both RFBGs could be easily observed at 1200 ℃, which was exactly on the edge of $T_g$ of silica fiber [49, 169, 171]. At this point, the CTE, heat capacity, shear modulus, viscosity, and many other properties of silica material differ substantially below and above $T_g$. While there was no observable wavelength drift for SFBG at any temperature during the whole process. The spectra of SFBG in the first temperature cycle of the 1200 ℃ temperature calibration process from step No.1 to No.23 (150 ℃ - 1200 ℃ - 150 ℃) are shown in Fig. 4.25. Similar to the first calibration, the second highest peak of SFBG switched at the temperature range from 300 ℃ to 400 ℃, so the wavelength of Peak 2 was still used for the SFBG temperature sensitivity fitting.

Considering there were obvious drifts for the two RFBGs, if the results were processed ac-
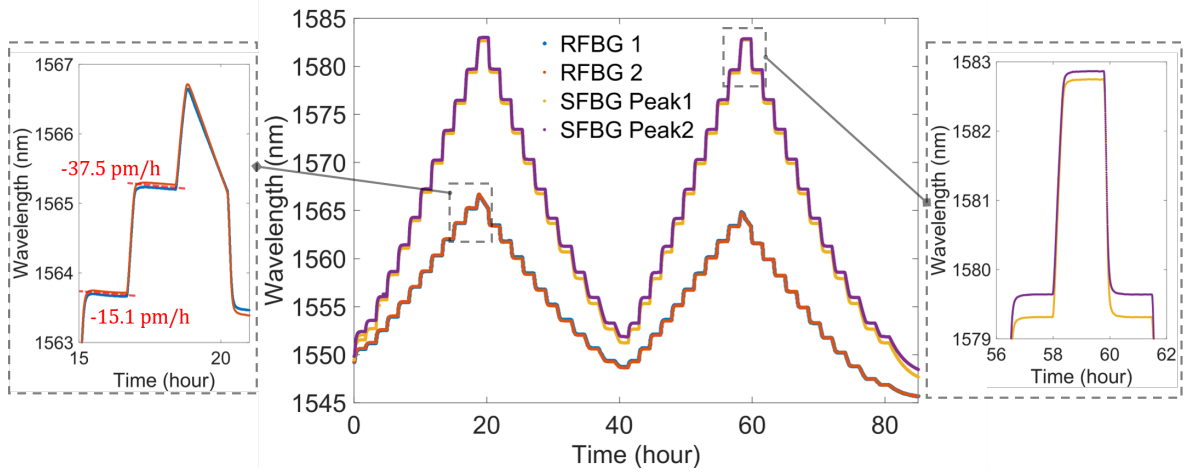
Figure 4.24: Bragg wavelengths evolutions of RFBGs and SFBG during temperature calibration process from 150 ℃ to 1200 ℃.



Figure 4.25: Spectra of SFBG in the first temperature cycle of the temperature calibration process from 150 ℃ to 1200 ℃.

cording to the averaging method in the standardized calibration process, the results would be inappropriate. Therefore, only the temperature-induced Bragg wavelength change of the SFBG (Peak 2) is shown in 4.26, and it is used to fit the temperature sensitivity of SFBG. The fitting coefficients of the polynomial calibration function of the SFBG in the temperature calibration from room temperature to 1200 ℃ are shown in Table 4.7.

In this research, at temperatures lower than 1000 ℃, it can be found that both RFBGs and SFBG showed good high-temperature sensing performance. When the temperature exceeded 1000 ℃, RFBG suffered degraded performance as temperature rising until 1200 ℃ when silica fibers drastically changed their properties and could no longer be used

Figure 4.26: Bragg wavelength changes of RFBGs and SFBG, and the corresponding fittings in the temperature calibration from room temperature to 1200 ℃.

Table 4.7: Fit coefficients of the polynomial calibration function for the SFBG in the temperature calibration from room temperature to 1200 ℃.

| Coefficients | SFBG |
|---|---|
| $a_1$ (nm/℃) | $1.25 \times 10^{-2}$ |
| $a_2$ (nm/℃$^2$) | $4.36 \times 10^{-5}$ |
| $a_3$ (nm/℃$^3$) | $-6.31 \times 10^{-8}$ |
| $a_4$ (nm/℃$^4$) | $4.77 \times 10^{-11}$ |
| $a_5$ (nm/℃$^5$) | $-1.38 \times 10^{-15}$ |

for temperature sensing. The SFBG showed good high-temperature sensing performance from room temperature to 1200 ℃. However, it should be noticed that the spectrum of SFBG is complicated due to the multimode issue, and the unclad structure made SFBGs very sensitive. As a comparison, RFBGs have the advantages of low cost, simple fabrication, multiplexing capacity and easy calibration. Therefore, for application scenarios where the temperature is lower than 1000 ℃, and a large number of sensors are required, RFBG should be the optimal choice.

# Chapter 5

# Monitoring metal casting processes with RFBG sensors

Critical in-situ information like temperature and strain is important for optimizing the casting processes to obtain quality cast parts with reduced residual stresses, high fatigue strengths, and longer life cycles. The Institute for Measurement Systems and Sensor Technology, TUM and the Photonics Laboratory, MUAS have used high-temperature resistant FBGs to monitor aluminum casting processes in cooperation with the Chair of Metal Forming and Casting, TUM [6–8]. In this chapter, the research about using RFBG sensors to monitor metal casting processes was introduced. The temperature and strain distributions during aluminum casting were studied in more detail, and their correlation with solidification characteristics was revealed. Moreover, in addition to aluminum, copper casting processes were also monitored, with the maximum monitored temperature extended from 650 °C to 1100 °C.
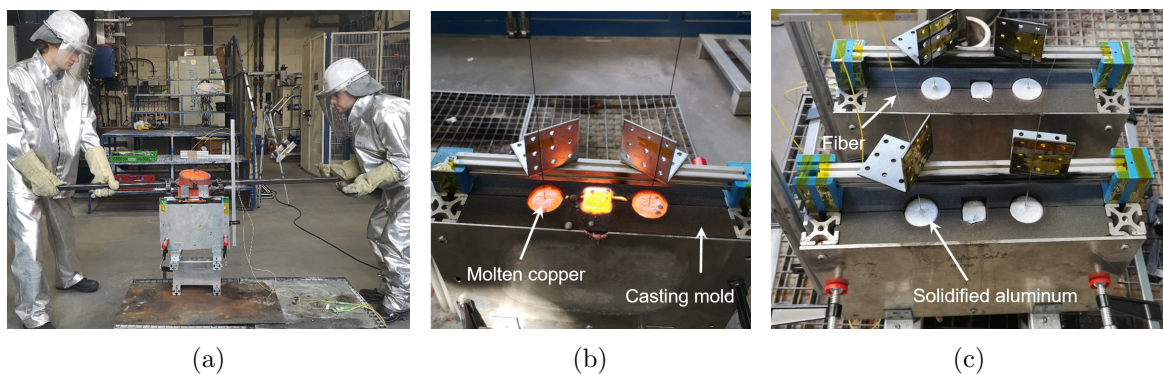


Figure 5.1: Pictures of field experiments of metal casting processes: (a) copper casting during pouring, (b) copper casting after pouring, (c) aluminum casting after cooling.

Figs. 5.1 illustrate the field experiments of the metal casting processes. 3D-printed furan resin-bound silica sand molds were used to determine the casting shape, whose schematic diagram is shown in Fig. 5.2. The structure has two symmetrical arms in the x-axial direction. In casting, the metal is melted in a crucible and then poured into the inlet of the mold. In order to improve the casting quality, a filter is used to filter slag from the melt. Then, the filtered melt flows through the two runners equally and rises from the bottom to the top in both arms along the z-axial direction. The two arms have the same conical geometry with a length of 80 mm, a diameter of 21 mm at the higher end, and a diameter of 16 mm at the lower end. The feeder with a diameter of 40 mm is used to provide extra metal during the solidification process to prevent cavities and voids due to shrinkage.
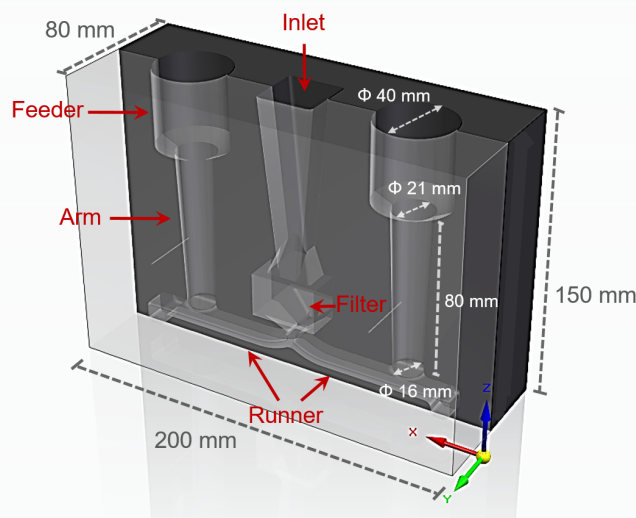


Figure 5.2: Schematic diagram of the casting mold.

As mentioned in Section 3.1.1 and 4.1.2, RFBGs in LMA fibers showed larger tensile force tolerance with larger fiber diameters and lower drift rates at high temperatures due to lower dopant concentration. Those advantages made them a perfect choice for sensing in metal casting. Therefore, in this section, all RFBG sensors were fabricated in LMA-250 fibers. The fabrication processes were similar to those mentioned in Section 4.1.1. But, the reflectivities of seed gratings ranged from 80% to 95%, and there was no separate hydrogen out-diffusion process before the 48-hour 900 ℃ isothermal regeneration and annealing process.

# 5.1 Aluminum casting monitoring using RFBG sensors

In this research, RFBG sensors were used to monitor the aluminum casting process. The standardized hypoeutectic alloy AlSi9Cu3 (DIN EN 1706:2010) was chosen for casting. This alloy is an ideal choice for complex machine and engine parts. The high copper concentration contributes to the high-temperature strength, and the high silicon concentration improves the mechanical strength in general and also provides good castability and machining properties [172]. Table 5.1 shows the actual composition of AlSi9Cu3 used in this research, measured by spark emission spectroscopy.

Table 5.1: Actual composition of AlSi9Cu3 alloy.

| Type | Al | Si | Cu | Fe | Mn | Mg | Zn |
|---|---|---|---|---|---|---|---|
| wt./% | 87.82 | 9.15 | 2.68 | 0.15 | 0.02 | 0.01 | 0.07 |

The schematic diagram of the aluminum casting experiment is shown in Fig. 5.3. For strain measurement, a LMA fiber with a five-point RFBG array was positioned in the left arm of the mold. The lead-in and lead-out of the fiber into the mold were protected with two stainless steel capillaries. The distance between both capillaries was 40 mm. A clamp was used to provide a pretension on the fiber to reduce the impact of disturbances when pouring. The inset shows detailed information on the RFBG array: It consisted of five RFBGs with identical lengths of 3 mm, and the distances between adjacent RFBGs were 6 mm. The Bragg wavelengths of these RFBGs at room temperature from the upper position #1 to the lower position #5 were 1540, 1545, 1550, 1555, and 1560 nm, respectively. This RFBG array was in direct contact with the aluminum alloy during the casting, and thus these RFBGs were influenced by both temperature and strain and were designated as RFBG($T$, $\varepsilon$)s. As one can not distinguish between the Bragg wavelength changes caused by temperature or strain in RFBG($T$, $\varepsilon$)s, a similar five-point RFBG array was inserted into a capillary that extended over the entire length of the RFBG array and was positioned inside the right arm of the mold, only for the temperature measurement. The temperature sensor fiber was glued with silicone at the ingress of the capillary and was freely suspended in the capillary. All capillaries had external and internal diameters of 0.8 mm and 0.4 mm, respectively, and the lower end of the temperature sensor capillary was sealed by laser beam welding. Due to the protection of the capillary, no strain was transferred to these RFBGs, and they were only sensitive to temperature, so they were called RFBG($T$)s. The RFBG($T$, $\varepsilon$)s and RFBG($T$)s with the same Bragg wavelengths were mounted exactly at the same vertical position in each arm of the mold. All the

capillaries were fixed to the frame or the fixed plates. Previous research has proved that the casting mold has excellent symmetry, and there is no obvious temperature difference caused by the capillary, so it can be assumed that each sensing point at the same vertical position in the left and right arms experienced the same temperature evolution during casting [8]. All the Bragg wavelengths were recorded by the FBG interrogator si255 in real time and then transferred to a PC.
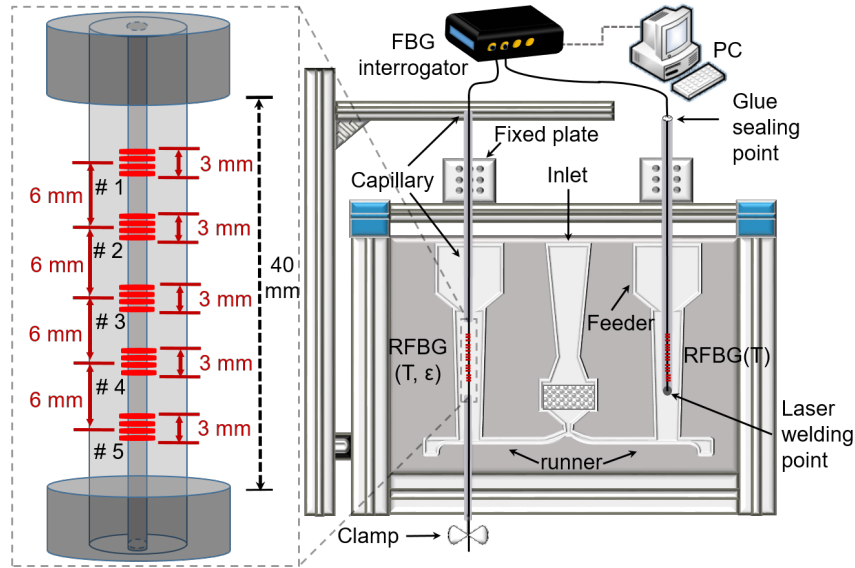


Figure 5.3: Schematic diagram of the aluminum casting experiment.

Fig. 5.4(a) shows the monitored Bragg wavelength changes of RFBG($T$)s and RFBG($T$, $\varepsilon$)s during the complete casting process, while Fig. 5.4(b) depicts the Bragg wavelength changes during the first several minutes with an expanded time scale. Due to the high temperature of the liquid aluminum, all Bragg wavelengths experienced instant redshifts of $\sim$8 nm when the liquid aluminum reached the locations of the sensors. The Bragg wavelength changes of RFBG($T$, $\varepsilon$)s and RFBG($T$)s showed almost the same behaviors at the very beginning because the aluminum at this time was liquid, and no strain but only temperature was applied to the RFBG($T$, $\varepsilon$)s. The separation started afterward when RFBG($T$) continued decreasing due to the temperature drop while RFBG($T$, $\varepsilon$)s otherwise showed positive wavelength shifts (see Fig. 5.4(b)). The positive wavelength shifts were related to tensile strains and will be discussed in detail in Section 5.1.2. After the positive shift, the RFBG($T$, $\varepsilon$)s showed a much faster negative shift rate than the RFBG($T$)s due to the shrinkage of the cooling aluminum. As shown in Fig. 5.4(a), when the casted part was back at room temperature, the wavelength changes of the RFBG($T$)s returned to zero, while the wavelength changes of the RFBG($T$, $\varepsilon$)s were negative and showed values of -12.8 nm due to the shrinkage of the aluminum.
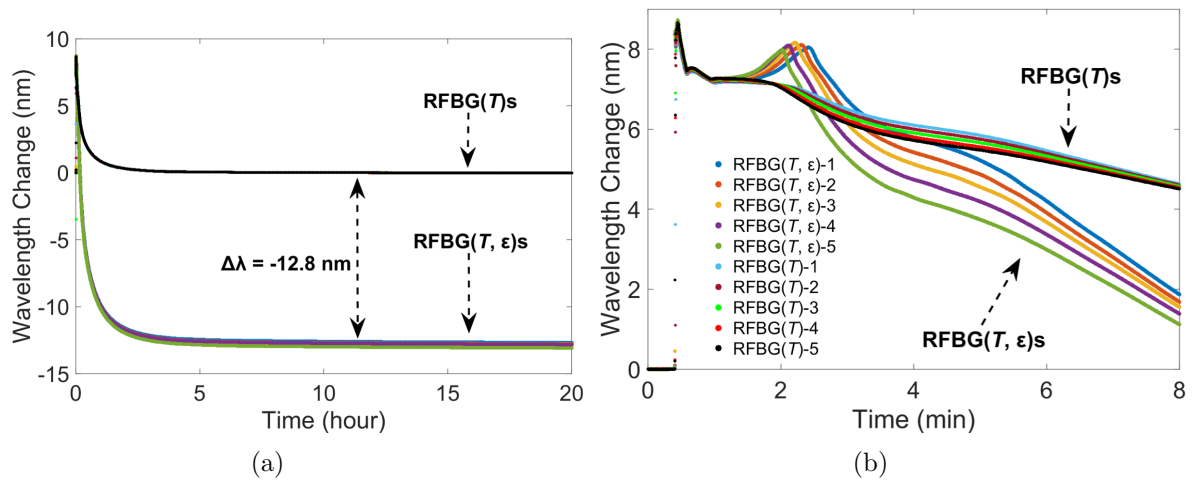
Figure 5.4:  Bragg wavelength changes of RFBG($T$, $\varepsilon$)s and RFBG($T$)s (a) during the whole aluminum casting process, (b) during the first eight minutes of the aluminum casting process.

Fig. 5.5 shows the reflective spectra of RFBG($T$)-3 and RFBG($T$, $\varepsilon$)-3 at room temperature before and after the aluminum casting process as an example. It can be seen from the dashed lines that there was almost no change for the spectrum of RFBG($T$)-3. While, the solid lines show that the spectrum of RFBG($T$, $\varepsilon$)-3 suffered from reflectivity decay and slight deformation, and the whole spectrum shifted to lower wavelength due to the compressive strain caused by the aluminum shrinkage.
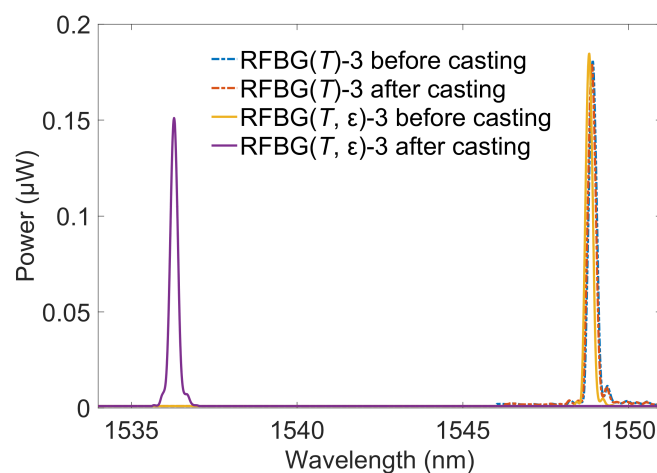


Figure 5.5:  Spectra of RFBG($T$)-3 and RFBG($T$, $\varepsilon$)-3 at room temperature before and after casting.

## 5.1.1   Temperature evolution and distribution during aluminum casting

As mentioned in Section 4.1.3, a generalized fifth-order polynomial calibration function can be used for all RFBGs on the same type of fiber, produced by the same fabrication process. Hamann has used several LMA-250 fibers to fabricate RFBGs via the 48-hour 900 °C isothermal regeneration and annealing process and carried out a series of temperature calibration processes for them [167]. Table 5.2 shows the fit coefficients of the polynomial calibration function for the RFBGs in LMA-250 fibers obtained by him. Compared with the fit coefficients obtained in Table 4.5, the temperature sensitivity obtained by Hamann was a little bit higher. Two possible reasons could be used to explain the difference: Firstly, there was no independent hydrogen out-diffusion process in Hamann's experiments. Secondly, in his experiments, the additional room temperature point was obtained with the Peltier-driven calibration device and the PT100 resistive temperature sensor. Here, the fit coefficients from Hamann were used, because, for all the RFBG sensors used in casting, we did not carry out any independent hydrogen out-diffusion process and the PT100 should provide more reliable temperature data at room temperature than the Type-R thermocouple.

Table 5.2: Fit coefficients of the polynomial calibration function for the RFBGs on LMA fibers from room temperature to 800°C [167].

| Coefficients | $a_1$ (nm/°C) | $a_2$ (nm/°C$^2$) | $a_3$ (nm/°C$^3$) | $a_4$ (nm/°C$^4$) | $a_5$ (nm/°C$^5$) |
|---|---|---|---|---|---|
| Value | 9.65 $\times 10^{-3}$ | 9.47 $\times 10^{-6}$ | -9.47 $\times 10^{-9}$ | 9.14 $\times 10^{-12}$ | -4.43 $\times 10^{-15}$ |

According to Eqs. 4.1 and 4.2, the temperature values can be calculated from the wavelengths of RFBG($T$)s, so the temperature evolutions at different positions can be obtained. Fig. 5.6(a) shows the temperature evolution and distribution in the aluminum casting monitored by the RFBG($T$) array during the whole process. As shown in the inset on the top left, the casting started at room temperature, and after 20 hours of cooling, the temperature of the cast part returned back to room temperature. Previous research has shown that there was no obvious drift when using the RFBG-based temperature sensors in the aluminum casting [8].

Fig. 5.6(b) shows temperature distribution at the very beginning of the aluminum casting process. Considering that the melt aluminum rose from the bottom to the top in the arm, the temperature at RFBG($T$)-5 increased first due to its lowest position. The RFBG($T$)-5 also showed a relatively highest temperature compared to the other RFBG($T$)s due to the heat transfer during the melt flowing, as shown in the inset. The temperature increase at point A corresponded to the latent heat release. Point B corresponded to the
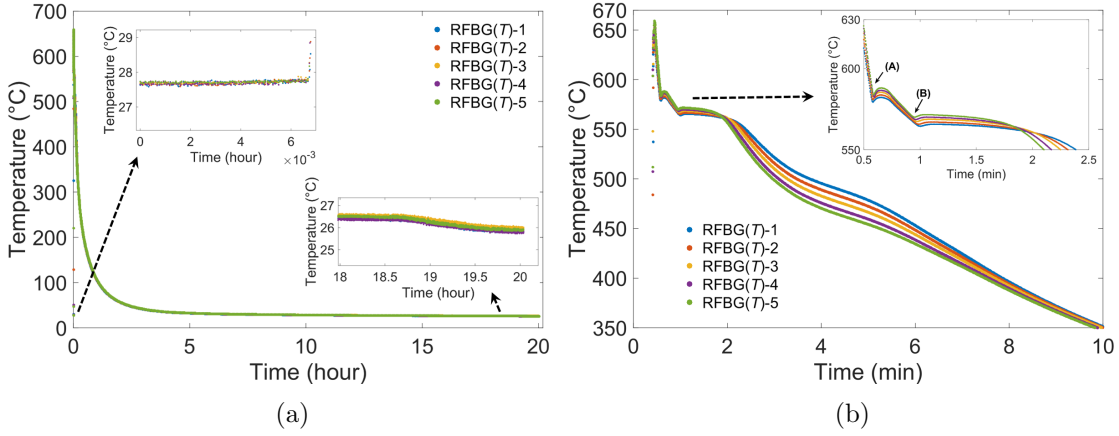
Figure 5.6: Temperature evolution and distribution (a) during the whole aluminum casting process, (b) during the first several minutes of the aluminum casting process.

main eutectic reaction when the $\alpha$(Al)+$\beta$(Si) eutectic dendrites formed. After 2 minutes, the temperature distribution reversed, and the temperature at RFBG($T$)-1 showed the relatively highest temperature compared to the others. This was because of the extra heat provided by the feeder. It can be seen that there was a clear temperature gradient along the vertical direction from 2 to 8 minutes. The higher the position of the RFBG($T$) was located, the higher the temperature was. After that, the temperatures at different locations of the RFBG($T$)s gradually returned to almost the same.

## 5.1.2 Strain evolution and distribution during aluminum casting

The used casting mold had an excellent symmetry between both arms, so the strain-induced Bragg wavelength variation of RFBG($T$, $\varepsilon$)s could be obtained by subtracting the wavelength variations of the corresponding RFBGs from both arms at the same height:

$$\Delta\lambda_{B,RFBG(T,\varepsilon)}(\varepsilon) = \Delta\lambda_{B,RFBG(T,\varepsilon)}(T,\varepsilon) - \Delta\lambda_{B,RFBG(T)}(T). \tag{5.1}$$

In order to get an overview of the strain behavior during the aluminum casting process, in the following section, the strain situation of the fiber during aluminum casting is simplified, by assuming that the strain is acting on a free fiber in the axial direction. Therefore, the strain can be calculated as $\varepsilon = \Delta\lambda_B(\varepsilon)/\lambda_B k_\varepsilon$. As mentioned in Section 2.2.1, in a wide temperature range over several hundred degrees, it has been found that the relative strain sensitivity $k_\varepsilon$ is temperature-dependent, and it can be approximately described with a temperature-dependent Poisson's ratio as Eq. 2.43. According to this equation and the optical fiber parameters in Table 5.3, we can theoretically calculate the temperature-dependent relative strain sensitivity $k_\varepsilon(T)$, as seen in Fig. 5.7.
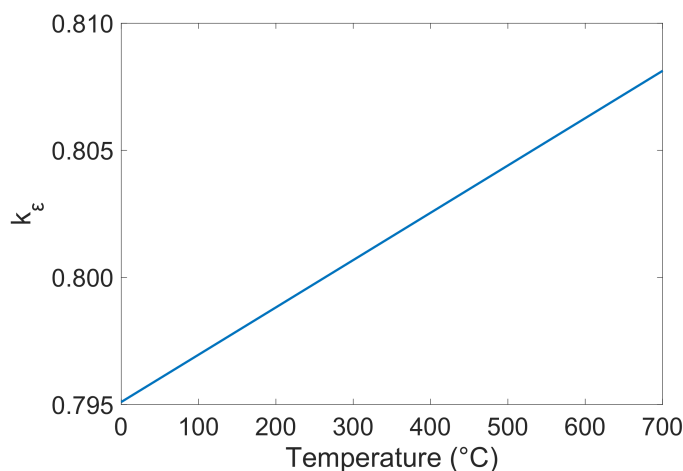
Figure 5.7: Theoretical calculated $k_\varepsilon(T)$ as a function of temperature (0–700 °C).

Therefore, the strain behavior during the aluminum casting can be obtained. Fig. 5.8(a) shows recorded temperature and strain at the middle position of the RFBG arrays (position #3) in the first ten minutes. It can be seen that there was almost no strain transferred to the fiber but disturbances when the solidification started (latent heat released). Tensile strain occurred right after the main eutectic reaction and increased afterward until it reached a maximum value of $\sim$1000 $\mu\varepsilon$. The strain behavior here might relate to the thermal stress caused by the temperature difference between the core and the edge of the cast part: At the beginning, due to the cold mold and the surrounding environment, the edge region of the cast cooled down first, causing it to shrink and deform plastically. The core, however, remained hot and almost liquid, making it incompressible and preventing the edge region from shrinking. As a result, the core region suffered compressive stress, while the edge region was under tensile stress. However, during this period, the stress/strain was not able to be transferred to the fiber due to the too small dendrites, resulting in almost no strain being observed at the beginning. Later, as the core cooled down and shrank, the core shrinkage was hindered by the already cold edge region, creating tensile stress in the core and compressive stress at the edge. During this period, the dendrites grew large enough to transfer the strain to the fiber, and thus the tensile strain was detected [7, 173]. After the maximum tensile strain, the temperature difference between the core and the edge decreased due to the gradual heat transfer, resulting in a rapid drop in the strain as well as temperature.

Due to multiplexing capability, the strain distribution was also obtained by the RFBG arrays, as shown in Fig. 5.8(b). The tensile strains appeared one by one from RFBG($T$, $\varepsilon$)-5 to RFBG($T$, $\varepsilon$)-1, revealing the solidification front started from the lower position to the upper position. The maximum strains were reached at each position accordingly.

Table 5.3: Parameters of the optical fiber and the aluminum alloy.

| Parameter | Value | Source |
|---|---|---|
| $n_{eff}$ | 1.4473 | [174] |
| $p_{11}$ | 0.116 | [175] |
| $p_{12}$ | 0.255 | [175] |
| $E_{fiber}$ | 74.9 $GPa$ | [78] |
| $\nu_{0,fiber}$ | 0.16 | [60] |
| $\frac{d\nu_{fiber}}{dT}$ | $4.79 \times 10^{-5}/°\mathrm{C}$ | [60] |
| $\alpha_{fiber}$ | $5.5 \times 10^{-7}/°C$ | [76] |
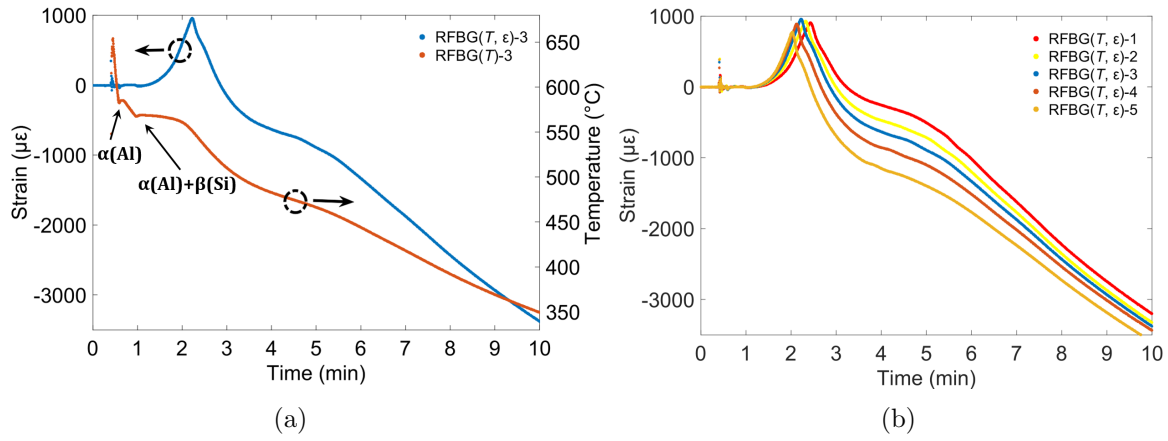


Figure 5.8: (a) Temperature and strain evolution at the middle position of the RFBG arrays, (b) strain distribution recorded by the RFBG arrays during the first ten minutes of the aluminum casting process.

However, when the tensile strain turned to the compressive strain afterward, there was still a gradient in tensile strain distribution from the upper position to the lower position. The strain difference during this period was related to the thermal stress caused by the temperature gradient along the axial direction of the arm, which was also the leading cause of the residual stresses.

## 5.1.3 Correlation between the solidification phases of the aluminum alloy and the strain behavior

Considering the fact that the temperature at each RFBG($T$, $\varepsilon$) was known by RFBG($T$), the strain evolution and distribution as a function of temperature can be obtained, as shown in Fig. 5.9(a), where it can be seen that the final compressive strain reached

values over -10000 $\mu\varepsilon$ after cooling down to room temperature.



(a)

(b)

(c)
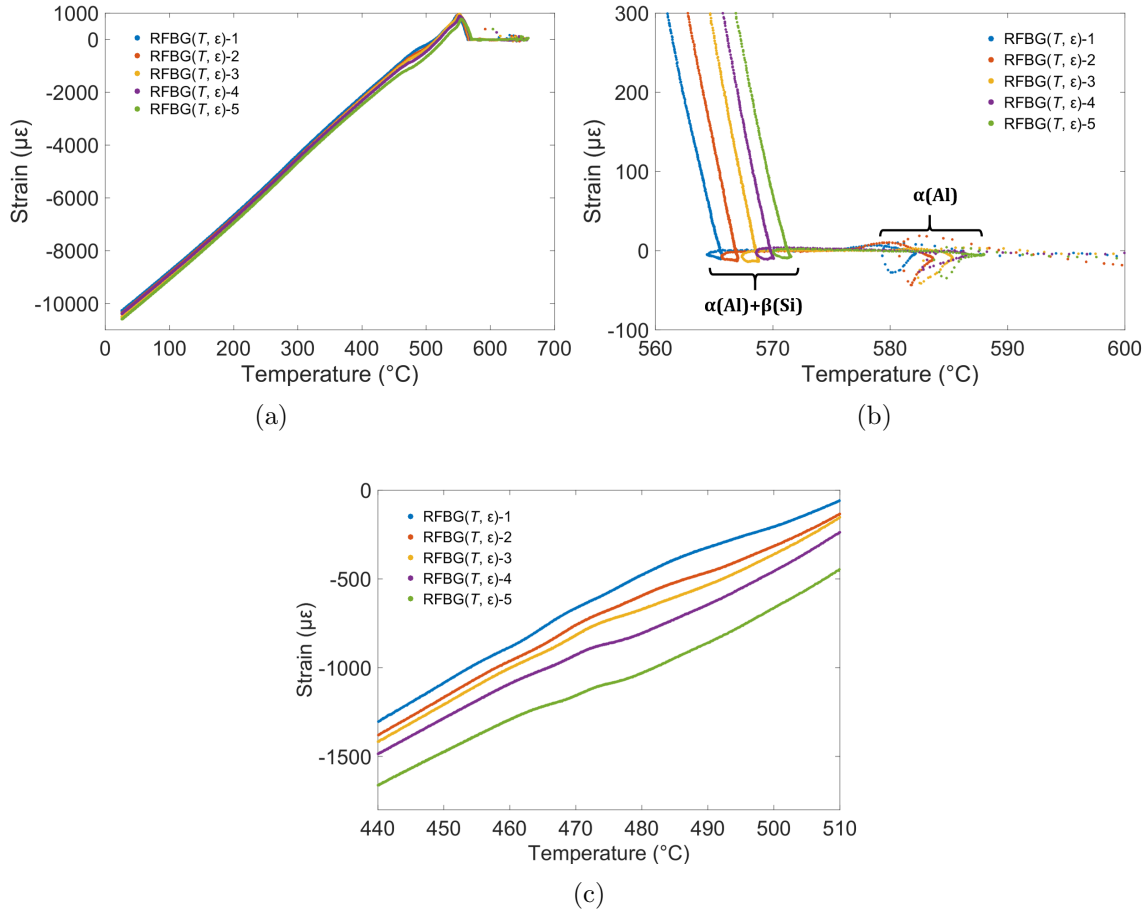
Figure 5.9: Strain evolution and distribution during the aluminum casting monitored by RFBG arrays in the temperature range of (a) 0-700 °C, (b) 560-600 °C, (c) 440-510 °C.

Table 5.4 shows the solidification phases of aluminum alloy reported in other literature [12]. Resemblance can be found between the reported solidification phases and the strain behavior observed. The further zoomed-in results are shown in Fig. 5.9(b). It can be seen that there was no strain observed when the aluminum was still liquid at temperatures higher than 588 °C, and the aluminum cooled down gradually. Some disturbances could be found at temperatures in the range of 580 °C to 588 °C. We associated this with the start of solidification and the formation of the primary $\alpha$-Al dendrite network, which caused almost no strain but some fluctuations to the Bragg wavelengths. This was because, during the early stages, dendrites normally grew from a single nucleus, but only a few microns in diameter [11]. Those dendritic crystals were separate and moved freely in the melt, so there was almost no strain transferring from aluminum to the fiber, even though the temperature increased slightly due to the emitted latent heat.

Table 5.4: Solidification phases of aluminum alloy A380 [12].

| No. | Temperature | Description |
|---|---|---|
| 1 | 576 °C | Start of solidification and formation of $\alpha$(Al) |
| 2 | 566 °C | Start of main eutectic reaction and formation of $\alpha$(Al)+$\beta$(Si) |
| 3 | 562 °C | Rigidity point |
| 4 | 503 °C | Precipitation of Al2Cu |
| 5 | 490 °C | End of solidification |

The circles in the temperature range of 565 °C to 571 °C corresponded to the main eutectic reaction when there was another small temperature increase due to the heat from $\alpha$(Al)+$\beta$(Si) eutectic dendrites formation. The rigidity points, when the further coarsening and ripening of dendrites increased the strength of the solid network, were reached afterward, corresponding to the start of the observed tensile strains. At this point, the solid phase was sufficiently coalesced to transmit tensile stress [14], and the solidifying aluminum was able to transfer stresses to the fiber [6]. It can be seen that the rigidity points started at the lowest RFBG($T$, $\varepsilon$)-5 first. The higher the position of the RFBG was, the later the rigidity point was reached, and the lower the temperature of the rigidity point was. The above-mentioned solidification phases also showed similar behaviors, and they happened in small temperature ranges. The results show that our method can spatially resolve the times and temperatures of the rigidity points and the onsets of the different solidification phases and thus can be used to improve casting processes and the corresponding modeling.

As the temperature continued to decrease, the recorded strain turned into compressive strain due to the shrinkage of the cooling aluminum. After that, aluminum shrinkage dominated the strain behavior. It can be found in Fig. 5.6(b) that, during the period from the start of the main eutectic reaction, which corresponded to point B, to the end of solidification, which was at the temperature of 490 °C, the cooling rates at different sensor positions were different: the higher the sensor position, the lower the cooling rate was. The different cooling rates led to a gradient temperature distribution and a gradient compressive strain distribution, as shown in Fig. 5.9(c), which might be highly valuable in evaluating residual stresses. Further research is needed to determine the specific relationship between strain gradient and residual stresses.

In summary, in this subsection, a gradient strain distribution after the solidification was observed, which might provide useful information about the residual stresses of the casted part. The resemblance between the solidification phases and strain behavior showed that our strain monitoring method could provide a new perspective to study the solidification characteristics of metal alloys.

## 5.2   Copper casting monitoring using RFBG sensors

Compared with aluminum, copper has a much higher melting point (1082 ℃), which makes it more challenging for RFBGs. In this research, RFBG sensors were used to monitor the casting process of a copper-tin alloy CuSn2 (UNSC50700 · JISC5070). This alloy has good corrosion resistance, excellent cold workability, and average strength. Besides, CuSn2 has the highest conductivity for heat and electricity among the copper-tin alloys, and it is commonly applied in the manufacturing of stamped parts, automotive, connectors, and electrical engineering [176]. Table 5.5 shows the standardized composition of CuSn2 and the actual composition of CuSn2 measured by spark emission spectroscopy.

Table 5.5: Standardized and actual composition of CuSn2 alloy.

| Type | Cu(wt./%) | Sn(wt./%) | P(wt./%) | Zn(wt./%) |
|---|---|---|---|---|
| Standardized CuSn2 [176] | rem | 1.6-2.2 | 0.03-0.1 | <0.1 |
| Actual CuSn2 | 98.2 | 1.76 | <0.001 | <0.005 |

The schematic diagram of the copper casting experiment is depicted in Fig. 5.10. Similar to the aluminum casting experiment in the last section, a LMA fiber with a RFBG array protected in a capillary was placed in the right arm of the mold for temperature measurement. The RFBG array had three RFBG($T$)s from the upper position to the lower position, and the distance between adjacent RFBG($T$)s was 20 mm. Besides, a reference Type-K thermocouple was placed nearly at the same position as the middle RFBG($T$). The left arm of the mold was used for strain measurement, where one LMA fiber was partly protected by two separate capillaries, with a RFBG($T$, $\varepsilon$) in direct contact with copper. Limited by the larger shrinkage during copper cooling, the distance between the two capillaries was reduced to 30 mm, and only one RFBG($T$, $\varepsilon$) at the same height as the middle RFBG($T$) was used. The Bragg wavelengths of the RFBGs were measured by the interrogator si255 in real time, whereas the data from the thermocouple were recorded by a DAQ device. Five individual casting experiments have been carried out with the same experimental setup to check our method's reliability and repeatability.

RFBG($T$, $\varepsilon$) in the same height as the middle RFBG($T$) recorded the axial strain progression during the casting and solidification process. The Bragg wavelengths of the RFBG($T$, $\varepsilon$) and the middle RFBG($T$) in all five individual experiments as a function of time are shown in Fig. 5.11. The copper was in the liquid phase at the beginning of the casting. Thus, no strain was transferred to the fiber, and the Bragg wavelengths of the RFBG($T$, $\varepsilon$) and the RFBG($T$) almost overlapped with each other, as seen in the inset of Fig. 5.11. Then, the copper gradually solidified, and compressive strain due to the

thermal contraction acted on the RFBG($T$, $\varepsilon$), resulting in the separation of the Bragg wavelengths. After cooling down to room temperature, there was a large wavelength difference between RFBG($T$) and RFBG($T$, $\varepsilon$). As seen in Table 5.6, in all the experiments, the final wavelength differences were similar, with an average value of -17.57 nm.
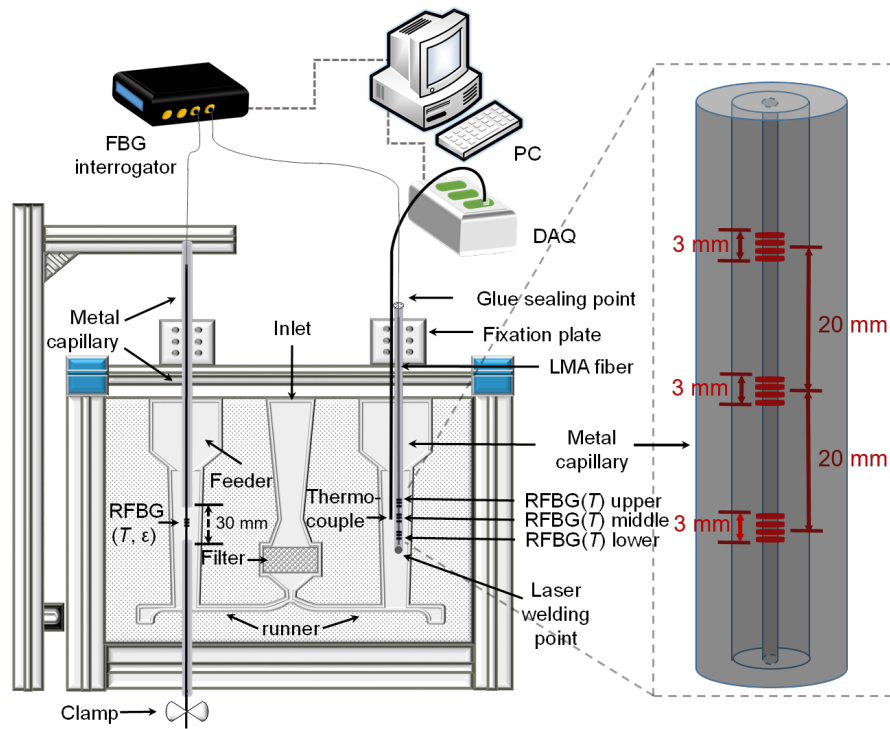


Figure 5.10: Schematic diagram of the copper casting experiment using RFBG sensors for in-situ temperature and strain monitoring.

Table 5.6: Wavelength differences in copper casting experiments.

| Casting Number | 1 | 2 | 3 | 4 | 5 |
|---|---|---|---|---|---|
| Final Wavelength Difference between RFBG($T$) and RFBG($T$, $\varepsilon$) (nm) | -17.39 | -17.59 | -17.43 | -17.58 | -17.84 |

## 5.2.1 Temperature evolution and distribution during copper casting

The wavelength information from RFBG($T$) should be converted into temperature information. The fit coefficients of the polynomial calibration function in Table 5.2 were obtained by the temperature calibration process from room temperature to 800 °C [167], which could not cover the temperature range of copper casting. New fit coefficients need
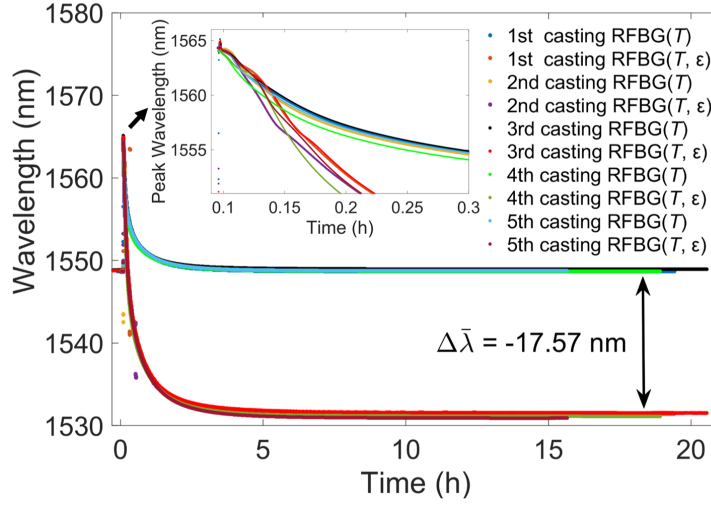
Figure 5.11: Evolutions of the Bragg wavelengths of the middle RFBG($T$)s and the RFBG($T$, $\varepsilon$)s in five copper casting processes.

to be obtained by another calibration process. As we have known in Section 4.2.3, the standardized calibration process performed in the calibration furnace was not suitable for RFBGs when the temperature was over 1000 °C because each temperature step took more than one hour until temperature equilibrium. Considering that the drift rate of RFBG increases dramatically at temperatures over 1000 °C, the calibration process can not be applied at these temperatures.

Here, since the reference Type-K thermocouple was placed at the same position of middle RFBG($T$), we regarded them as sharing the same temperature environment. A new calibration function was obtained by combining the data from the calibration furnace (T≤800 °C) and the data from the first copper casting experiment (T>800 °C), as shown in Fig. 5.12. The blue dots represent the data from the calibration furnace in the standardized temperature calibration process carried out by Hamann, the red dots represent the data from the first copper casting process, and the yellow curve is obtained by the polynomial fit method. The fit coefficients of the fifth-order calibration function from room temperature to 1200°C are shown in Table 5.7.

Table 5.7: Fit coefficients of the polynomial calibration function for the RFBGs on LMA fibers from room temperature to 1200°C.

| Coefficients | $a_1$ (nm/°C) | $a_2$ (nm/°C$^2$) | $a_3$ (nm/°C$^3$) | $a_4$ (nm/°C$^4$) | $a_5$ (nm/°C$^5$) |
|---|---|---|---|---|---|
| Value | 9.51 $\times 10^{-3}$ | 1.04 $\times 10^{-5}$ | -1.14 $\times 10^{-8}$ | 9.92 $\times 10^{-12}$ | -3.85 $\times 10^{-15}$ |

For the sake of a better explanation, the experimental results of the second casting experi-
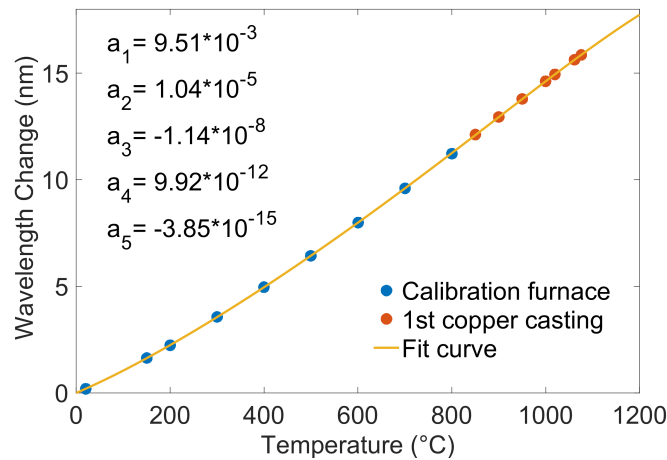
Figure 5.12: The temperature-induced Bragg wavelength change $\Delta\lambda_B(T)$ of the RFBG temperature sensors in LMA fibers and the generalized fifth-order polynomial calibration function.

ment were choose to be plotted as an example. Fig. 5.13(a) shows the whole temperature data from the RFBG temperature sensor array and the thermocouple as a function of time in the copper casting process. As can be seen in Fig. 5.13(b), after pouring, the temperature increased immediately from room temperature to $\sim$1134 °C. Considering the variations in the experimental environment, the maximum temperature measured by the RFBG($T$)s in each casting experiment differed from 1065 to 1134 °C, as shown in Table 5.8. Because of the position difference, the hot liquid copper alloy reached the RFBG($T$) at the lower position first. Then, the liquid level rose and reached the other two RFBG($T$)s successively. Therefore, as shown in the inset of Fig. 5.13(b), the increase in temperature was first observed at the lower position and later at the upper position. Owing to the fact that the liquid alloy already started to cool down because of the heat transfer between the melt and the casting mold, the lower RFBG temperature sensor showed the highest peak temperature compared with the other two. At point A in Fig. 5.13(b), the molten copper alloy started to solidify, and the solidification latent heat was released, making the temperature drop rates significantly slower. Considering the structure of the casting mold, there was a feeder containing a large amount of melt at the top, which provided additional heat to the upper part of the cast alloy. Therefore, the temperature drop rate decreased successively from the lower position to the upper position. At point B, the temperature curves intersected, and since then, the lower position underwent the relatively lowest temperature until the whole cast part gradually cooled down to room temperature after $\sim$10 hours. This temperature distribution behavior was similar to that of aluminum alloy with the same casting mold structure as mentioned in the last section.

(a)                                                    (b)
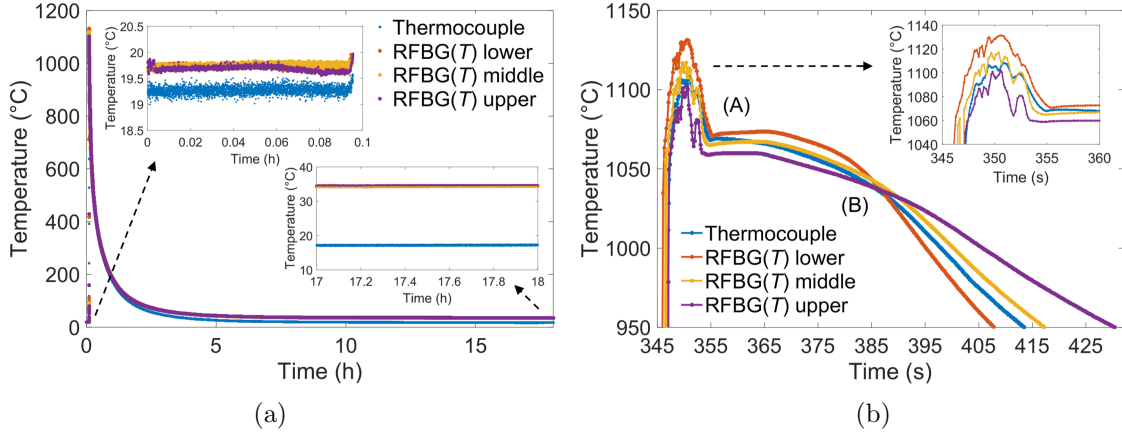
Figure 5.13: Temperature measurement during the copper casting experiment as a function of time: (a) during the whole casting and cooling process, (b) at the beginning of the casting.

Table 5.8: Maximum temperatures measured by the RFBG($T$)s in copper casting experiments.

| Casting Number | 1 | 2 | 3 | 4 | 5 |
|---|---|---|---|---|---|
| Maximum Temperature (℃) | 1098 | 1134 | 1133 | 1065 | 1091 |

It can be seen in Fig. 5.13(b) that, at high temperatures, the temperature information from the middle RFBG temperature sensor (yellow line) agreed well with that from the reference thermocouple (blue line) at the same position, even at temperatures exceeding 1100 ℃. However, it has been found that there were permanent Bragg wavelength red drifts in RFBG($T$)s due to the high temperature during casting. As seen in the insets of Fig. 5.13(a), before the casting, the temperature differences at room temperature between RFBG($T$)s and thermocouple were less than 1 ℃, whereas the temperature differences became 17.3 ℃ after the casting, which was caused by the error from the permanent drift. For casting experiments, the main focus is to monitor the temperature variation as well as the temperature gradient at high temperatures because they reveal the movement of the solidification front and determine the final cast parts' structural properties and residual stresses. In this case, our casting experiments showed that the RFBG temperature sensor array could provide valuable temperature distribution information for copper casting.

## 5.2.2  Strain evolution during copper casting

As discussed in Section 5.1.2, for RFBG($T$, $\varepsilon$)s, the strain-induced Bragg wavelength variation, $\Delta\lambda_{B,RFBG(T,\varepsilon)}(\varepsilon)$ can be obtained by subtracting the wavelength variations of

the corresponding RFBGs from both arms at the same height. As a simplified approach, the temperature-dependent relative strain sensitivity $k_\varepsilon(T)$ (see Fig. 5.7) was extended up to 1200 °C. Then, the strain obtained from RFBG($T$, $\varepsilon$) can be calculated and can be depicted as a function of temperature, using the temperature information provided by the middle RFBG($T$).

Fig. 5.14(a) shows the strain evolutions in five copper castings as a function of temperature. Here, it can be seen that, due to the shrinkage of copper during cooling, the RFBG($T$, $\varepsilon$) experienced a very strong compressive strain ~14000 $\mu\varepsilon$ when the cast part cooled down to room temperature. From high temperatures to room temperatures, the strain behaviors can be divided into three phases. From casting temperature to ~1000 °C (phase-I), the copper was still in the liquid phase, and no strain was acting onto the fiber. In phase-II at temperatures between ~700 °C and ~1000 °C, obvious disturbances were observed. These disturbances might relate to the fiber's transition from viscoelasticity to elasticity [78], and might also relate to the characteristics of the copper alloy, considering that the hot working temperature range of CuSn2 is 750 - 850 °C [176]. At temperatures lower than 700 °C in phase-III, all experimental results showed similar behaviors because the copper alloy was completely solidified and the relative position between the fiber and the copper alloy was stable.
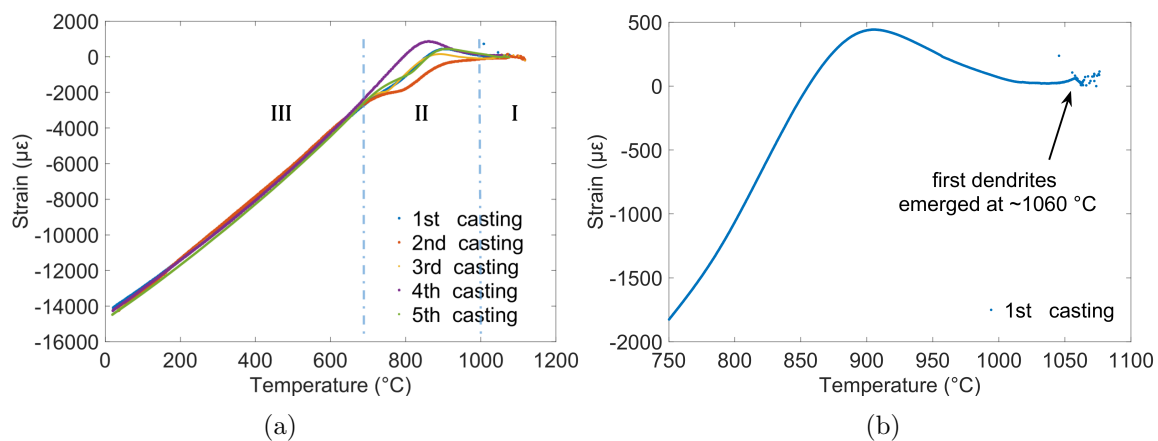


Figure 5.14: Strain evolutions during the copper casting and cooling process as a function of temperature: (a) all five castings in the temperature range of 0-1200 °C, (b) the first casting in the temperature range from casting temperature to 750 °C.

In order to have a closer look at the details of the strain progression at high temperatures, the results from the first copper casting experiment were chosen and zoomed in at temperatures above 750 °C, as seen in Fig. 5.14(b). At the very beginning of the casting, the copper was still in the liquid phase. Almost no strain but disturbances were transferred into the fiber. The first dendrites emerged from the melt at ~1060 °C, and a slight ten-

sile strain was observed, exactly corresponding to the point A in Fig. 5.13(b) when the solidification latent heat was released. Another obvious tensile strain at the temperature of 900 ℃ might relate to the thermal stress caused by the temperature difference between the core and the edge of the cast part when the core shrinkage was hampered by the already cooled edge zone, causing tensile stresses in the core and compressive stresses at the edge [7, 173].

It has been found in Section 5.1.3 that the solidification characteristics of aluminum alloy can be detected through strain information obtained from RFBG sensors. For our copper casting experiments, considering the copper alloy used in this research was a kind of alloy with very high copper concentration, no special solidification reaction or phase was expected according to the copper-tin phase diagram [177]. In spite of this, our results showed that, with our RFBG sensors, in-situ strain behavior during the copper casting process could be detected, and the highest temperature was over 1100 ℃.

# Chapter 6

# Structural health monitoring with embedded FBG sensors

OFSs have the merits of small size, design flexibility, immunity to electromagnetic interference, resistance to corrosion, and the capacity to achieve distributed sensing, which make them become a mainstream sensing technology more than just a laboratory exploration. In recent years, OFSs have been applied for SHM of numerous facilities and structures [112, 154–160].

In the last chapter, it has been shown that, with casting processes, bare optical fibers can be embedded into metals like aluminum and copper. The survived FBG sensors can further be used for SHM of the metal structures. In this chapter, the embedding situation and temperature response of the fiber-embedded metal cast parts were studied. Several tensile tests were carried out for aluminum specimens with the axial strain monitored by the embedded FBG sensors inside. A temperature and external axial strain decoupling method for fiber-embedded metal structures was proposed and demonstrated.

## 6.1   Fiber-embedded metal cast parts

Fig. 6.1 shows the picture of two fiber-embedded metal cast parts obtained by the casting processes. The left one is a copper cast part, while the right one is an aluminum cast part. For every cast part, the left arm has at least one FBG strain sensor $\text{FBG}(T, \varepsilon)$ which survives after the metal casting process, so the arm with $\text{FBG}(T, \varepsilon)$ is also called "strain arm". In this section, the main focus is on those $\text{FBG}(T, \varepsilon)$s because they have the fiber parts in direct contact with the metals.
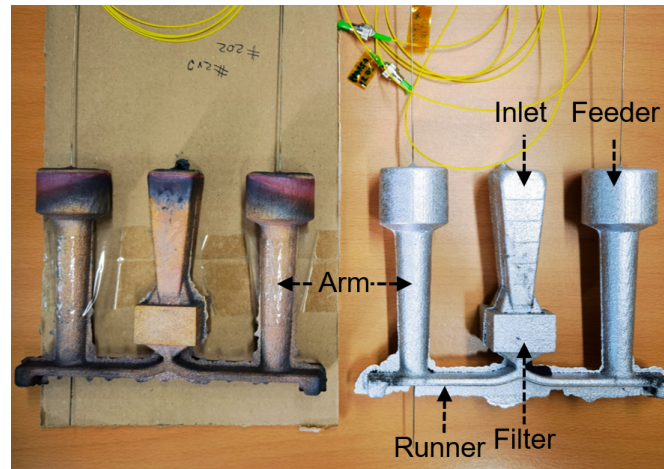
Figure 6.1: Fiber-embedded metal cast parts: aluminum alloy cast part (right) and copper alloy cast part (left).

### 6.1.1 Fiber embedding condition in metal cast

The fiber embedding conditions in aluminum and copper cast parts were studied by cutting their strain arms, respectively. For aluminum, an old cast part obtained from the previous experiments done by Lindner [61] was used. It should be noticed that the embedded fiber was a single-mode fiber (GF1B, Nufern, East Granby, USA) with a diameter of 125 μm, and the fiber had not been annealed before the casting. The aluminum alloy was AlSi9Cu3. Figs. 6.2(a) to 6.2(d) show the microscopic pictures of the cross section of the aluminum cast part at different positions of the strain arm. It
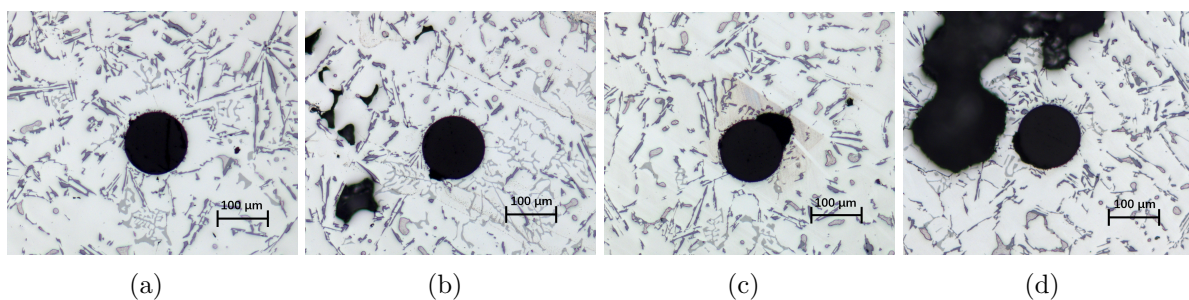


Figure 6.2: Microscope pictures of the cross section of the aluminum cast at (a) position 1, (b) position 2, (c) position 3, (c) position 4.

can be seen that at different positions, the embedding conditions of the embedded fiber show some differences. At position 1, the fiber was fully surrounded by the aluminum alloy without any obvious gap or void. While some voids can be seen in the boundary between fiber and surrounding aluminum alloy at positions 2 to 4. These voids might influence the strain transferred from the aluminum to the fiber. It can also be seen that,

at position 2 and position 4, there are some defects/cavities in the aluminum alloy, which were probably caused by slags or inhomogeneous cooling.



(a)                               (b)                               (c)
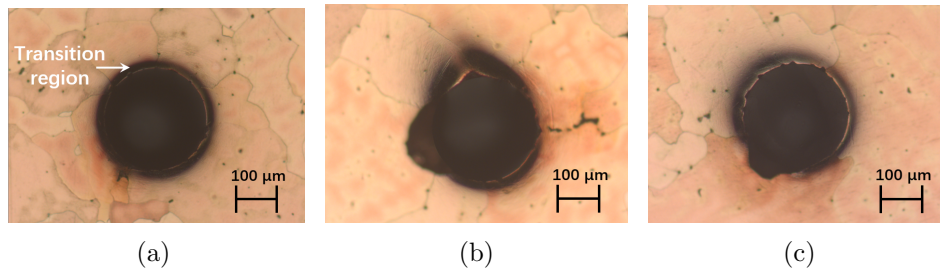
Figure 6.3: Microscope pictures of the cross section of the copper cast at (a) position 1, (b) position 2, (c) position 3.

Figs. 6.3(a) to 6.3(c) show the microscopic pictures of one copper cast part at different positions of the strain arm. This copper cast part was from one of the copper casting experiments mentioned in Section 5.2, so the used fiber was an annealed LMA fiber with a diameter of 250 µm, and the copper alloy was CuSn2. It can be seen that the embedding condition seems a little better than the fiber in the aluminum cast part because fewer voids or defects appeared. However, different from the aluminum cast part, there was a transition region between fiber and copper at the boundary, showing that the boundary condition between copper and fiber might have changed due to the ultra-high temperature in copper casting.



(a)                               (b)
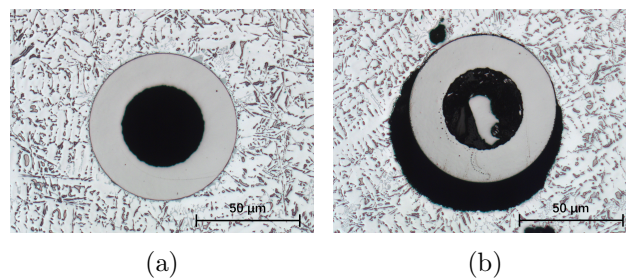
Figure 6.4: Microscope pictures of the cross section of the aluminum cast (with capillary) at (a) position 5, (b) position 6.

Some positions in the strain arm also included capillaries, and their embedding conditions were also investigated. Figs. 6.2(c) and 6.4(b) show the microscopic pictures of the cross section of the aluminum cast part at another two positions, where capillaries were embedded as well. It can be seen at position 5, the embedding condition was very good without any void or defect, while at position 6, a terrible embedding with large defects

was observed. It is believed that the capillaries might make the embedding condition of fiber unpredictable, so the location of FBG($T$, $\varepsilon$) should be away from the capillaries.

## 6.1.2 Interaction between embedded fiber and metal at different temperatures

In metal cast parts, FBG($T$, $\varepsilon$)s are located at positions where the fibers are in direct contact with the metal. The temperature and strain sensitivities mentioned in Section 2.2.1 are mainly for FBGs on free fibers. While, for FBGs in the fibers embedded in metal cast parts, considering the large differences between the material properties of fiber and metal, the mechanical interaction and stress transition between them need to be discussed.

As shown in the last subsection, the fiber was wrapped by aluminum or copper, which means both temperature and stress (strain) from surrounding metals could influence the FBG($T$, $\varepsilon$)s. Even though no external strain was applied, when the temperature changed, the interaction between the metal and the fiber could bring thermal strain. In Fig. 6.2(a), the fiber was fully surrounded by aluminum without obvious gap or void, and this structure can be simplified as a shrink-fit model [178–180], whose schematic diagram is shown in Fig. 6.5.
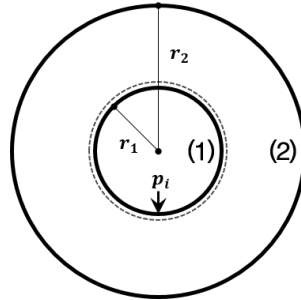


Figure 6.5: Schematic diagram of shrink-fit model.

According to the Lamé solutions, the radial stress caused by the thermal contraction at the interface between fiber and metal can be expressed as follows [181, 182]:

$$\sigma_r = \frac{r_1^2}{r_2^2 - r_1^2}(1 - \frac{r_2^2}{r_1^2})p_i, \tag{6.1}$$

where $r_1$ and $r_2$ are the radii of the internal structure (1), which is optical fiber, and the surrounding structure (2), which is cast metal, respectively. $p_i$ is the internal pressure

from structure (1) to structure (2), and it can be formulated as [178, 179]:

$$p_i = \frac{(\alpha_2 - \alpha_1)E_2 E_1 (r_2^2 - r_1^2)\Delta T}{\{[(1+\nu_2)E_1 + (1-\nu_1)E_2]r_2^2 - [(1-\nu_2)E_1 + (1-\nu_1)E_2]r_1^2\}}. \tag{6.2}$$

Here, $\alpha_i$, $E_i$, and $\nu_i$ are CTE, Young's modulus, and Poisson's ratio of structure (i). The total radial strain $\varepsilon_r$ and the total axial strain $\varepsilon_z$ of the fiber can be written as:

$$\varepsilon_r = \varepsilon_{rr} + \varepsilon_{zr}, \tag{6.3}$$

$$\varepsilon_z = \varepsilon_{zz} + \varepsilon_{rz}, \tag{6.4}$$

where $\varepsilon_{rr}$ is the pure radial strain, $\varepsilon_{zr}$ is the transversal effect of the axial strain, $\varepsilon_{zz}$ is the pure axial strain, and $\varepsilon_{rz}$ is the transversal effect of the radial strain. According to the shrink-fit model, these strains can be expressed as follows [178, 179]:

$$\varepsilon_{rr} = \frac{1-\nu_1}{E_1}p_i, \tag{6.5}$$

$$\varepsilon_{rz} = -\frac{2\nu_1}{E_1}p_i, \tag{6.6}$$

$$\varepsilon_{zz} = \frac{(\alpha_2 - \alpha_1)E_2(r_2^2 - r_1^2)}{E_1 r_1^2 + E_2(r_2^2 - r_1^2)}\Delta T, \tag{6.7}$$

$$\varepsilon_{zr} = -\nu_1\varepsilon_{zz}. \tag{6.8}$$

Considering the radius of the surrounding metal is much larger than that of the fiber ($r_2 \gg r_1$), Eqs. 6.2 and 6.7 can be simplified as follows [28]:

$$p_i = \frac{(\alpha_2 - \alpha_1)E_2 E_1}{(1+\nu_2)E_1 + (1-\nu_1)E_2}\Delta T, \tag{6.9}$$

$$\varepsilon_{zz} = (\alpha_2 - \alpha_1)\Delta T. \tag{6.10}$$

With total radial and axial strains obtained from the shrink-fit model, the thermal strain-induced Bragg wavelength change $\Delta\lambda_B(\varepsilon_{the})$ can be predicted according to Eq. 2.40 [37, 183]:

$$\Delta\lambda_B(\varepsilon_{the}) = \lambda_B\{\varepsilon_z - \frac{n_{eff}^2}{2}[p_{12}\varepsilon_z + (p_{12} + p_{11})\varepsilon_r]\}. \tag{6.11}$$

Therefore, it can be seen that when the temperature changes, different from FBG($T$), the

Bragg wavelength change of FBG($T$, $\varepsilon$) includes two parts:

$$\Delta\lambda'_B(T) = \Delta\lambda_B(T) + \Delta\lambda_B(\varepsilon_{the}), \qquad (6.12)$$

where $\Delta\lambda_B(T)$ is the pure temperature-induced Bragg wavelength change, and $\Delta\lambda_B(\varepsilon_{the})$ is the wavelength change caused by the thermal strain.

The CTEs of aluminum $\alpha_{alu}$ and copper $\alpha_{cu}$ are about 40 and 30 times larger than the CTE of fiber $\alpha_{fiber}$, respectively, so it can be expected that the temperature sensitivities of FBG($T$, $\varepsilon$)s embedded in metal cast parts are much larger than that of a normal FBG in a free fiber.

### 6.1.3 Temperature response of the fiber-embedded metal cast parts

The fiber-embedded metal cast parts were heated up in temperature steps to know their real temperature responses at different temperatures, i.e., the temperature sensitivities of embedded FBG($T$, $\varepsilon$)s. Fig. 6.6(a) shows the schematic diagram of a temperature response test of the fiber-embedded metal cast parts. One fiber-embedded aluminum cast part and one fiber-embedded copper cast part were put into a climatic chamber (VCL 4010, Vötsch, Balingen, Germany). The interrogator si255 was used to record the Bragg wavelengths and the spectra of the two RFBG($T$, $\varepsilon$) in the two cast parts, respectively. The commercial PT100 resistive temperature sensor was placed beside the specimen for temperature reference. Two different temperature cycles were carried out in the temperature response test. In the first cycle, the temperature range was from 20 °C to 120 °C, with each temperature step of 20 °C. While, the temperature range in the second cycle was from 0 °C to 180 °C, also with each temperature step of 20 °C. The temperature evolution during the temperature response test measured by the PT100 is shown in Fig. 6.6(b).

The evolutions of Bragg wavelength change of two RFBG($T$, $\varepsilon$) recorded by interrogator si255 are shown in Fig. 6.7. It can be seen that the temperature sensitivity of the RFBG($T$, $\varepsilon$) embedded in aluminum is higher than that embedded in copper due to the higher CTE of aluminum. In the first cycle, both RFBG($T$, $\varepsilon$)s worked well, while the RFBG($T$, $\varepsilon$) in the aluminum cast part showed a permanent wavelength drift when the temperature was over 120 °C in the second cycle. As shown in insets, for the RFBG($T$, $\varepsilon$) in the aluminum cast part, the drift rates were 28.1 pm/h at 160 °C and 71.9 pm/h at 180 °C, while no obvious drift for the RFBG($T$, $\varepsilon$) in copper cast part even at the highest temperature 180 °C could be observed.
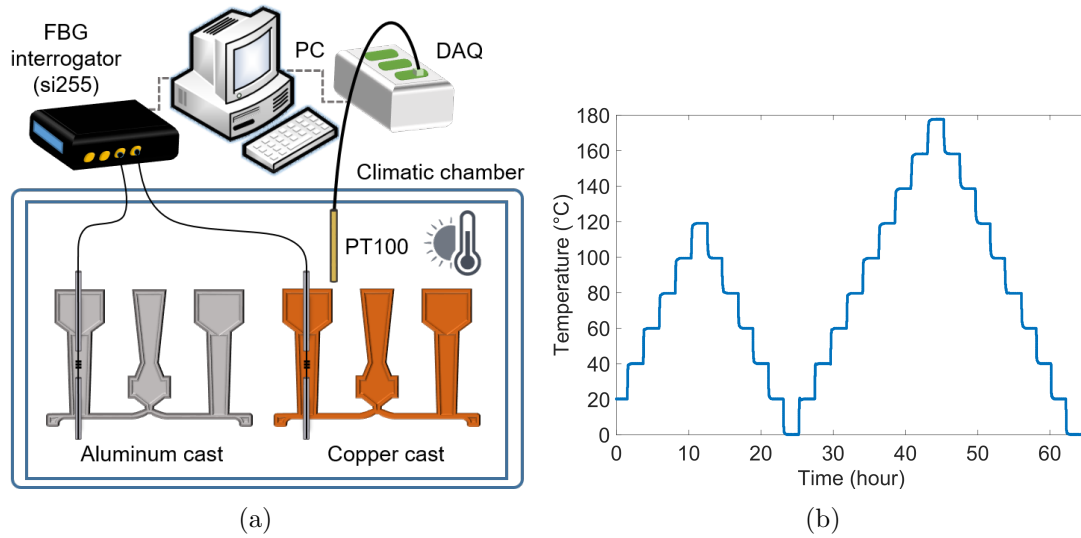
Figure 6.6: (a) Schematic diagram of temperature response test of the fiber-embedded metal cast parts. (b) Temperature evolution measured by the PT100 during the temperature response test.
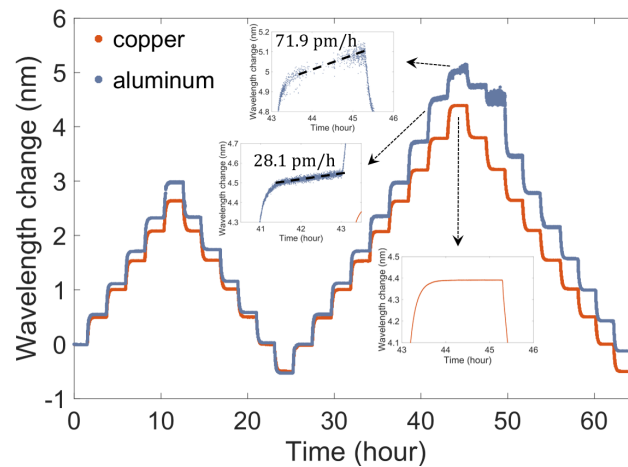


Figure 6.7: Evolutions of the Bragg wavelength changes of the RFBG($T$, $\varepsilon$)s in copper cast and aluminum cast recorded by si255 during the temperature response test.

Besides, the reflectivity of the RFBG($T$, $\varepsilon$) in the aluminum cast part dropped when the temperature increased. At some temperature steps, it was too difficult for the peak-finding algorithm to find the correct peak due to too weak signals, which was the reason for the data disturbance in region A. This kind of reflectivity dropping was not entirely reversible as the temperature cooled down, so the Bragg peak of the RFBG($T$, $\varepsilon$) in the aluminum cast part suffered from permanent wavelength drift and reflectivity decay after the second cycle. While, for the RFBG($T$, $\varepsilon$) in the copper cast part, the reflectivity

increased with temperature, and this kind of reflectivity increase was reversible, so there was almost no change in the spectrum before and after the test. Fig. 6.8 shows the spectra of RFBG($T$, $\varepsilon$)s in aluminum (solid lines) and copper (dashed lines) cast parts at 20 °C at the beginning (1 hour) and at the end of the temperature response test (62 hours). The possible reason for the irreversible behavior of the RFBG($T$, $\varepsilon$) in aluminum cast part might be the relaxation of the thermal stress caused by the material property mismatch between aluminum alloy and silica fiber, and also the artificial aging of aluminum alloy, which was normally in the temperature range of 100-200 °C [184].
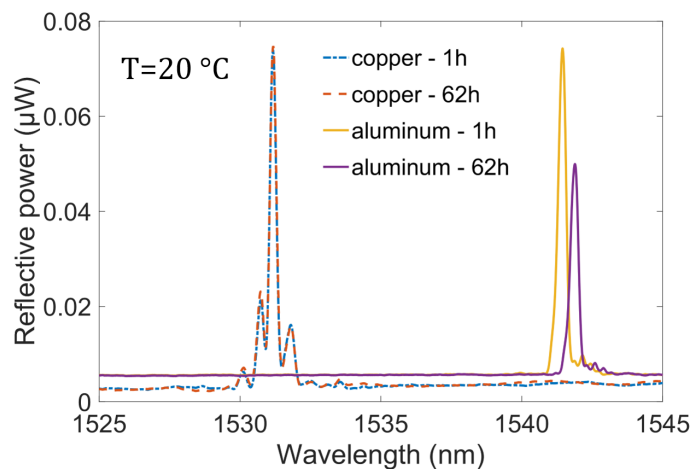


Figure 6.8: Spectra of RFBG($T$, $\varepsilon$)s in aluminum and copper cast parts at 20 °C at the beginning and at the end of the temperature response test.

The Bragg wavelength changes as a function of temperature for the aluminum cast and the copper cast are shown in Figs. 6.9(a) and 6.9(b), respectively. By using the parameters in Tables 5.3 and 6.1, the theoretical thermal strain-induced Bragg wavelength changes calculated by the shrink-fit model in the last subsection can be obtained, which are shown as blue lines. It can be seen that, for the aluminum cast part, the theoretical thermal strain-induced wavelength change agreed well with the experimental results in the first cycle, even with the results of the temperature-increasing steps at temperatures lower than 140 °C. After the permanent drift, it seemed that the temperature sensitivity still kept the same but just with an offset. For the copper cast part, however, there was a big deviation between the theoretical and experimental results. One possible reason might be the transition region between fiber and copper, as shown in Fig. 6.3(a). As discussed in Section 6.1.1, the boundary condition between copper and fiber might have changed due to the ultra-high temperature in copper casting, leading to the failure of the shrink-fit model.
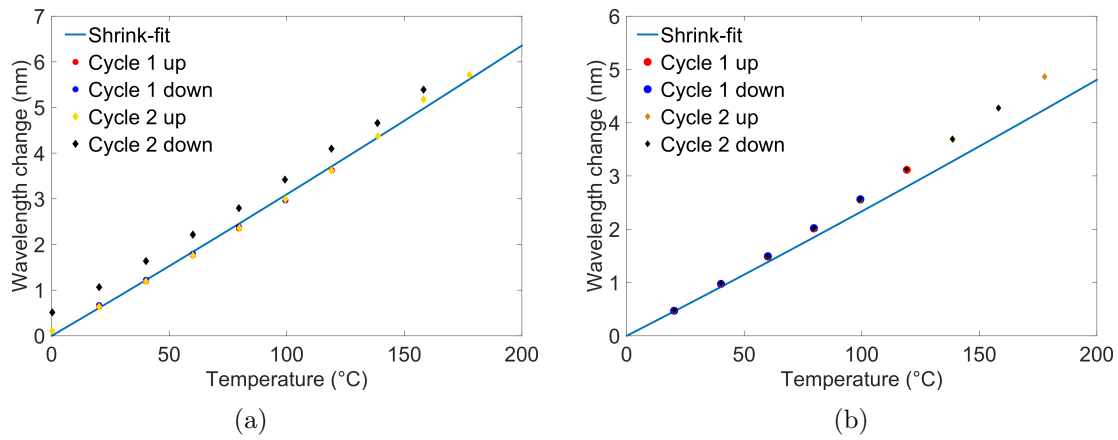
Figure 6.9: Bragg Wavelength changes of the RFBG($T$, $\varepsilon$)s in (a) the aluminum cast part, and (b) the copper cast part as a function of temperature.

In addition, the Bragg wavelength changes of RFBG($T$, $\varepsilon$)s as a function of temperature during the copper casting process have been obtained in the last chapter. Here, for comparison, we put the wavelength change results of RFBG($T$, $\varepsilon$)s in copper from the temperature response test and the casting processes together, as shown in Fig. 6.10. It can be seen that the results overlapped with each other well.
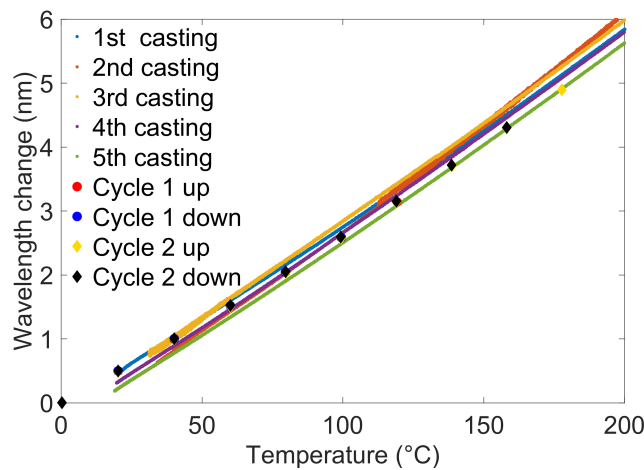


Figure 6.10: Bragg Wavelength changes of RFBG($T$, $\varepsilon$) in copper during the temperature response test and the casting processes.

Table 6.1: Parameters of aluminum alloy and copper alloy.

| Parameter | Value | Source |
|-----------|-------|--------|
| $E_{alu}$ | 73 GPa | [185] |
| $\nu_{alu}$ | 0.33 | [185] |
| $\alpha_{alu}$ | $21 \times 10^{-6}/°C$ | [185] |
| $E_{cu}$ | 110 GPa | [186] |
| $\nu_{cu}$ | 0.36 | [176] |
| $\alpha_{cu}$ | $18.2 \times 10^{-6}/°C$ | [186] |

## 6.2   Strain monitoring on metal structures using embedded FBG sensors

According to the DIN-Standard [187], the strain arms of the metal cast parts could be further machined into a tensile test specimen. Figs. 6.11(a) and 6.11(b) show the pictures of copper and aluminum specimens, respectively, and Fig. 6.11(c) shows the specification of a tensile test specimen. The diameter of the tensile test section was 8 mm, with a uniform region of 40 mm in length. The lower section of the specimen was the feeder. It was kept unchanged because it could not be removed due to the fiber and the capillary inside (see Fig. 6.1). In this section, several tensile tests were carried out to monitor the external strain loads on the aluminum tensile test specimens. Those specimens were fabricated by the aluminum cast parts from the previous experiments done by Lindner, and Stadler [61, 188]. The embedded fibers were all GF1B fibers, and the aluminum alloy was still AlSi9Cu3.

Several tensile tests were carried out with a tensile test machine (Type 1484, ZwickRoell, Ulm, Germany) in the Chair of Metal Forming and Casting. Figs. 6.12(a) and 6.12(b) show the schematic diagram and the picture of the field experiment of a tensile test. In this experiment, a tensile test specimen with a FBG array was used for the test. The inset in Fig. 6.12(a) shows the internal structure of this specimen. The FBG array in the GF1B fiber consists of three FBG($T$, $\varepsilon$)s from the upper to the lower position and the distance between adjacent FBG($T$, $\varepsilon$)s was 12 mm. In the tensile test, three strain gauges (1-LY13-3/350A, HBM, Darmstadt, Germany) were attached at the corresponding heights of FBG($T$, $\varepsilon$)s on the surface of the test region for strain reference. An extensometer was used to measure the displacement $\Delta l$, so another strain reference could be obtained by $\varepsilon = \Delta l/l$, where $l$ is the distance between between the two measuring rods of the extensometer. The room temperature during the experiment was stable, whose average value was 20.8 °C measured by the PT100 resistive temperature sensor.
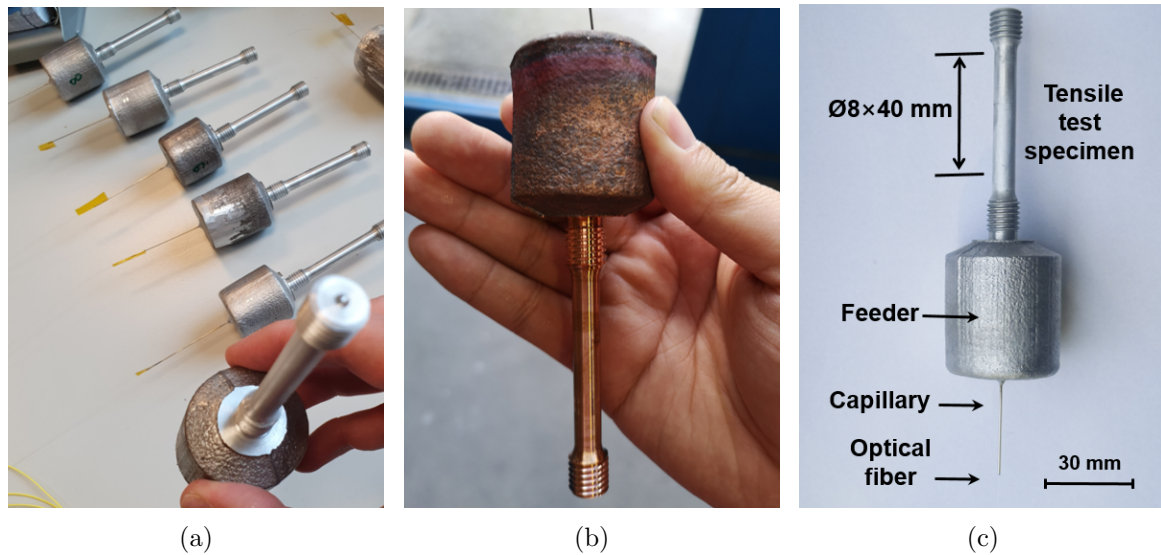
Figure 6.11: Pictures of (a) aluminum tensile test specimens, (b) a copper tensile test
specimen. (b) Specification of a tensile test specimen.
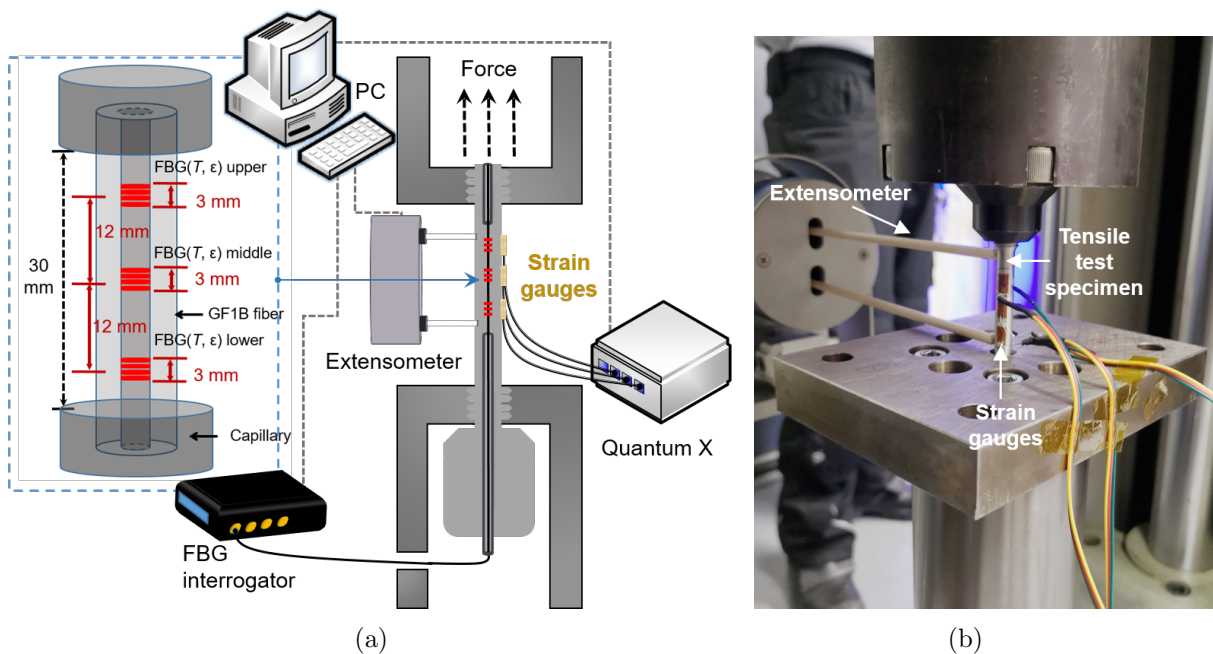


Figure 6.12: (a) Schematic diagram of, (b) picture of the field experiment of a tensile test
on an aluminum specimen.

Two force cycles were carried out in the first tensile test by the tensile test machine. In each cycle, tens of steps were carried out, and every step consisted of a force-applying and a force-releasing processes, both lasting 30 seconds. The applied force started from 0 N and increased by 50 N after every step. The maximum force reached 4000 N. Fig. 6.13(a) shows the schematic diagram of the force cycles. The strain results measured by the strain gauges at the different positions and the extensometer are shown in Fig. 6.13(b). Fluctuations could be seen at the beginning of each cycle because there were some relative movements due to the unstable connection between the specimen and the fixation frame of the test machine. In addition, in the first cycle, the specimen experienced both plastic and elastic strains at large applied forces. Fig. 6.13(c) shows the schematic diagram of the total strain experienced by the specimen in one step, for example. When the force was applied, the total strain $\varepsilon_{total}$ consisting of elastic strain $\varepsilon_{el}$ and plastic strain $\varepsilon_{pl}$ occurred in the specimen, but the plastic part remained as the force was released. Therefore, the elastic strain, which was used for calculating the strain sensitivity, can be obtained as follows:

$$\varepsilon_{el} = \varepsilon_{total} - \varepsilon_{pl}. \tag{6.13}$$

The measurement results in the second cycle, however, did not show any plastic strain at large applied forces anymore. It seemed that the force range when no plastic strain would occur had been extended during the first cycle. Work hardening effect [189], also known as strain hardening effect, might be the main cause of this behavior. This effect originates from the strengthening of a metal by plastic deformation because of dislocation movements and dislocation generation within the crystal structure of the material. For aluminum alloy, it can be strengthened via work hardening. By setting the Bragg wavelengths at the beginning of the test without external strain as offsets, the wavelength changes of three FBG($T$, $\varepsilon$) could be obtained, as shown in Fig. 6.13(d). The wavelength change used for the strain sensitivity calculation in the first cycle was obtained in the same way as elastic strain:

$$\Delta\lambda_B(\varepsilon_{ext}) = \Delta\lambda_{el} = \Delta\lambda_{total} - \Delta\lambda_{pl}. \tag{6.14}$$

The external strain sensitivity could be calculated with the linear fit method, as shown as follows:

$$K_\varepsilon = \frac{\Delta\lambda_B(\varepsilon_{ext})}{\varepsilon_{ext}} = \lambda_0 k_\varepsilon, \tag{6.15}$$

where $K_\varepsilon$ is the external strain sensitivity of embedded FBG($T$, $\varepsilon$), and $k_\varepsilon$ is the k-factor. The theoretical calculated k-factor for FBG($T$, $\varepsilon$) embedded in aluminum cast parts was reported to be 0.826 [28] ($K_\varepsilon$=1.27 pm/$\mu\varepsilon$ at 1540 nm). As a comparison, the k-factor for a FBG in a free fiber was measured to be 0.795 [77] ($K_\varepsilon$=1.22 pm/$\mu\varepsilon$ at 1540 nm).

The strain information recorded by the strain gauges showed a big difference between
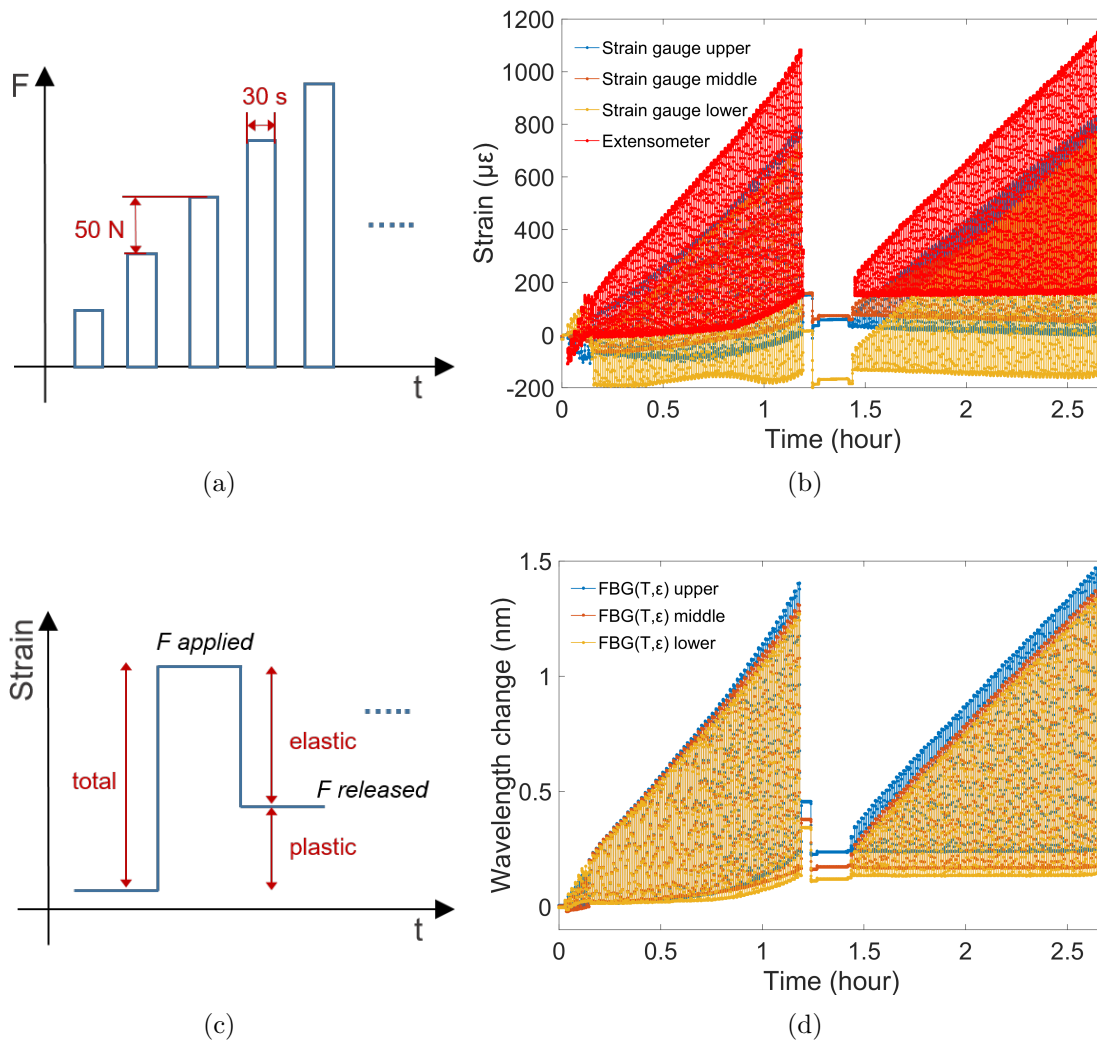
Figure 6.13: (a) Schematic diagram of the force cycles. (b) Strain measurement results
by strain gauges and by extensometer. (c) Schematic diagram of the elastic and plastic
strains. (d) Wavelength changes of RFBG($T$, $\varepsilon$)s.

each other (see Fig. 6.13(b)). At the maximum force, the strain recorded by the lower
strain gauge was over 800 $\mu\varepsilon$ while by the middle strain gauge lower than 500 $\mu\varepsilon$. This
resulted in a large deviation in the strain sensitivities of each FBG($T$, $\varepsilon$)s, as shown in Fig.
6.14(a). The possible reason is that the force applied during the test is not completely
axial, and the strain gauge attached to the surface may also be affected by the bending
of the surface. Therefore, it was preferred to use the strain information provided by the
extensometer for reference values. Figs. 6.14(b) and 6.14(c) show the wavelength changes
recorded as a function of strain in 1st and 2nd cycles, respectively, with the extensometer
giving reference strain values.

Considering the fluctuations caused by the unstable connection between the specimen and the fixation frame of the machine, it was preferred not to use the strain data below 200 $\mu\varepsilon$. The strain sensitivities obtained by the linear fit are listed in the figures, and the k-factors are shown in Table 6.2.
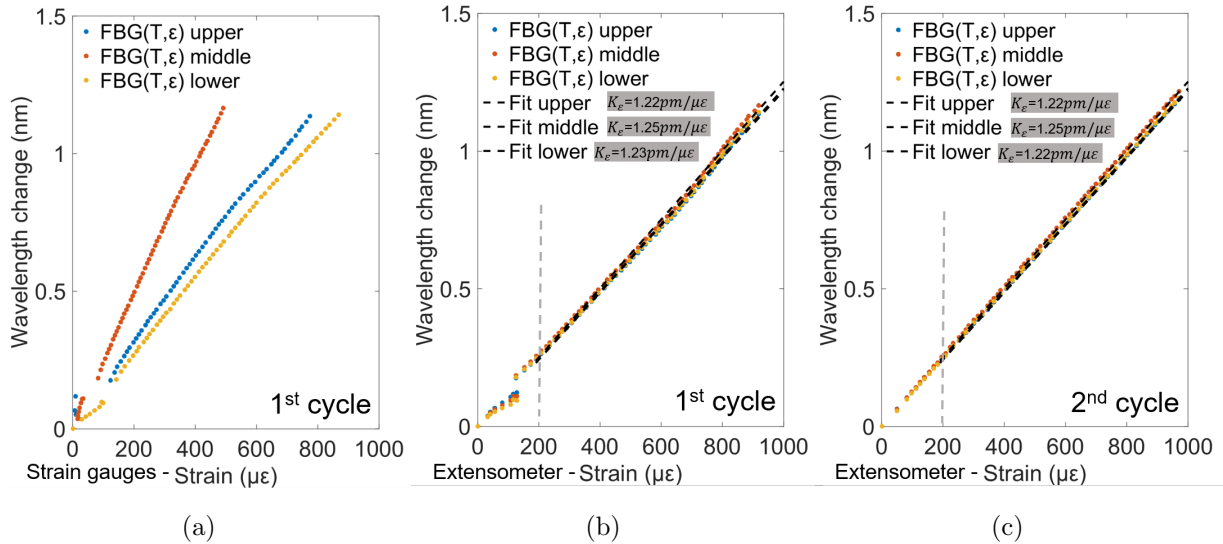


Figure 6.14: Wavelength changes as a function of strain recorded by (a) the strain gauges in 1st cycle, (b) the extensometer in the 1st cycle, and (b) 2nd cycle.

Another tensile test, including three cycles, was carried out with another aluminum tensile test specimen. Same as 1st tensile test, every step consisted of a force-applying and a force-releasing processes, with each step increasing by 50 N. The maximum force this time was 4500 N. The tensile test specimen used this time had the same internal structure as the last one, where three FBG$(T, \varepsilon)$s had been embedded inside. The Bragg wavelength changes of three embedded FBGs during the test are shown in Fig. 6.15(a). Based on the experience from the first tensile test, it was preferred to use the strain information provided by the extensometer, as shown in Fig. 6.15(b). Fluctuations due to unstable connections between the specimen and the fixation frame could also be seen at the beginning. This time, the fluctuation range was larger, and it was preferred not to use the strain data below 500 $\mu\varepsilon$. The wavelength changes as a function of strain recorded by the extensometer during the three different cycles are shown in Figs. 6.16(a), 6.16(b) and 6.16(c), respectively. The strain sensitivities obtained by the linear fit are listed in the figures, and the k-factors are shown in Table 6.2.

The obtained k-factors of the FBG$(T, \varepsilon)$s from the tensile tests were larger in the first cycles and smaller in the following cycles. This means that our method of obtaining the
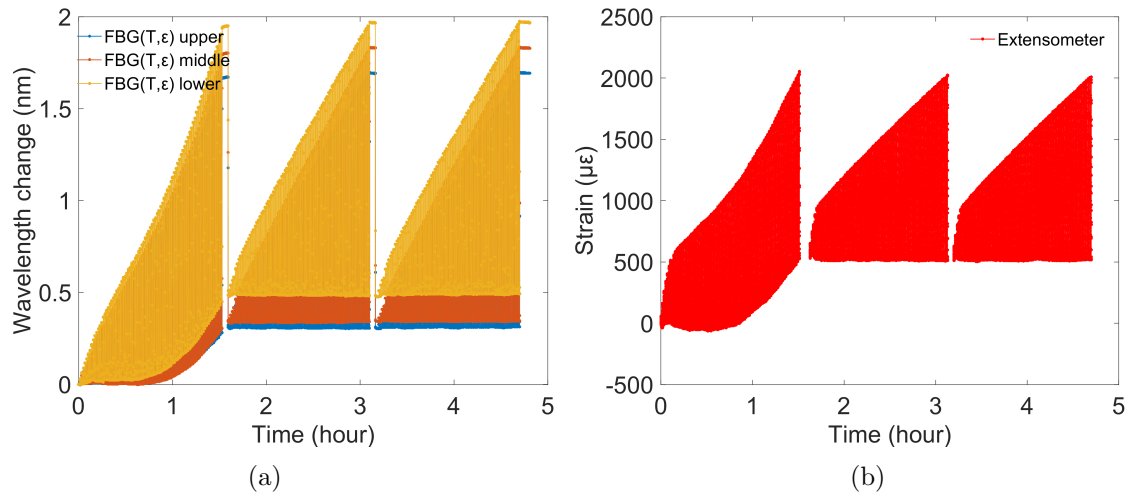
Figure 6.15: (a) Wavelength changes of RFBG($T$, $\varepsilon$)s, (b) Strain measurement results by
extensometer during the second tensile test.
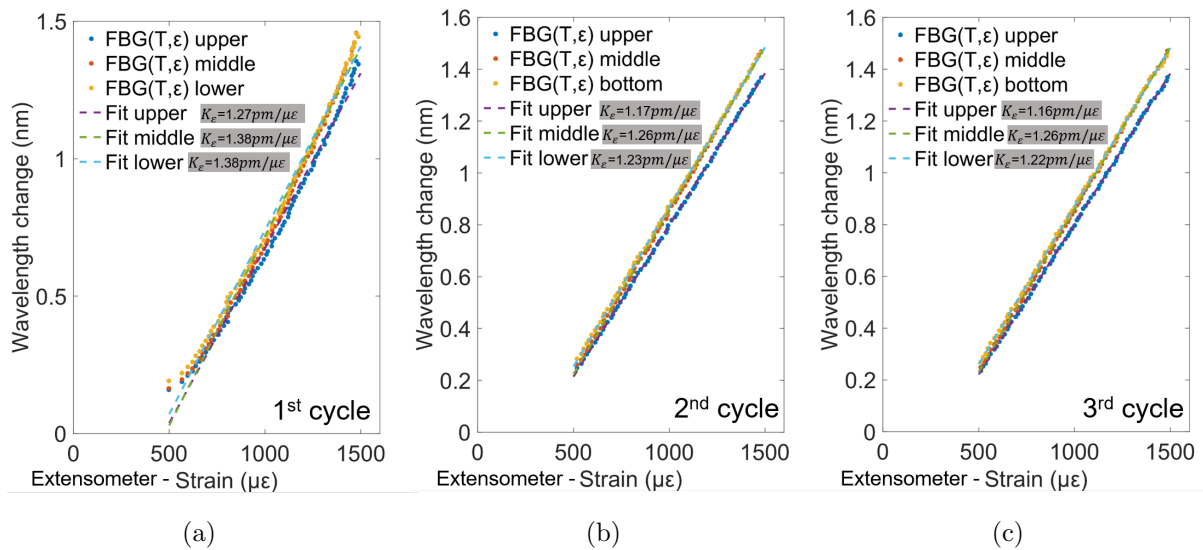


Figure 6.16: Wavelength changes as a function of strain recorded by extensometer over
500 $\mu\varepsilon$ in (a) 1st cycle, (b) 2nd cycle, (c) 3rd cycle.

elastic strain through the Eq. 6.13 was not accurate enough. The results from the second
and third cycles agreed well, showing good repeatability in the elastic region. It should
be noticed that always the middle FBG($T$, $\varepsilon$)s showed the largest k-factor, the possible
reason for which might be the less influence from the capillaries: the upper and lower
FBG($T$, $\varepsilon$)s were only 3 mm away from the corresponding capillaries, as shown in the
inset of Fig. 6.12(a).)

Table 6.2: k-factor for FBG($T$, $\varepsilon$) in two tensile tests.

| Tensile test No. | FBG position | 1st Cycle | 2nd Cycle | 3rd Cycle |
|---|---|---|---|---|
| 1st | Upper | 0.789 | 0.790 | - |
|  | Middle | 0.817 | 0.814 | - |
|  | Lower | 0.801 | 0.796 | - |
| 2nd | Upper | 0.833 | 0.761 | 0.765 |
|  | Middle | 0.896 | 0.818 | 0.823 |
|  | Lower | 0.867 | 0.794 | 0.769 |

The obtained k-factors from the middle FBG($T$, $\varepsilon$)s agreed well with the theoretical value calculated by Lindner et al. [28], which was 0.826. This agreement verified the validity of Lindner's theory, and also confirmed that the interaction between the aluminum alloy and the optical fiber indeed affected the strain sensitivity of the embedded fiber (the k-factor of a bare optical fiber was 0.795 [77]).

## 6.3 Simultaneously temperature and strain monitoring on metal structures using embedded FBG sensors

Decoupling temperature and external strain is challenging for fiber-embedded metal structures. In this subsection, a method to use embedded FBG sensors to simultaneously monitor the temperature and strain of the metal structure was proposed. Another tensile test specimen obtained by the casting process was used, whose schematic diagram is shown in Fig. 6.17(a). In this fiber, there was a FBG array consisting of a FBG($T$, $\varepsilon$) in direct contact with aluminum and two FBG($T$)s protected inside capillaries. Those two FBG($T$)s provide the temperature information at different positions and are named FBG($T$)-1 for the lower one and FBG($T$)-2 for the upper one. The distance between adjacent FBGs was 12 mm. Fig. 6.17(b) shows a typical reflective spectrum of those embedded FBG sensors at room temperature, obtained by the FBG interrogator sm125. For reference, the inset shows an enlarged spectrum of FBG($T$, $\varepsilon$) obtained with an optical spectrum analyzer (Advantest Q8384, Anritsu, Tokyo, Japan). It can be seen that the reflective power of FBG($T$, $\varepsilon$) was a bit weaker than that of FBG($T$)s because the FBG($T$, $\varepsilon$) suffered from compression and micro bendings during the solidification and cooling process. Temperature and strain calibrations for those embedded OFSs were carried out separately. The cross-sensitivity issue of the middle FBG($T$, $\varepsilon$) could be solved by using the temperature information provided by the FBG($T$)s to compensate for the influence of temperature and thermal strain, so the external strain information can be
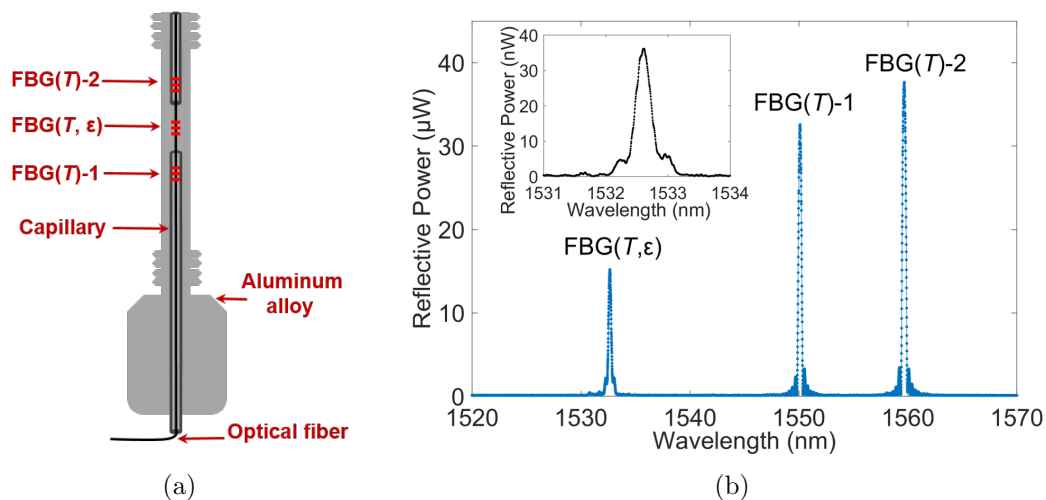
Figure 6.17: (a) Schematic diagram of the aluminum specimen. (b) Spectrum of the aluminum specimen.

obtained. A temperature and external strain measurement experiment was carried out to demonstrate the multiparameter monitoring capability of the system.

## 6.3.1   Temperature calibration

A temperature calibration process was carried out to obtain the temperature sensitivities of the embedded FBG($T$, $\varepsilon$) and FBG($T$)s when no external stress was applied. The aluminum specimen was put into the VCL 4010 climatic chamber. The schematic diagram is similar to the temperature response test in Fig. 6.6(a). The Bragg wavelengths of three FBGs were recorded by the interrogator sm125 with the peak-finding algorithm and then transferred to a PC. The PT100 resistive temperature sensor was placed beside the specimen as a reference. The recorded temperature during the calibration process was shown in Fig. 6.18(a). Two temperature cycles were carried out from 0 to 80 ℃, with a temperature step of 10 ℃ and 2 hours duration at each step. The recorded Bragg wavelength changes of FBG($T$, $\varepsilon$) and FBG($T$)s at different temperatures (0, 10, 20, 30, 40, 50, 60, 70, 80 ℃) in each cycle are shown in Fig. 6.18(b) and 6.18(c), respectively. It can be seen that the experimental results show good repeatability from the 1st cycle to the 2nd cycle. According to the shrink-fit model mentioned in Section 6.1.2 and the parameters in Tables 5.3 and 6.1, the theoretical Bragg wavelength change of the embedded FBG($T$, $\varepsilon$) at different temperatures can be calculated, as shown as the black dashed line in Fig. 6.18(b). The theoretical calculations agreed well with the experimental results, proving the availability of the shrink-fit model for the fiber-embedded aluminum specimen.

A polynomial function of temperature $T$ can be used to represent $\Delta\lambda_B(T)$. In this temperature range, to achieve higher precision and to better decouple temperature and strain, a second-order calibration polynomial function

$$\Delta\lambda_B(T) = a_1^T T + a_2^T T^2 \tag{6.16}$$

was used for FBG($T$)s according to the polynomial fit method, as shown in the solid blue line in Fig. 6.18(c). Another second-order calibration was used to represent $\Delta\lambda'_B(T)$, which can be expressed as

$$\Delta\lambda'_B(T) = a_1^{T,\varepsilon} T + a_2^{T,\varepsilon} T^2. \tag{6.17}$$

The fit coefficients of the calibration functions $a_1^{T,\varepsilon}$ and $a_2^{T,\varepsilon}$ for FBG($T$, $\varepsilon$), $a_1^T$ and $a_2^T$ for FBG($T$)s, are shown in Table 6.3.
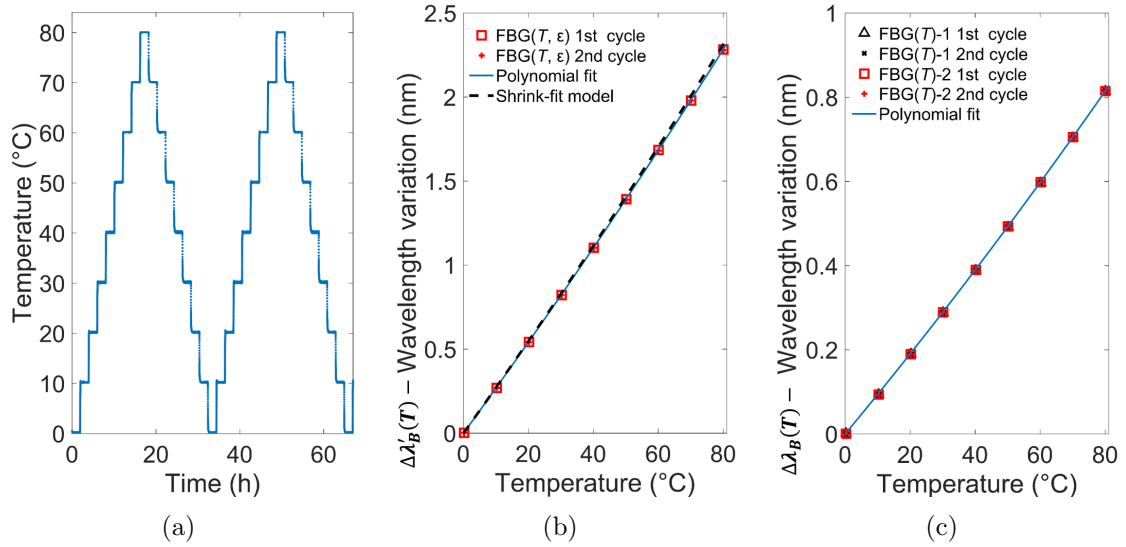


Figure 6.18: (a) Temperature cycles recorded by the PT100 temperature sensor during the calibration process. Bragg wavelength changes of (b) FBG($T$, $\varepsilon$) and (c) FBG($T$)s.

Table 6.3: Fit coefficients of the second-order polynomial calibration function for the FBG sensors.

| Coefficients | $a_1^{T,\varepsilon}$ (nm/°C) | $a_2^{T,\varepsilon}$ (nm/°C$^2$) | $a_1^T$ (nm/°C) | $a_2^T$ (nm/°C$^2$) |
|---|---|---|---|---|
| Value | $2.7 \times 10^{-2}$ | $2.4 \times 10^{-5}$ | $9.3 \times 10^{-3}$ | $1.1 \times 10^{-5}$ |

## 6.3.2 Strain calibration

A strain calibration process at room temperature was carried out to measure the external strain sensitivity $K_\varepsilon$ of the embedded $\mathrm{FBG}(T, \varepsilon)$, as shown in Fig. 6.19. The aluminum specimen was fixed into a custom-built tensile test setup, where the external strain was provided by the weights applied to the frame. It was assumed that the room temperature was stable during the strain calibration, so the influence from thermal strain was negligible.
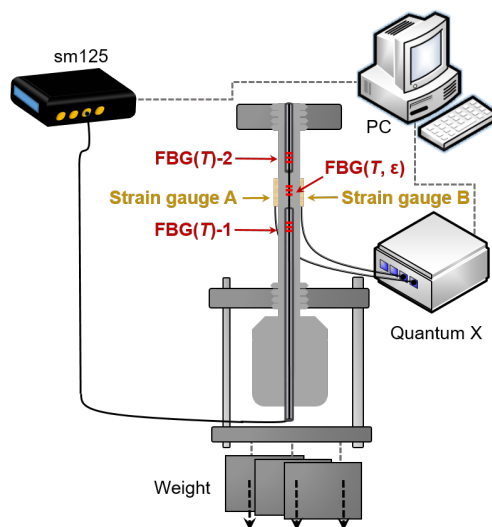


Figure 6.19: Schematic diagram of the strain calibration experiment in a custom-built tensile test setup.

Due to the limitation of our custom-built setup, there was a very slight bending in the specimen during weight loading. Hence, one side was stretched slightly stronger than the other side. It was assumed that this bending effect was mainly significant on the surface of the specimen and could be neglected in the interior of the specimen, where the glass fiber was located. Two strain gauges (1-LY13-3/350A, HBM, Darmstadt, Germany) were glued on two opposite surfaces of the test specimen at the longitudinal position where $\mathrm{FBG}(T, \varepsilon)$ was located, so the bending effect can be compensated by [190]:

$$\varepsilon_{ext,exp} = \frac{\varepsilon_{sg,A} + \varepsilon_{sg,B}}{2}, \tag{6.18}$$

where $\varepsilon_{ext,exp}$ is the experimentally measured external strain, $\varepsilon_{sg,A}$ and $\varepsilon_{sg,B}$ are the strain data obtained from each strain gauges, respectively. During the experiment, the data measured by the strain gauges were collected by a DAQ board (QuantumX MX840B, HBM, Darmstadt, Germany), and the Bragg wavelengths of FBGs were recorded by the interrogator sm125 and then transferred to a PC. An offset weight of 24.76 kg was applied

in advance to consolidate the connection between the specimen and the frame, so their relative movement was reduced to a low level. Starting from the offset weight, when the strain was regarded as zero, the loading weight was increased step by step, from 0 kg to 41.6 kg, with 8 steps of 5.2 kg. Three cycles with loading and unloading steps were carried out to check the experimental repeatability. Fig. 6.20(a) shows the strain data obtained by two strain gauges ($\varepsilon_{sg,A}$ and $\varepsilon_{sg,B}$), and the corresponding experimentally measured strain $\varepsilon_{exp}$ based on Eq. 6.18. It can be seen that our compensation method worked well and the results could also explain why there was a big deviation for the strains measured by the three strain gauges in Section 6.2. According to the theory of linear elasticity, the theoretical external strain can be calculated as follows:

$$\varepsilon_{ext,theo} = \frac{\sigma}{E_{alu}} = \frac{mg}{AE_{alu}} = \frac{mg}{\pi b^2 E_{alu}}, \tag{6.19}$$

where $m$ is the loaded weight, $A$ is the cross-section area of the specimen, $g$ is the gravitational acceleration (9.8 m/s$^2$), and $E_{alu}$ is the Young's modulus of aluminum (73 GPa) . Fig. 6.20(b) shows the theoretically calculated strain $\varepsilon_{ext,theo}$, the experimentally measured strain $\varepsilon_{ext,exp}$ by strain gauges and the corresponding loaded weight. The experimental results agreed well with the theoretical calculations based on Eq. 6.19 using the parameters in Table 6.1. This shows that the theoretical calculations were trustable, and each loaded weight could correspond to each external strain.
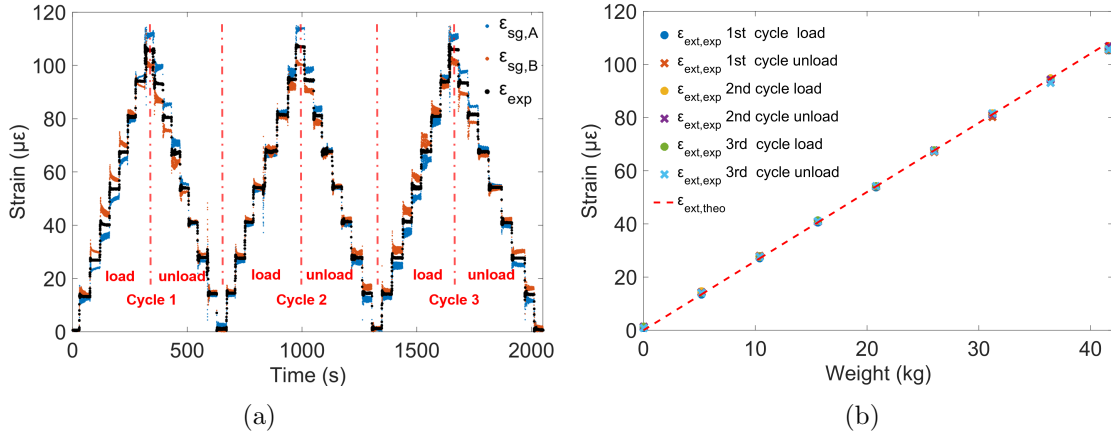


Figure 6.20: (a) Experimentally measured external strain $\varepsilon_{ext,exp}$ by strain gauges in strain calibration process with three cycles. (b) Loaded weight and corresponding experimental/theoretical external strain.

Then, a strain calibration of the embedded FBG($T$, $\varepsilon$) was carried out at room temperature. The Bragg wavelength of FBG($T$, $\varepsilon$) was measured by the interrogator sm125 when the abovementioned three cycles with the same loading and unloading steps were carried
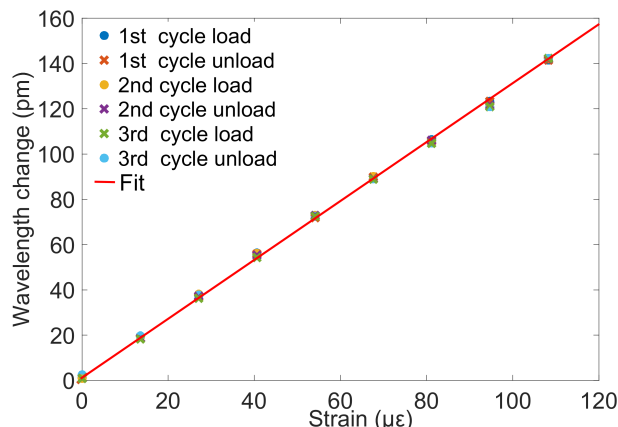
Figure 6.21: Bragg wavelength variation of FBG($T$, $\varepsilon$) under different strains at room temperature.

out. The Bragg wavelength variation under different external strains was obtained, as shown in Fig. 6.21. By averaging the values in each cycle, the external strain sensitivity could be calculated with the linear fit method. According to Eq. 6.15, the external strain sensitivity $K_\varepsilon$ was 1.29 pm/$\mu\varepsilon$ at 1532.5 nm, and k-factor is 0.838.

## 6.3.3    Temperature and strain decoupling

For the embedded fiber sensors, the temperature and external strain sensitivities were obtained respectively by the temperature and strain calibrations described above. For FBG($T$, $\varepsilon$), the Bragg wavelength was influenced by both temperature and external strain, as shown as follows:

$$\lambda_B(T,\varepsilon) = \lambda_0 + \Delta\lambda'_B(T) + \Delta\lambda_B(\varepsilon_{ext}), \tag{6.20}$$

where $\lambda_0$ is the Bragg wavelength at 0 °C and 0 $\mu\varepsilon$, which has been measured in advance. It was assumed that the external strain sensitivity was independent of temperature for the limited temperature range. Therefore, by substituting Eq. 6.15 and Eq. 6.17 into Eq. 6.20, the external strain can be decoupled from the temperature in FBG($T$, $\varepsilon$), as shown as follows:

$$\varepsilon_{ext} = \frac{\lambda_B(T,\varepsilon) - \lambda_0 - a_1^{T,\varepsilon}T - a_2^{T,\varepsilon}T^2}{K_\varepsilon}. \tag{6.21}$$

Here, $T$ is the temperature at the location of FBG($T$, $\varepsilon$), which can be predicted with the temperatures measured by FBG($T$)-1 and FBG($T$)-2 according to an interpolation

method:

$$T = \frac{T_{temp1} + T_{temp2}}{2},  \tag{6.22}$$

where $T_{temp1}$ and $T_{temp2}$ are the temperatures measured by FBG($T$)-1 and FBG($T$)-2, respectively.

A temperature and strain measurement experiment was carried out to check the temperature and external strain sensing ability. The schematic diagram of the setup used is shown in Fig. 6.22. This setup was similar to that in the strain calibration experiment, but the strain gauges were removed and replaced by heating foils surrounding the cylindrical and feeder parts of the specimen. With the NTC sensor, the connected PID controller, and the heating foils, the temperature of the specimen was controlled to be stabilized at temperatures of 25 °C, 30 °C, 40 °C, 50 °C, 60 °C, 70 °C, and 80 °C. Extra insulation foam was used to cover the heating region to improve the temperature homogeneity and stability. At each controlled temperature level, loading and unloading steps
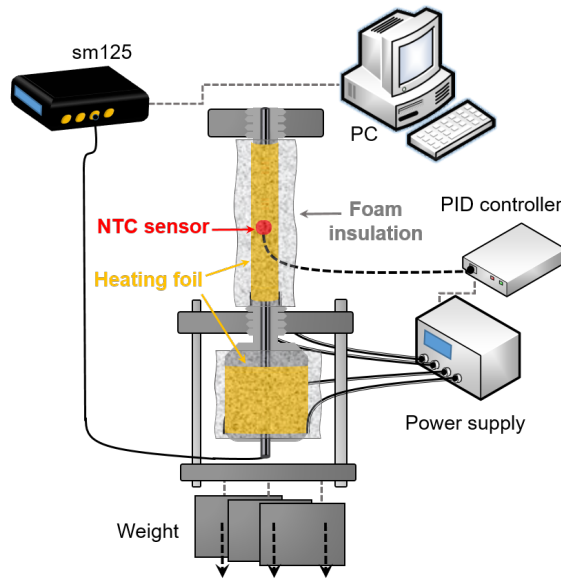


Figure 6.22: Schematic diagram of the temperature and strain measurement experiment.

mentioned in Section 6.3.2 were performed. As an example, Fig. 6.23(a) and 6.23(b) show the Bragg wavelengths of FBG($T$, $\varepsilon$), FBG($T$)-1, and FBG($T$)-2 during three strain cycles at a temperature of 80 °C, respectively. As seen in Fig. 6.23(a), the Bragg wavelength of FBG($T$, $\varepsilon$) changed as time owing to the loading and unloading steps, while, in Fig. 6.23(b), the Bragg wavelengths of FBG($T$)-1 and FBG($T$)-2 remained constant, revealing that FBG($T$)s were independent to strain and the temperature environment provided by the heating foils was stable. The temperature values were calculated based on Eq. 6.22, and the external strain values were decoupled from the temperature and
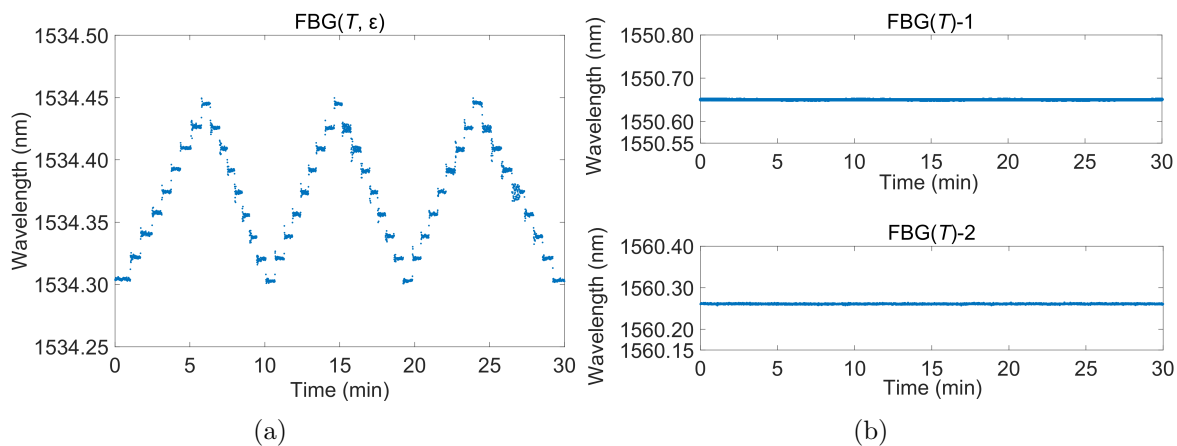
Figure 6.23: Bragg wavelength variation of (a) FBG($T$, $\varepsilon$), (b) FBG($T$)-1 and FBG($T$)-2 during the strain cycles at 80 ℃.

thermal strain in FBG($T$, $\varepsilon$) according to Eq. 6.21. The reference temperature was from the NTC sensor, while the reference strain was based on the theoretical calculations according to Eq. 6.19, respectively. Fig. 6.24(a) shows the strain obtained by FBG sensors and by reference at different temperatures, while Fig. 6.24(b) shows the FBG measured temperature and reference temperature at different strains. The black line represents the linear function when FBG measured value is equal to the reference value. To better show the decoupled temperature and strain at the same time, Fig. 6.24(c) is plotted, where the red cross symbols represent the measured values from FBG sensors and black circle symbols represent the reference values. The results show that the temperature and strain values obtained from the embedded FBG sensors agreed well with the reference values, revealing the good multiparameter monitoring capability of the embedded FBG sensors. The difference between the measured values and the reference values are within $\pm 5$ $\mu\varepsilon$ for external strain and $\pm 1$ ℃ for temperature.

The main reason for the difference between measured values and reference values might come from the limitation of the heating foil because it has been found that there was a slight temperature difference between the surface and the interior of the specimen. According to the decoupling method in Eq. 6.21, this temperature difference would lead to a strain deviation, especially in this case where the temperature sensitivity of FBG($T$, $\varepsilon$) was much higher than its external strain sensitivity. Our custom-built setup can only provide the external strains up to 110 $\mu\varepsilon$, while in some real applications like the tensile tests in Section 6.2, typical tensile strains can be more than one order of magnitude higher, so the strain difference ($\pm 5$ $\mu\varepsilon$) would be small enough. Therefore, it is believed that our embedded FBG sensors show a good performance in providing temperature and external strain information.
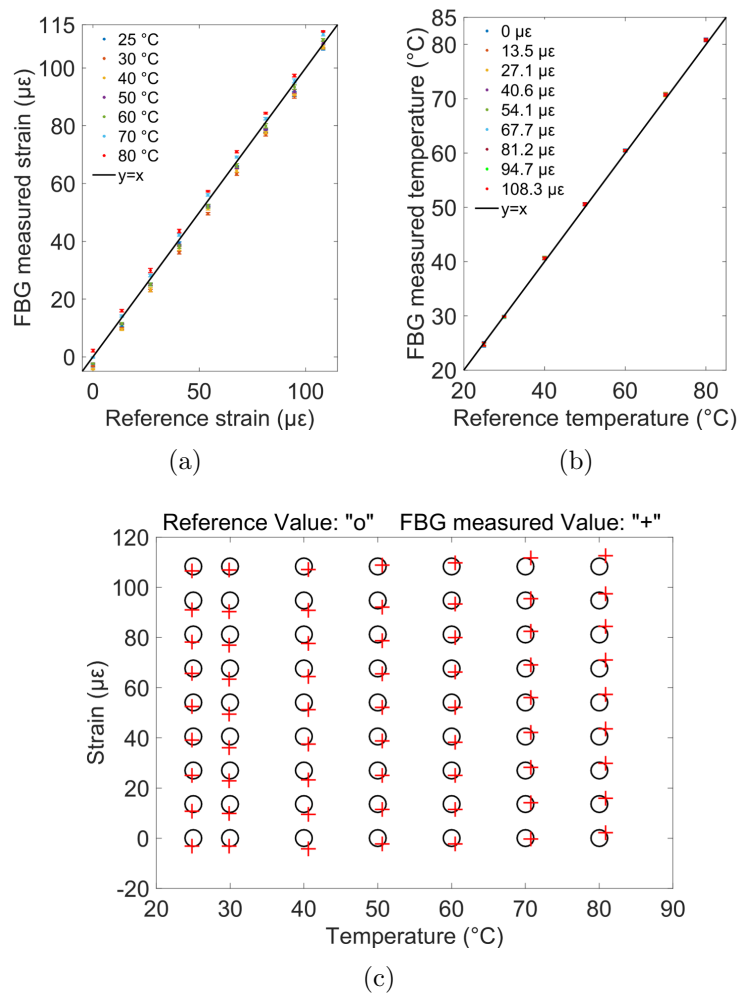
Figure 6.24: (a) Strain measured by FBG sensors at different temperatures. (b) Temperature measured by FBG sensors at different strains. (c) Reference values (circles) and measured values (crosses) obtained from FBG sensors at different temperatures and strains.

This research demonstrated that embedded FBG sensors could be a promising method for in-situ SHM of metallic cast structures. Temperature and external strain can be measured inside a cast part by a single sensing fiber, representing an important step towards fiber optic smart casts. More sensing points with tens of FBGs can be achieved due to the multiplexing ability, which allows extending the SHM capability of the fiber optic system to complex metallic structures. Besides, during the casting manufacturing process itself, the optical sensors can be embedded deeply inside the metallic structures, and no additional additive manufacturing process is needed, which shows potential for mass manufacturing. Further research could be carried out to extend the measured range of temperature and strain, which would expand the application scenarios. SHM of other

metallic materials, such as copper and steel, and other physical parameters, such as humidity and vibration, could also be further investigated.

# Chapter 7

# Summary

RFBGs, as one of the high-temperature resistant FBGs with the best performance, have been investigated in this thesis. By fabricating RFBGs in LMA fibers, the influence of dopant concentration on temperature sensitivity and wavelength drift rate has been studied. Standardized temperature calibration processes show that the temperature sensitivity of the RFBG in SMF-28 fiber was slightly higher than that of the RFBG in LMA fibers because of the higher dopant concentration and the larger CTE of the SMF-28 fiber core. 48-hour isothermal regeneration and annealing processes at 900 °C showed that drift rates of RFBGs in SMF-28 and LMA fibers were ~5.76 pm/h and ~3.78 pm/h, respectively. Thermal stress relaxation might be the dominant factor for the wavelength drift of RFBGs. Based on the calculation in Section 4.1.2, the thermal stress of the SMF-28 fiber was much larger than those of the LMA fibers. During the annealing process, the thermal stresses inside fibers were gradually relaxed, and the fiber with larger thermal stress exhibited a higher drift rate. A long-term stability test has been carried out at 600 °C for two years. The reflective powers of three RFBGs showed almost no change for all the RFBGs. The wavelength drift of the RFBG in SMF-28 showed a monotonous increase with a drift rate of 0.243 nm/year (0.0277 pm/h) and reached a saturated level after 250 days. There was almost no change in the wavelength drift for the RFBG in SMF-28 during the last 100 days. The final wavelength drift after one year was +0.16 nm. While, the drift behaviors of the RFBGs in LMA fibers showed a sudden change during the test: the drift rates were relatively low at the first 100 days, whose values were 0.058 nm/year (0.0066 pm/h) and 0.073 nm/year (0.0083 pm/h) for two LMA fibers, respectively. After 110- 130 days, the drift rates suddenly increased, which were 0.407 nm/year (0.0464 pm/h) and 0.329 nm/year (0.0376 pm/h), respectively. After 300 days, the wavelength drifts of the RFBGs in LMA fibers also reached saturated levels. The final wavelength drifts after one year were +0.12 nm and +0.14 nm, respectively. The

results showed that, for reflectivity, RFBG would not decay at temperatures of 600 ℃ and RFBG temperature sensors could work over long-term periods at least up to this temperature level; for wavelength drift, the RFBGs in LMA fibers have obviously lower wavelength drift and improved long-term functionality when the total working time is less than 100 days at 600 ℃. A series of comparative experiments on RFBG and SFBG were carried out to compare their difference and respective strengths and weaknesses. There was no drift observed for SFBG during the 48-hour annealing process at 900 ℃. Two temperature calibration processes were carried out, one from room temperature to 800 ℃ and one from room temperature to 1200 ℃. The temperature sensitivity of SFBG was found to be much larger than RFBG due to the higher CTE of sapphire. Both RFBG and SFBG showed good high-temperature sensing performance at temperatures lower than 1000 ℃. While, when the temperature exceeded 1000 ℃, the drift rate of RFBG increased significantly as temperature until 1200 ℃ when silica fibers drastically changed their properties and could no longer be used for temperature sensing. It should be noticed that the spectrum of SFBG is complicated due to the multimode issue, and the unclad structure makes SFBG very sensitive. As a comparison, RFBG has the advantages of low cost, simple fabrication, multiplexing capacity and easy calibration. Therefore, for application scenarios where the temperature is lower than 1000 ℃, and a large number of sensors are required, RFBG should be the optimal choice.

RFBG arrays fabricated in LMA fibers have been used to monitor temperature and strain during the AlSi9Cu3 aluminum casting process. The temperature evolution and distribution were measured with an array with RFBG($T$)s in a single fiber protected in a capillary. The strain evolution at each position has been decoupled from the temperature in the RFBG($T$, $\varepsilon$)s using the temperature information provided by the corresponding RFBG($T$)s. The results showed a high degree of correlation between the solidification phases of the aluminum alloy and the strain behavior during casting. The rigidity point and some solidification reactions were found to correspond to small temperature ranges. The gradient strain distribution at constant temperatures after solidification, which might be related to the residual stresses caused by the casting mold of this design, has been further revealed. The final compressive strain reached values over -10000 $\mu\varepsilon$ due to the shrinkage of the aluminum alloy. The findings showed that our RFBG-based casting monitoring method could provide a new perspective to study the solidification characteristics of metal alloys. Besides, casting monitoring was extended from aluminum alloy to copper alloy. The maximum temperature was up to 1100 ℃, and the largest compressive strain reached approximately -14000 $\mu\varepsilon$. The temperature obtained from RFBG($T$) agreed well with that from the reference thermocouple at the same position at high temperatures. After the cast parts cooled down to room temperature, permanent Bragg wavelength red drift caused by the relaxation effect led to a temperature information deviation in the

order of 17.3 ℃. Further work in casting monitoring can be done in the field of transverse strain distribution monitoring and casting of various metal alloys.

FBG sensors were embedded into aluminum and copper cast parts by casting. The actual embedding conditions were studied with the micrographs of the cross-sections, and the interaction between embedded fiber and metal at different temperatures was theoretically predicted with the shrink-fit model. A temperature response test was carried out for those RFBG($T$, $\varepsilon$)s embedded in aluminum and copper cast parts, with the first cycle from 0 ℃ to 120 ℃ and the second cycle from 0 ℃ to 180 ℃. In the first cycle, both RFBG($T$, $\varepsilon$)s worked well, while the RFBG($T$, $\varepsilon$) in the aluminum cast part showed a permanent wavelength drift when the temperature was over 120 ℃ in the second cycle. The drift rates were 28.1 pm/h at 160 ℃ and 71.9 pm/h at 180 ℃, while no obvious drift for the RFBG($T$, $\varepsilon$) in copper cast part even at the highest temperature of 180 ℃. The possible reason for the permanent drift in the aluminum cast part might be the relaxation of the thermal stress caused by the material property mismatch between aluminum alloy and silica fiber, and also the artificial aging of aluminum alloy, which was normally in the temperature range of 100-200 ℃. The shrink-fit model could be applied to well predict the Bragg wavelength changes of RFBG($T$, $\varepsilon$) embedded in the aluminum cast part when the permanent drift was ignored, while there was a big deviation between the theoretical and experimental results in the copper cast part. The possible reason might be that the boundary condition between copper and fiber might have changed due to the transition region caused by ultra-high temperatures in copper casting. In addition, the results of the wavelength change of RFBG($T$, $\varepsilon$)s in the temperature response test agreed well with that in the casting experiments. Several aluminum cast parts embedded with three FBG($T$, $\varepsilon$)s were further machined into tensile test specimens, and two tensile tests were carried out with the tensile test machine. The first tensile test consisted of two force cycles with the maximum force reaching 4000 N. The second tensile test had three cycles, and the maximum force reached 4500 N. The specimens in those two tensile tests experienced both elastic and plastic strains in the first cycles. The force range where no plastic strain occurs was extended afterward, and only elastic strains occurred in the following cycles. Work hardening effect might be the main cause of this behavior. The obtained k-factors of the FBG($T$, $\varepsilon$)s from the tensile tests were larger in the first cycles and smaller in the following cycles, and always the middle FBG($T$, $\varepsilon$)s showed the largest k-factor, the possible reason of which might be the less influence from the capillaries. A temperature and external strain decoupling method has been proposed for fiber-embedded metal structures. An optical fiber with two FBG($T$)s and one strain FBG($T$, $\varepsilon$) was embedded into an aluminum cast structure. The strain sensor FBG($T$, $\varepsilon$) was in direct contact with aluminum, while the adjacent placed temperature sensors FBG($T$)s were protected from strains by capillaries. A temperature calibration in a climatic chamber

from 0 to 80 °C and a strain calibration in a custom-built tensile test setup from 0 to $\sim$110 $\mu\varepsilon$ at room temperature were carried out respectively for the embedded sensors. The cross-sensitivity issue was well solved: external strain can be decoupled from the temperature and thermal strain in the FBG($T$, $\varepsilon$) using the interpolated temperature information provided by the FBG($T$)s. The temperature and strain values obtained from our embedded sensors agreed well with reference values.

In summary, the research in this thesis shows that RFBGs inscribed in LMA fibers exhibit better high-temperature sensing performance and can be applied in harsh environments like metal casting with the maximum temperature $\sim$1100 °C. The evolution and distribution of temperature and strain during aluminum and copper casting processes can be monitored by the fiber optic method, providing a new perspective to study the solidification characteristics of metal alloys. OFSs can be embedded into metal structures for in-situ SHM by casting. With a single embedded sensing fiber, temperature and external strain can be measured and decoupled, representing an important step towards fiber-optic smart casts.

For fiber optic smart casting, future research can be carried out to monitor transverse strain distribution, and to further reveal the correlation between the recorded strains and solidification characteristics and residual stresses. For fiber optic smart structures, OFSs can be further embedded into various metal alloys and achieve SHM of some industrial structures like induction engines and wind turbine blades.

# Appendix A

# Appendix

## A.1 List of Symbols

| | |
|---|---|
| $a$ | diameter of fiber core |
| $A_{core}$ | cross-sectional area of fiber core |
| $A_{clad}$ | cross-sectional area of fiber cladding |
| $A_j(z)$ | amplitude of the j-th mode transmitting along the forward (+z) direction |
| $b$ | diameter of fiber cladding |
| $B_j(z)$ | amplitude of the j-th mode transmitting along the backward (-z) direction |
| $E$ | Young's modulus |
| $E_{core}$ | Young's modulus of fiber core |
| $E_{clad}$ | Young's modulus of fiber cladding |
| $E_a$ | activation energy |
| $f_{rep}$ | repetition rate |
| $F$ | force; also, tension |
| $k_\varepsilon$ | relative strain sensitivity of FBG |
| $K_\varepsilon$ | strain sensitivity |
| $l$ | integer |
| $L$ | length |
| $M$ | number of fiber modes |
| $n_{core}$ | refractive index of fiber core |
| $n_{clad}$ | refractive index of fiber cladding |
| $n_{eff}$ | effective refractive index of fiber |
| NA | numerical aperture of fiber |
| $p_{ij}$ | elastic-optical coefficients |
| $R$ | reflectivity |

| | |
|---|---|
| $R_{max}$ | maximum reflectivity |
| $T$ | temperature |
| $T_g$ | glass transition temperature |
| $T_m$ | melting temperature |
| $V$ | normalized frequency |
| $V_s$ | scanning speed |
| $\alpha$ | CTE |
| $\alpha_{clad}$ | CTE of fiber cladding |
| $\beta$ | propagation constant |
| $\Delta$ | fractional refractive index change |
| $\Delta n_{AC}$ | strength of the refractive index modulation along z-axis (AC component) |
| $\Delta n_{DC}$ | mean value of the refractive index change (DC component) |
| $\Delta n_{eff}(z)$ | effective refractive index change |
| $\Delta T$ | temperature difference, also temperature change |
| $\Delta \lambda_0$ | bandwidth of FBG based on first zeros |
| $\Delta \lambda_{FWHM}$ | bandwidth of FBG based on FWHM |
| $\Delta \lambda_B(T)$ | temperature-induced Bragg wavelength change |
| $\Delta \lambda_B(\varepsilon)$ | strain-induced Bragg wavelength change |
| $\varepsilon_r$ | total radial strain |
| $\varepsilon_{rr}$ | pure radial strain |
| $\varepsilon_{zr}$ | transversal effect of axial strain |
| $\varepsilon_z$ | total axial strain |
| $\varepsilon_{zz}$ | pure axial strain |
| $\varepsilon_{rz}$ | transversal effect of radial strain |
| $\zeta$ | thermo-optic coefficient |
| $\theta_a$ | acceptance angle of fiber |
| $\kappa$ | "AC" coupling coefficient |
| $\lambda_B$ | Bragg wavelength |
| $\Lambda$ | grating period |
| $\nu$ | Poisson's ratio |
| $\nu_{fiber}$ | Poisson's ratio of fiber |
| $\rho$ | amplitude reflection coefficient |
| $\sigma$ | stress |
| $\sigma_{z,core}^m$ | axial mechanical stress in fiber core |
| $\sigma_{z,clad}^m$ | axial mechanical stress in fiber cladding |
| $\sigma_{z,core}^t$ | axial thermal stress in fiber core |
| $\sigma_{z,clad}^t$ | axial thermal stress in fiber cladding |
| $\hat{\sigma}$ | "DC" self-coupling coefficient |

## A.2   List of Abbreviations

| | |
|---|---|
| **CMT** | coupled-mode theory |
| **CTE** | coefficient of thermal expansion |
| **FBG** | fiber Bragg grating |
| **EFG** | edge-defined film-fed growth |
| **FWHM** | full width at half maximum |
| **fs-FBG** | femtosecond-laser-inscribed fiber Bragg grating |
| **GODC** | germanium oxygen deficient centers |
| **HF** | hydrogen-fluoride |
| **HWP** | half-wave plate |
| **LbL** | line-by-line |
| **LHPG** | laser-heated pedestal growth |
| **LMA** | large mode area |
| **LP** | linear polarizer |
| **MUAS** | Munich university of applied sciences |
| **NIR** | near infrared |
| **OFS** | optical fiber sensor |
| **PbP** | point-by-point |
| **PM** | polarization maintaining |
| **RFBG** | regenerated fiber Bragg grating |
| **SEM** | scanning electron microscope |
| **SHM** | structural health monitoring |
| **SFBG** | sapphire fiber Bragg grating |
| **TUM** | technical university of Munich |
| **UAM** | ultrasonic additive manufacturing |
| **UC** | ultrasonic consolidation |
| **UV** | ultraviolet |

## A.3   List of Tables

# A.4   List of Figures

# Bibliography

[1] Linjuan Yang. "The effect of casting temperature on the properties of squeeze cast aluminium and zinc alloys". In: *Journal of Materials Processing Technology* 140.1-3 (2003), pp. 391–396.

[2] Chandrashekhar M. Choudhari, Balkrishna E. Narkhede, and S.K. Mahajan. "Modeling and simulation with experimental validation of temperature distribution during solidification process in sand casting". In: *International Journal of Computer Applications* 78.16 (2013), pp. 23–29.

[3] Drew Nelson, Elizabeth Fuchs, Alberto Makino, and Adam D. Williams. "Residual-stress determination by single-axis holographic interferometry and hole drilling—Part II: Experiments". In: *Experimental Mechanics* 34.1 (1994), pp. 79–88.

[4] Matthias Reihle, Michael Hofmann, Uwe Wasmuth, Wolfram Volk, Hartmut Hoffmann, and Winfried Petry. "In situ strain measurements during casting using neutron diffraction". In: *Materials Science Forum*. Vol. 768. Trans Tech Publ. (2014), pp. 484–491.

[5] Jean-Marie Drezet, Bastien Mireux, Zoltan Szaraz, and Thilo Pirling. "In situ neutron diffraction during casting: determination of rigidity point in grain refined al-Cu alloys". In: *Materials* 7.2 (2014), pp. 1165–1172.

[6] Florian Heilmeier, Robert Koos, Peter Hornberger, Jochen Hiller, Klaus Weraneck, Martin Jakobi, Alexander W. Koch, and Wolfram Volk. "Calibration of cast-in fibre Bragg gratings for internal strain measurements in cast aluminium by using neutron diffraction". In: *Measurement* 163 (2020), p. 107939.

[7] Klaus Weraneck, Florian Heilmeier, Markus Lindner, Moritz Graf, Martin Jakobi, Wolfram Volk, Johannes Roths, and Alexander W. Koch. "Strain measurement in aluminium alloy during the solidification process using embedded fibre Bragg gratings". In: *Sensors* 16.11 (2016), p. 1853.

[8]   Markus Lindner, Edis Tunc, Klaus Weraneck, Florian Heilmeier, Wolfram Volk, Martin Jakobi, Alexander W. Koch, and Johannes Roths. "Regenerated Bragg grating sensor array for temperature measurements during an aluminum casting process". In: *IEEE Sensors Journal* 18.13 (2018), pp. 5352–5360.

[9]   S. Gowri and F.H. Samuel. "Effect of cooling rate on the solidification behavior of Al-7 Pct $Si - SiC_p$ metal-matrix composites". In: *Metallurgical and Materials Transactions A* 23 (1992), pp. 3369–3376.

[10]  J.O. Barlow and D.M. Stefanescu. "Computer-aided cooling curve analysis revisited". In: *Transactions-American Foundrymens Society* (1998), pp. 349–354.

[11]  Mile B. Djurdjevic and Gerhard Huber. "Determination of rigidity point / temperature using thermal analysis method and mechanical technique". In: *Journal of Alloys and Compounds* 590 (2014), pp. 500–506.

[12]  L. Arnberg, L. Bäckerud, and G. Chai. *Solidification characteristics of aluminum alloys.* Vol. 3: Dendrite Coherency. American Foundrymen's Society, (1996).

[13]  Nathalie Limodin, Luc Salvo, Elodie Boller, Michel Suéry, M Felberbaum, Sylvain Gailliègue, and Kamel Madi. "In situ and real-time 3-D microtomography investigation of dendritic solidification in an Al–10 wt.% Cu alloy". In: *Acta Materialia* 57.7 (2009), pp. 2300–2310.

[14]  Jean-Marie Drezet, Bastien Mireux, Zoltan Szaraz, and Thilo Pirling. "Determination of coherency and rigidity temperatures in Al-Cu alloys using in situ neutron diffraction during casting". In: *JOM* 66.8 (2014), pp. 1425–1430.

[15]  Ben De Pauw, Sidney Goossens, Thomas Geernaert, Dimitrios Habas, Hugo Thienpont, and Francis Berghmans. "Fibre Bragg gratings in embedded microstructured optical fibres allow distinguishing between symmetric and anti-symmetric lamb waves in carbon fibre reinforced composites". In: *Sensors* 17.9 (2017), p. 1948.

[16]  Mike Yeager, Michael Todd, William Gregory, and Chris Key. "Assessment of embedded fiber Bragg gratings for structural health monitoring of composites". In: *Structural Health Monitoring* 16.3 (2017), pp. 262–275.

[17]  C. Keulen, B. Rocha, M. Yildiz, and A. Suleman. "Embedded fiber optic sensors for monitoring processing, quality and structural health of resin transfer molded components". In: *Journal of Physics: Conference Series* 305 (2011), p. 012135.

[18]  Filippo Valvona, Jessica Toti, Vincenzo Gattulli, and Francesco Potenza. "Effective seismic strengthening and monitoring of a masonry vault by using glass fiber reinforced cementitious matrix with embedded fiber Bragg grating sensors". In: *Composites Part B: Engineering* 113 (2017), pp. 355–370.

[19] Robert Prussak, Daniel Stefaniak, Erik Kappel, Christian Hühne, and Michael Sinapius. "Smart cure cycles for fiber metal laminates using embedded fiber Bragg grating sensors". In: *Composite Structures* 213 (2019), pp. 252–260.

[20] Xiaochun Li and Fritz Prinz. "Metal embedded fiber Bragg grating sensors in layered manufacturing". In: *Journal of Manufacturing Science and Engineering* 125.3 (2003), pp. 577–585.

[21] Hamidreza Alemohammad and Ehsan Toyserkani. "Metal embedded optical fiber sensors: Laser-based layered manufacturing procedures". In: *Journal of Manufacturing Science and Engineering* 133.3 (2011).

[22] Dirk Havermann, Jinesh Mathew, William N. MacPherson, Duncan P. Hand, and Robert R.J. Maier. "Measuring residual stresses in metallic components manufactured with fibre Bragg gratings embedded by selective laser melting". In: *24th International Conference on Optical Fibre Sensors*. Vol. 9634. International Society for Optics and Photonics. (2015), 96340T.

[23] Dezhi Li and Rupert C Soar. "Plastic flow and work hardening of Al alloy matrices during ultrasonic consolidation fibre embedding process". In: *Materials Science and Engineering: A* 498.1-2 (2008), pp. 421–429.

[24] Xue Lan He, Zhen Qiang Wang, Dong Hui Wang, Xian Bin Wang, Yin Liu, Feng Chun Jiang, and Li Bo Yuan. "Optical fiber sensor for strain monitoring of metallic device produced by very high-power ultrasonic additive manufacturing". In: *IEEE Sensors Journal* 19.22 (2019), pp. 10680–10685.

[25] Chung E. Lee, Jorge J. Alcoz, William N. Gibler, Robert A. Atkins, and Henry Fuller Taylor. "Method for embedding optical fibers and optical fiber sensors in metal parts and structures". In: *Fiber Optic Smart Structures and Skins IV*. Vol. 1588. SPIE. (1991), pp. 110–116.

[26] Florian Heilmeier, Robert Koos, Klaus Weraneck, Markus Lindner, Martin Jakobi, Johannes Roths, Alexander W. Koch, and Wolfram Volk. "In-situ strain measurements in the plastic deformation regime inside casted parts using fibre-optical strain sensors: A contribution to the production of intelligent parts". In: *Production engineering* 13 (2019), pp. 351–360.

[27] Florian Heilmeier, Robert Koos, Michael Singer, Constantin Bauer, Peter Hornberger, Jochen Hiller, and Wolfram Volk. "Evaluation of strain transition properties between cast-in fibre Bragg gratings and cast aluminium during uniaxial straining". In: *Sensors* 20.21 (2020), p. 6276.

[28]   Markus Lindner, Andrea Stadler, Georg Hamann, Bennet Fischer, Martin Jakobi,
        Florian Heilmeier, Constantin Bauer, Wolfram Volk, Alexander W. Koch, and
        Johannes Roths. "Fiber Bragg sensors embedded in cast aluminum parts: axial
        strain and temperature response". In: *Sensors* 21.5 (2021), p. 1680.

[29]   Dirk Havermann, Jinesh Mathew, William N MacPherson, Robert RJ Maier, and
        Duncan P Hand. "Temperature and strain measurements with fiber Bragg gratings
        embedded in stainless steel 316". In: *Journal of Lightwave Technology* 33.12 (2014),
        pp. 2474–2479.

[30]   S. Triollet, L. Robert, E. Marin, and Y. Ouerdane. "Discriminated measures of
        strain and temperature in metallic specimen with embedded superimposed long
        and short fibre Bragg gratings". In: *Measurement Science and Technology* 22.1
        (2010), p. 015202.

[31]   Andrea Stadler, Markus Lindner, Qiang Bian, Georg Hamann, Constantin Bauer,
        Wolfram Volk, Martin Jakobi, Alexander W. Koch, and Johannes Roths. "Decou-
        pled temperature and strain measurement with regenerated fiber Bragg gratings
        during an aluminum casting process". In: *Sensors and Smart Structures Technolo-
        gies for Civil, Mechanical, and Aerospace Systems 2021*. Vol. 11591. International
        Society for Optics and Photonics. (2021), p. 115912D.

[32]   Turan Erdogan, Victor Mizrahi, Paul J. Lemaire, and Don Monroe. "Decay of
        ultraviolet-induced fiber Bragg gratings". In: *Journal of Applied Physics* 76.1
        (1994), pp. 73–80.

[33]   Dan Grobnic, Cyril Hnatovsky, Sergey Dedyulin, Robert B. Walker, Huimin Ding,
        and Stephen J. Mihailov. "Fiber Bragg grating wavelength drift in long-term high
        temperature annealing". In: *Sensors* 21.4 (2021), p. 1454.

[34]   Shuo Yang, Di Hu, and Anbo Wang. "Point-by-point fabrication and characteriza-
        tion of sapphire fiber Bragg gratings". In: *Optics Letters* 42.20 (2017), pp. 4219–
        4222.

[35]   Fedor Mitschke. *Fiber optics*. Springer, (2016).

[36]   Charles R. Kurkjian, Peter G. Simpkins, and Daryl Inniss. "Strength, degradation,
        and coating of silica lightguides". In: *Journal of the American Ceramic Society* 76.5
        (1993), pp. 1106–1112.

[37]   Y. Liao and M. Li. *Fiber optics*. Beijing, Tsinghua University Press, (2000).

[38]   *Characteristics of a single-mode optical fibre and cable*. Standard G.652.D. ITU-T,
        (2016).

[39]    Corning. *Corning SMF-28 Ultra Optical Fiber.* `https : / / www . corning . com / media/worldwide/coc/documents/Fiber/product-information-sheets/PI-1424-AEN.pdf.` (2021).

[40]    Bahaa E.A. Saleh and Malvin Carl Teich. *Fundamentals of photonics.* John Wiley & Sons, (2019).

[41]    Xunsi Wang, Qiuhua Nie, Tiefeng Xu, and Liren Liu. "A review of the fabrication of optic fiber". In: *ICO20: Optical Design and Fabrication.* Ed. by James Breckinridge and Yongtian Wang. Vol. 6034. International Society for Optics and Photonics. SPIE, (2006), p. 60341D.

[42]    Andrew D. Yablon. "Optical and mechanical effects of frozen-in stresses and strains in optical fibers". In: *IEEE Journal of Selected Topics in Quantum Electronics* 10.2 (2004), pp. 300–311.

[43]    Michael R. Hutsel. *Characterization of the stress and refractive-index distributions in optical fibers and fiber-based devices.* Georgia Institute of Technology, (2011).

[44]    B.H. Kim, Y. Park, T.-J. Ahn, D.Y. Kim, B.H. Lee, Y. Chung, U.C. Paek, and W.-T. Han. "Residual stress relaxation in the core of optical fiber by $CO2$ laser irradiation". In: *Optics Letters* 26.21 (2001), pp. 1657–1659.

[45]    U.C. Paek and C.R. Kurkjian. "Calculation of cooling rate and induced stresses in drawing of optical fibers". In: *Journal of the American Ceramic Society* 58.7-8 (1975), pp. 330–335.

[46]    D.A. Krohn and A.R. Cooper. "Strengthening of glass fibers: I, cladding". In: *Journal of the American Ceramic Society* 52.12 (1969), pp. 661–664.

[47]    Kok-Sing Lim, Hang-Zhou Yang, Wu-Yi Chong, Yew-Ken Cheong, Chin-Hong Lim, Norfizah M. Ali, and Harith Ahmad. "Axial contraction in etched optical fiber due to internal stress reduction". In: *Optics Express* 21.3 (2013), pp. 2551–2562.

[48]    M. Cavillon, P.D. Dragic, and J. Ballato. "Additivity of the coefficient of thermal expansion in silicate optical fibers". In: *Optics Letters* 42.18 (2017), pp. 3650–3653.

[49]    L-Y Shao, John Canning, Tao Wang, Kevin Cook, and H-Y Tam. "Viscosity of silica optical fibres characterized using regenerated gratings". In: *Acta Materialia* 61.16 (2013), pp. 6071–6081.

[50]    M. John Matthewson and Charles R. Kurkjian. "Environmental effects on the static fatigue of silica optical fiber". In: *Journal of the American Ceramic Society* 71.3 (1988), pp. 177–183.

[51] Peter J. Lezzi, Erin E. Evke, Emily M. Aaldenberg, and Minoru Tomozawa. "Surface crystallization and water diffusion of silica glass fibers: Causes of mechanical strength degradation". In: *Journal of the American Ceramic Society* 98.8 (2015), pp. 2411–2421.

[52] R Le Parc, C Levelut, J Pelous, V Martinez, and B Champagnon. "Influence of fictive temperature and composition of silica glass on anomalous elastic behaviour". In: *Journal of Physics: Condensed Matter* 18.32 (2006), p. 7507.

[53] Yu Zheng and Shubin Wang. "Effect of moderately high temperature heat treatment on surface morphology and structure of quartz fibers". In: *Applied surface science* 258.10 (2012), pp. 4698–4701.

[54] F.E. Wagstaff. "Crystallization and melting kinetics of cristobalite". In: *Journal of the American Ceramic Society* 52.12 (1969), pp. 650–654.

[55] O.V. Mazurin, V.K. Leko, and L.A. Komarova. "Crystallization of silica and titanium oxide-silica corning glasses (codes 7940 and 7971)". In: *Journal of Non-Crystalline Solids* 18.1 (1975), pp. 1–9.

[56] Vitreous Silica, F.E. Wagstaff, and K.J. Richards. "Preparation and crystallization behavior of oxygen-deficient". In: *Journal of the American Ceramic Society* 48.7 (1965), pp. 382–383.

[57] F.E. Wagstaff and K.J. Richards. "Kinetics of crystallization of stoichiometric SiO2 glass in H2O atmospheres". In: *Journal of the American Ceramic Society* 49.3 (1966), pp. 118–121.

[58] Franz Josef Dutz. "Faseroptische Multipunkt-Sensornetzwerke zur Messung von Hochtemperaturverteilungen in Gasturbinen und chemischen Reaktoren". PhD thesis. Technical University of Munich, (2022).

[59] Clarence L. Babcock, Stephen W. Barber, and Kasimir Fajans. "Coexisting structures in vitreous silica". In: *Industrial & Engineering Chemistry* 46.1 (1954), pp. 161–166.

[60] SAM Spinner. "Elastic moduli of glasses at elevated temperatures by a dynamic method". In: *Journal of the American Ceramic Society* 39.3 (1956), pp. 113–118.

[61] Markus Lindner. "Hochtemperatur-Sensorik mittels regenerierten Faser-Bragg-Gittern im Aluminiumguss". PhD thesis. Technical University of Munich, (2022).

[62] Michael I. Ojovan. "Viscosity and glass transition in amorphous oxides". In: *Advances in Condensed Matter Physics* 2008 (2008).

[63] Robert H. Doremus. "Viscosity of silica". In: *Journal of Applied Physics* 92.12 (2002), pp. 7619–7629.

[64] Bjorn Mysen and Pascal Richet. *Silicate glasses and melts*. Elsevier, (2018).

[65] P.A. Pajaczkowska, P. Reiche, D. Klimm, and G. Majumdar. "MgO, MgAl2O4, $\alpha$-Al2O3, LiAlO2, LiGaO2, NdGaO3, and SrLaGaO4: Bulk Growth". In: *Reference Module in Materials Science and Materials Engineering*. Elsevier, (2017).

[67] Rick K. Nubling and James A. Harrington. "Optical properties of single-crystal sapphire fibers". In: *Applied optics* 36.24 (1997), pp. 5934–5940.

[66] H.E. LaBelle. "EFG, the invention and application to sapphire growth". In: *Journal of Crystal Growth* 50.1 (1980), pp. 8–17.

[68] RefractiveIndex.INFO. *Optical constants of CRYSTALS Sapphire (Al2O3)*. `https://refractiveindex.info/?shelf=3d&book=crystals&page=sapphire`. (2022).

[69] Irving H. Malitson and Marilyn J. Dodge. "Refractive-index and birefringence of synthetic sapphire". In: *Journal Of The Optical Society Of America*. Vol. 62. 11. (1972), pp. 1405–1405.

[70] LASER COMPONENTS GmbH. *Single Crystal Sapphire Optical Fiber*. `https://www.lasercomponents.com/fileadmin/user_upload/home/Datasheets/diverse-fiber-optics/safir.pdf`. (2021).

[71] Turan Erdogan. "Fiber grating spectra". In: *Journal of Lightwave Technology* 15.8 (1997), pp. 1277–1294.

[72] Wei-Ping Huang. "Coupled-mode theory for optical waveguides: an overview". In: *JOSA A* 11.3 (1994), pp. 963–983.

[73] H. Kogelnik. "Theory of optical waveguides". In: *Guided-wave optoelectronics*. Springer, (1988), pp. 7–88.

[74] Amnon Yariv. "Coupled-mode theory for guided-wave optics". In: *IEEE Journal of Quantum Electronics* 9.9 (1973), pp. 919–933.

[75] Sema Kurtaran and M. Selami Kılıçkaya. "The modelling of fiber Bragg grating". In: *Optical and quantum electronics* 39.8 (2007), pp. 643–650.

[76] Andreas Othonos. "Fiber Bragg gratings". In: *Review of Scientific Instruments* 68.12 (1997), pp. 4309–4341.

[77] Johannes Roths and Florian Jülich. "Determination of strain sensitivity of free fiber Bragg gratings". In: *Optical Sensors 2008*. Vol. 7003. International Society for Optics and Photonics. (2008), p. 700308.

[78] Markus Lindner, Daniel Bernard, Florian Heilmeier, Martin Jakobi, Wolfram Volk, Alexander W. Koch, and Johannes Roths. "Transition from purely elastic to viscoelastic behavior of silica optical fibers at high temperatures characterized using regenerated Bragg gratings". In: *Optics Express* 28.5 (2020), pp. 7323–7340.

[79]  Matthieu Lancry and Bertrand Poumellec. "UV laser processing and multiphoton absorption processes in optical telecommunication fiber materials". In: *Physics Reports* 523.4 (2013), pp. 207–229.

[80]  Raman Kashyap. *Fiber bragg gratings*. Academic press, (2009).

[81]  M.G. Sceats, G.R. Atkins, and S.B. Poole. "Photolytic index changes in optical fibers". In: *Annual Review of Materials Science* 23.1 (1993), pp. 381–410.

[82]  Linards Skuja. "Optically active oxygen-deficiency-related centers in amorphous silicon dioxide". In: *Journal of NON-crystalline Solids* 239.1-3 (1998), pp. 16–48.

[83]  Leonhard Polz. "Regenerieren von Faser-Bragg-Gittern in polarisationserhaltenden optischen Fasern". PhD thesis. Friedrich Schiller University, (2017).

[84]  James F. Shackelford. "Gas solubility in glasses: Principles and applications". In: *International Journal of Applied Glass Science* 2.2 (2011), pp. 85–95.

[85]  Paul J. Lemaire, R.M. Atkins, V. Mizrahi, and W.A. Reed. "High pressure H2 loading as a technique for achieving ultrahigh UV photosensitivity and thermal sensitivity in GeO2 doped optical fibres". In: *Electronics Letters* 13.29 (1993), pp. 1191–1193.

[86]  Leonhard Polz, Andreas Dörfler, Hartmut Bartelt, and Johannes Roths. "Regeneration experiments with fibre Bragg gratings in hydrogen out-diffused fibres". In: *23rd International Conference on Optical Fibre Sensors*. Vol. 9157. SPIE. (2014), pp. 1057–1060.

[87]  Wikipedia. *Phase diagram*. https://en.wikipedia.org/wiki/Phase_diagram. (2022).

[88]  Micorr. *The nature of metals*. https://micorr.org/scientific-bases/. (2022).

[89]  Ben Best. *Lessons for Cryonics from Metallurgy and Ceramics*. https://benbest.com/cryonics/lessons.html. (1990).

[90]  Mohammadreza Zamani. "Al-Si Cast alloys-microstructure and mechanical properties at ambient and elevated temperatures". PhD thesis. Jönköping University, School of Engineering, (2017).

[91]  Charlie Sanabria. "A new understanding of the heat treatment of Nb-Sn superconducting wires". PhD thesis. Florida State University, (2017).

[92]  Magdalena Jablonska, Tomasz Maciag, Marian Nowak, Tomasz Rzychon, Monika Czerny, and Karolina Kowalczyk. "Thermal and structural analysis of high-tin bronze of chemical composition corresponding to the composition of the singing bowl". In: *Journal of Thermal Analysis and Calorimetry* 137 (2019), pp. 735–741.

[93]    Leonhard Polz, Franz J. Dutz, Robert R.J. Maier, Hartmut Bartelt, and Johannes Roths. "Regenerated fibre Bragg gratings: A critical assessment of more than 20 years of investigations". In: *Optics & Laser Technology* 134 (2021), p. 106650.

[94]    Michael A. Fokine, Bengt E. Sahlgren, and Raoul Stubbe. "A novel approach to fabricate high-temperature resistant fiber Bragg gratings". In: *Bragg Gratings, Photosensitivity, and Poling in Glass Fibers and Waveguides*. Optica Publishing Group. (1997), BSuD–5.

[95]    Michael Fokine. "Growth dynamics of chemical composition gratings in fluorine-doped silica optical fibers". In: *Optics Letters* 27.22 (2002), pp. 1974–1976.

[96]    Michael Fokine. "Thermal stability of oxygen-modulated chemical-composition gratings in standard telecommunication fiber". In: *Optics Letters* 29.11 (2004), pp. 1185–1187.

[97]    John Canning, Michael Stevenson, Somnath Bandyopadhyay, and Kevin Cook. "Extreme silica optical fibre gratings". In: *Sensors* 8.10 (2008), pp. 6448–6452.

[98]    Jing-Jing Zhu, A Ping Zhang, Bin Zhou, Feng Tu, Jiang-Tao Guo, Wei-Jun Tong, Sailing He, and Wei Xue. "Effects of doping concentrations on the regeneration of Bragg gratings in hydrogen loaded optical fibers". In: *Optics Communications* 284.12 (2011), pp. 2808–2811.

[99]    S. Bandyopadhyay, J. Canning, P. Biswas, M. Stevenson, and K. Dasgupta. "A study of regenerated gratings produced in germanosilicate fibers by high temperature annealing". In: *Optics Express* 19.2 (2011), pp. 1198–1206.

[100]   J. Canning, J. Fenton, and M. Stevenson. "Ultra-strong regenerated gratings". In: *2009 14th OptoElectronics and Communications Conference*. IEEE. (2009), pp. 1–2.

[101]   Tao Wang, Li-Yang Shao, John Canning, and Kevin Cook. "Regeneration of fiber Bragg gratings under strain". In: *Applied optics* 52.10 (2013), pp. 2080–2085.

[102]   Mert Celikin, David Barba, Binod Bastola, Andreas Ruediger, and Federico Rosei. "Development of regenerated fiber Bragg grating sensors with long-term stability". In: *Optics Express* 24.19 (2016), pp. 21897–21909.

[103]   Somnath Bandyopadhyay, John Canning, Michael Stevenson, and Kevin Cook. "Ultrahigh-temperature regenerated gratings in boron-codoped germanosilicate optical fiber using 193 nm". In: *Optics Letters* 33.16 (2008), pp. 1917–1919.

[104]   Karima Chah, Kivilcim Yüksel, Damien Kinet, Nazila Safari Yazd, Patrice Mégret, and Christophe Caucheteur. "Fiber Bragg grating regeneration at 450 C for improved high temperature sensing". In: *Optics Letters* 44.16 (2019), pp. 4036–4039.

[105]  Mattias L Åslund, John Canning, Albert Canagasabey, Roberson Assis de Oliveira, Yang Liu, Kevin Cook, and Gang-Ding Peng. "Mapping the thermal distribution within a silica preform tube using regenerated fibre Bragg gratings". In: *International Journal of Heat and Mass Transfer* 55.11-12 (2012), pp. 3288–3294.

[106]  Paula Rinaudo, Benjamín Torres, Ignacio Paya-Zaforteza, Pedro A. Calderón, and Salvador Sales. "Evaluation of new regenerated fiber Bragg grating high-temperature sensors in an ISO 834 fire test". In: *Fire Safety Journal* 71 (2015), pp. 332–339.

[107]  E. Haddad, R.V. Kruzelecky, K. Tagziria, B. Aissa, Iain McKenzie, A. Guelhan, J-M Muylaert, Mert Celinkin, and David Barba. "High temperature optical fiber sensor for atmospheric reentry". In: *International Conference on Space Optics—ICSO 2016*. Vol. 10562. SPIE. (2017), pp. 275–283.

[108]  Nélia Alberto, Hypolito José Kalinowski, Victor Neto, and Rogério Nogueira. "Diamond-coated fiber Bragg grating through the hot filament chemical vapor process for chemical durability improvement". In: *Applied Optics* 56.6 (2017), pp. 1603–1609.

[109]  Yann Corre, Guillaume Laffont, Christine Pocheau, Romain Cotillard, Jonathan Gaspar, Nicolas Roussel, Mehdi Firdaouss, J-L Gardarein, Dominique Guilhem, and Marc Missirlian. "Integration of fiber Bragg grating temperature sensors in plasma facing components of the WEST tokamak". In: *Review of Scientific Instruments* 89.6 (2018), p. 063508.

[110]  Franz J. Dutz, Andreas Heinrich, Rolf Bank, Alexander W. Koch, and Johannes Roths. "Fiber-optic multipoint sensor system with low drift for the long-term monitoring of high-temperature distributions in chemical reactors". In: *Sensors* 19.24 (2019), p. 5476.

[111]  Franz J. Dutz, Markus Lindner, Andreas Heinrich, Carl G Seydel, Thomas Bosselmann, Alexander W. Koch, and Johannes Roths. "Multipoint high temperature sensing with regenerated fiber Bragg gratings". In: *Fiber Optic Sensors and Applications XV*. Vol. 10654. International Society for Optics and Photonics. (2018), p. 1065407.

[112]  Franz J. Dutz, Sven Boje, Ulrich Orth, Alexander W. Koch, and Johannes Roths. "High-temperature profile monitoring in gas turbine exhaust-gas diffusors with six-point fiber-optic sensor array". In: *International Journal of Turbomachinery, Propulsion and Power* 5.4 (2020), p. 25.

[113]   Leonhard Polz, Barbara Hopf, Andreas Jarsen, Michael Eitzenberger, Markus Lindner, Hartmut Bartelt, and Johannes Roths. "Regenerated Bragg gratings in panda fibers for simultaneous temperature and force measurements at high temperatures". In: *Journal of Lightwave Technology* 34.19 (2016), pp. 4550–4556.

[114]   Zixuan Li, Fengming Yu, Osamu Saito, and Yoji Okabe. "In-situ laser-ultrasonic visualization with the use of regenerated fiber Bragg grating sensors at elevated temperatures". In: *Mechanical Systems and Signal Processing* 188 (2023), p. 110007.

[115]   Rongzhang Chen, Aidong Yan, Mingshan Li, Tong Chen, Qingqing Wang, John Canning, Kevin Cook, and Kevin P. Chen. "Regenerated distributed Bragg reflector fiber lasers for high-temperature operation". In: *Optics Letters* 38.14 (2013), pp. 2490–2492.

[116]   Karol Wysokiński, Tomasz Stańczyk, Katarzyna Gibała, Tadeusz Tenderenda, Anna Ziołowicz, Mateusz Słowikowski, Małgorzata Broczkowska, and Tomasz Nasiłowski. "New methods of enhancing the thermal durability of silica optical fibers". In: *Materials* 7.10 (2014), pp. 6947–6964.

[117]   D. Varelas, D.M. Costantini, H.G. Limberger, and R.P. Salathe. "Fabrication of high-mechanical-resistance Bragg gratings in single-mode optical fibers with continuous-wave ultraviolet laser side exposure". In: *Optics Letters* 23.5 (1998), pp. 397–399.

[118]   Andrea Stadler, Fabian Buchfellner, Andreas Zeisberger, Martin Jakobi, Alexander W. Koch, and Johannes Roths. "Verification of the mechanical integrity of regenerated fiber Bragg gratings (RFBGs) by shaker tests for their use as high-temperature sensors in gas turbines". In: *Optical Fiber Sensors*. Optica Publishing Group. (2022), W4–33.

[119]   Guillaume Laffont, Romain Cotillard, Nicolas Roussel, Rudy Desmarchelier, and Stéphane Rougeault. "Temperature resistant fiber Bragg gratings for on-line and structural health monitoring of the next-generation of nuclear reactors". In: *Sensors* 18.6 (2018), p. 1791.

[120]   Alexis Méndez, Vincent P. Wnuk, Michael Fokine, Åsa Claesson, Lars-Erik Nilsson, Steve Ferguson, and Tom Graver. "Packaging process of fiber Bragg grating strain sensors for use in high-temperature applications". In: *Fiber Optic Sensor Technology and Applications IV*. Vol. 6004. SPIE. (2005), pp. 111–117.

[121]   Yun Tu, Shan-Tung Tu, and Yi-Hua Qi. "Thermal characteristics of silver-recoated regenerated grating sensors for high-temperature sensing". In: *22nd International Conference on Optical Fiber Sensors*. Vol. 8421. SPIE. (2012), pp. 872–875.

[122]  Yun Tu, Yi-Hua Qi, and Tung Shan Tu. "Fabrication and thermal characteristics of Ti-Ag-Ni coated regenerated grating sensors for high-temperature sensing". In: *Smart Sensor Phenomena, Technology, Networks, and Systems Integration 2013*. Vol. 8693. SPIE. (2013), pp. 57–63.

[123]  Jeffrey Juergens, Grigory Adamovsky, Ramakrishna Bhatt, Gregory Morscher, and Bertram Floyd. "Thermal evaluation of fiber Bragg gratings at extreme temperatures". In: *43rd AIAA Aerospace Sciences Meeting and Exhibit*. (2005), p. 1214.

[124]  Grigory Adamovsky, Rosemary Bramante, Jeffrey Mackey, A Holguin, Bertram Floyd, and H Chan. "Fiber Bragg based optical sensors for extreme temperatures". In: *Infotech@ Aerospace 2011*. (2011), p. 1576.

[125]  G. Laffont, R. Cotillard, and P. Ferdinand. "9000 hours-long high temperature annealing of regenerated fiber Bragg gratings". In: *Fifth European Workshop on Optical Fibre Sensors*. Vol. 8794. SPIE. (2013), pp. 305–308.

[126]  Yuhua Li, Minwei Yang, D.N. Wang, J. Lu, T. Sun, and KTV Grattan. "Fiber Bragg gratings with enhanced thermal stability by residual stress relaxation". In: *Optics Express* 17.22 (2009), pp. 19785–19790.

[127]  Man-Hong Lai, Kok-Sing Lim, Dinusha S. Gunawardena, Hang-Zhou Yang, Wu-Yi Chong, and Harith Ahmad. "Thermal stress modification in regenerated fiber Bragg grating via manipulation of glass transition temperature based on CO2-laser annealing". In: *Optics Letters* 40.5 (2015), pp. 748–751.

[128]  Dimitrios Polyzos, Jinesh Mathew, William N. MacPherson, and Robert R.J. Maier. "Effect of dopant diffusion on the long-term stability of Fabry–Pérot optical fiber sensors". In: *Journal of Lightwave Technology* 35.24 (2017), pp. 5317–5323.

[129]  Stephen J. Mihailov, Christopher W. Smelser, Dan Grobnic, Robert B. Walker, Ping Lu, Huimin Ding, and James Unruh. "Bragg gratings written in all-SiO2 and Ge-doped core fibers with 800-nm femtosecond radiation and a phase mask". In: *Journal of Lightwave Technology* 22.1 (2004), pp. 94–100.

[130]  Graham D. Marshall, Robert J. Williams, Nemanja Jovanovic, M.J. Steel, and Michael J. Withford. "Point-by-point written fiber-Bragg gratings and their application in complex grating designs". In: *Optics Express* 18.19 (2010), pp. 19844–19859.

[131]  Junji Nishii, Naoyuki Kitamura, Hiroshi Yamanaka, Hideo Hosono, and Hiroshi Kawazoe. "Ultraviolet-radiation-induced chemical reactions through one-and two-photon absorption processes in GeO2-SiO2 glasses". In: *Optics Letters* 20.10 (1995), pp. 1184–1186.

[132] Christopher W. Smelser, Stephen J. Mihailov, and Dan Grobnic. "Formation of Type I-IR and Type II-IR gratings with an ultrafast IR laser and a phase mask". In: *Optics express* 13.14 (2005), pp. 5377–5386.

[133] K. Miura Davis, Kiyotaka Miura, Naoki Sugimoto, and Kazuyuki Hirao. "Writing waveguides in glass with a femtosecond laser". In: *Optics Letters* 21.21 (1996), pp. 1729–1731.

[134] Eugene G. Gamaly, Saulius Juodkazis, Koichi Nishimura, Hiroaki Misawa, Barry Luther-Davies, Ludovic Hallo, Philippe Nicolai, and Vladimir T. Tikhonchuk. "Laser-matter interaction in the bulk of a transparent solid: Confined microexplosion and void formation". In: *Physical Review B* 73.21 (2006), p. 214101.

[135] Dan Grobnic, Christopher W. Smelser, Stephen J. Mihailov, and Robert B. Walker. "Long-term thermal stability tests at 1000 ℃ of silica fibre Bragg gratings made with ultrafast laser radiation". In: *Measurement Science and Technology* 17.5 (2006), p. 1009.

[136] Amós Martinez, IY Khrushchev, and Ian Bennion. "Thermal properties of fibre Bragg gratings inscribed point-by-point by infrared femtosecond laser". In: *Electronics letters* 41.4 (2005), pp. 176–178.

[137] Dan Grobnic, Stephen J Mihailov, Christopher W Smelser, and Huimin Ding. "Sapphire fiber Bragg grating sensor made using femtosecond laser radiation for ultrahigh temperature applications". In: *IEEE Photonics Technology Letters* 16.11 (2004), pp. 2505–2507.

[138] Xizhen Xu, Jun He, Changrui Liao, Kaiming Yang, Kuikui Guo, Chi Li, Yunfang Zhang, Zhengbiao Ouyang, and Yiping Wang. "Sapphire fiber Bragg gratings inscribed with a femtosecond laser line-by-line scanning technique". In: *Optics Letters* 43.19 (2018), pp. 4562–4565.

[139] Matthias Busch, Wolfgang Ecke, Ines Latka, Daniel Fischer, Reinhardt Willsch, and Hartmut Bartelt. "Inscription and characterization of Bragg gratings in single-crystal sapphire optical fibres for high-temperature sensor applications". In: *Measurement Science and Technology* 20.11 (2009), p. 115301.

[140] Qi Guo, Yong-Sen Yu, Zhong-Ming Zheng, Chao Chen, Peng-Long Wang, Zhen-Nan Tian, Yang Zhao, Xin-Yu Ming, Qi-Dai Chen, Han Yang, and Hong-Bo Sun. "Femtosecond laser inscribed sapphire fiber Bragg grating for high temperature and strain sensing". In: *IEEE Transactions on Nanotechnology* 18 (2019), pp. 208–211.

[141] Xizhen Xu, Jun He, Changrui Liao, and Yiping Wang. "Multi-layer, offset-coupled sapphire fiber Bragg gratings for high-temperature measurements". In: *Optics Letters* 44.17 (2019), pp. 4211–4214.

[142] Dan Grobnic, Stephen J. Mihailov, H. Ding, F. Bilodeau, and Christopher W. Smelser. "Single and low order mode interrogation of a multimode sapphire fibre Bragg grating sensor with tapered fibres". In: *Measurement Science and Technology* 17.5 (2006), p. 980.

[143] Chun Zhan, Jae Hun Kim, Jon E. Lee, Stuart Yin, Paul Ruffin, and Claire Luo. "High temperature sensing using higher-order-mode rejected sapphire-crystal fiber gratings". In: *Photonic Fiber and Crystal Devices: Advances in Materials and Innovations in Device Applications*. Vol. 6698. SPIE. (2007), pp. 100–107.

[144] Shuo Yang, Daniel Homa, Gary Pickrell, and Anbo Wang. "Fiber Bragg grating fabricated in micro-single-crystal sapphire fiber". In: *Optics Letters* 43.1 (2018), pp. 62–65.

[145] Qi Guo, Shanren Liu, Xuepeng Pan, Bo Wang, Zhennan Tian, Chao Chen, Qidai Chen, Yongsen Yu, and Hongbo Sun. "Femtosecond laser inscribed helical sapphire fiber Bragg gratings". In: *Optics Letters* 46.19 (2021), pp. 4836–4839.

[146] Joshua T. Jones, Anthony Birri, Thomas E. Blue, Dan Kominsky, Kelly McCary, Osgar John Ohanian, and S. Derek Rountree. "Light propagation considerations for internally clad sapphire optical fiber using the 6Li (n, $\alpha$) 3H reaction". In: *Journal of Lightwave Technology* 40.4 (2021), pp. 1181–1187.

[147] Mohan Wang, Patrick S. Salter, Frank P. Payne, Adrian Shipley, Stephen M. Morris, Martin J. Booth, and Julian A.J. Fells. "Single-mode sapphire fiber Bragg grating". In: *Optics Express* 30.9 (2022), pp. 15482–15494.

[148] Muhammad Roman, Damilola Balogun, Chen Zhu, Laura Bartlett, Ronald J. O'Malley, Rex E. Gerald, and Jie Huang. "Thermal mapping of metal casting mold using high-resolution distributed fiber-optic sensors". In: *IEEE Transactions on Instrumentation and Measurement* 70 (2021), pp. 1–10.

[149] Muhammad Roman, Damilola Balogun, Laura Bartlett, Ronald J. O'Malley, Rex E. Gerald, and Jie Huang. "Optical fiber temperature sensors embedded in a metal casting mold". In: *27th International Conference on Optical Fiber Sensors*. Optica Publishing Group. (2022), W4–43.

[150] Muhammad Roman, Damilola Balogun, Yiyang Zhuang, Rex E. Gerald, Laura Bartlett, Ronald J. O'Malley, and Jie Huang. "A spatially distributed fiber-optic temperature sensor for applications in the steel industry". In: *Sensors* 20.14 (2020), p. 3900.

[151]  B.G. Thomas and M.K. Okelman. "Implementation of temperature and strain micro-sensors into a casting mold surface". In: *Sensors, Sampling, and Simulation for Process Control*. John Wiley & Sons, (2011), pp. 127–134.

[152]  Dirk Lieftucht, Markus Reifferscheid, Thomas Schramm, Artemy Krasilnikov, and Dieter Kirsch. "HD mold—A new fiber-optical-based mold monitoring system". In: *Iron Steel Technol* 10 (2013), pp. 87–95.

[153]  Ton Spierings, Arnoud Kamperman, Herman Hengeveld, Jan Kromhout, and Edward Dekker. "Development and application of fiber Bragg gratings for slab casting". In: *Proceedings of the 2017 AISTech Conference, Nashville, TN, USA*. (2017), pp. 8–11.

[154]  Huaping Wang, Ping Xiang, and Lizhong Jiang. "Optical fiber sensor based in-field structural performance monitoring of multilayered asphalt pavement". In: *Journal of Lightwave Technology* 36.17 (2018), pp. 3624–3632.

[155]  Helmut Woschitz, Ferdinand Klug, and Werner Lienhart. "Design and calibration of a fiber-optic monitoring system for the determination of segment joint movements inside a hydro power dam". In: *Journal of Lightwave Technology* 33.12 (2014), pp. 2652–2657.

[156]  Chennan Hu, Zhihao Yu, and Anbo Wang. "An all fiber-optic multi-parameter structure health monitoring system". In: *Optics Express* 24.18 (2016), pp. 20287–20296.

[157]  Zhichun Fan, Xingzhong Diao, Malin Liu, Yong Zhang, Zhiyong Huang, and He Yan. "On-line monitoring of sealing glass in electrical penetration assembly based on femto-laser inscribed fiber Bragg grating sensors". In: *Optics Express* 27.2 (2019), pp. 608–620.

[158]  Laura Albero Blanquer, Florencia Marchini, Jan Roman Seitz, Nour Daher, Fanny Bétermier, Jiaqiang Huang, Charlotte Gervillié, and Jean-Marie Tarascon. "Optical sensors for operando stress monitoring in lithium-based batteries containing solid-state or liquid electrolytes". In: *Nature Communications* 13.1 (2022), pp. 1–14.

[159]  Matthew J. Nicolas, Rani W. Sullivan, and W. Lance Richards. "Large scale applications using FBG sensors: determination of in-flight loads and shape of a composite aircraft wing". In: *Aerospace* 3.3 (2016), p. 18.

[160]  Yen-Te Ho, Yu-Li Wang, Liang-Cheng Chang, Tzu-Pin Wang, and Jui-Pin Tsai. "Optical system for monitoring groundwater pressure and temperature using fiber Bragg gratings". In: *Optics Express* 29.11 (2021), pp. 16032–16045.

[161] D. White. *Ultrasonic object consolidation*. US Patent 6,519,500. (2003).

[162] Simona Masurtschak, Ross James Friel, Arnold Gillner, J Ryll, and RA Harris. "Fiber laser induced surface modification/manipulation of an ultrasonically consolidated metal matrix". In: *Journal of Materials Processing Technology* 213.10 (2013), pp. 1792–1800.

[163] Nouari Saheb and Samir Mekid. "Fiber-embedded metallic materials: From sensing towards nervous behavior". In: *Materials* 8.11 (2015), pp. 7938–7961.

[164] Tomasz Osuch, Alicja Anuszkiewicz, Dawid Zakrzewski, Adam Filipkowski, Jacek Olszewski, Paweł Mergo, Dariusz Pysz, Rafał Kasztelanic, and Ryszard Buczyński. "Enhancement of spectral response of Bragg gratings written in nanostructured and multi-stepped optical fibers with radially shaped GeO2 concentration". In: *Optics Express* 28.10 (2020), pp. 14774–14787.

[165] LIEKKI. *Large Mode Area Passive Fibers.* `https://static1.squarespace.com/static/5d5d8be5c16a590001b58605/t/5ee2574112206419c0ed9ef0/1591891778604/nLIGHT+LIEKKI+Large+Mode+Area+Passive+Fibers_2020.pdf`. (2020).

[166] Nguyen Hong Ky, Hans Georg Limberger, René Paul Salathé, François Cochet, and Liang Dong. "Hydrogen-induced reduction of axial stress in optical fiber cores". In: *Applied Physics Letters* 74.4 (1999), pp. 516–518.

[167] Georg Hamann. "Characterization of free and embedded RFBG sensors in a SM250 fiber". Project Study. Munich University of Applied Sciences, (2019).

[168] Dimitrios Polyzos, Jinesh Mathew, William N. MacPherson, and Robert R.J. Maier. "High temperature stability testing of Ge-doped and F-doped Fabry-Perot fibre optical sensors". In: *Sixth European Workshop on Optical Fibre Sensors.* Vol. 9916. SPIE. (2016), pp. 10–13.

[169] Stephen J. Mihailov, Dan Grobnic, and Christopher W. Smelser. "High-temperature multiparameter sensor based on sapphire fiber Bragg gratings". In: *Optics Letters* 35.16 (2010), pp. 2810–2812.

[170] Tino Elsmann, Tobias Habisreuther, Albrecht Graf, Manfred Rothhardt, and Hartmut Bartelt. "Inscription of first-order sapphire Bragg gratings using 400 nm femtosecond laser radiation". In: *Optics Express* 21.4 (2013), pp. 4591–4597.

[171] Tobias Habisreuther, Tino Elsmann, Zhiwen Pan, Albrecht Graf, Reinhardt Willsch, and Markus A. Schmidt. "Sapphire fiber Bragg gratings for high temperature and dynamic temperature diagnostics". In: *Applied Thermal Engineering* 91 (2015), pp. 860–865.

[172] *Aluminium and aluminium alloys-Castings—Chemical composition and mechanical properties.* Standard ISO 3522:2007. International Organization for Standardization, (2007).

[173] Eckart Doege and Bernd-Arno Behrens. *Handbuch Umformtechnik.* Springer, (2010).

[174] Florian Juelich and Johannes Roths. "OP2-determination of the effective refractive index of various single mode fibres for fibre Bragg grating sensor applications". In: *Proceedings OPTO 2009 & IRS² 2009* (2009), pp. 119–124.

[175] X Roselló-Mechó, M. Delgado-Pinar, A. Díez, and M.V. Andrés. "Measurement of Pockels' coefficients and demonstration of the anisotropy of the elasto-optic effect in optical fibers under axial strain". In: *Optics Letters* 41.13 (2016), pp. 2934–2937.

[176] European Copper Institute. *Copper-tin alloys tin bronzes phosphor bronzes CuSn2.* `https://copperalliance.eu/uploads/2018/03/cusn2.pdf`. (2018).

[177] N. Saunders and A.P. Miodownik. "The Cu-Sn (copper-tin) system". In: *Bulletin of Alloy Phase Diagrams* 11.3 (1990), pp. 278–287.

[178] Yulong Li, Zhang Hua, Feng Yan, and Peng Gang. "Metal coating of fiber Bragg grating and the temperature sensing character after metallization". In: *Optical Fiber Technology* 15.4 (2009), pp. 391–397.

[179] Y. Feng. "Study on sensing performance of fiber Bragg grating embedded in metal structures". PhD thesis. Nanchang University, (2009).

[180] Jianyu He, Liyun Ding, Jun Cai, Wenjie Zhu, and Jixiang Dai. "A novel high temperature resistant Mo-Cu functional gradient coating for optic fiber Bragg grating". In: *Results in Physics* 14 (2019), p. 102456.

[181] YC Zhou. "Solid mechanics in materials". In: Beijing, China: Science Press, (2005), pp. 157–160.

[182] S Timoshenko and JN Goodier. "Theory of Elasticity". In: *Inc. New York* (1951).

[183] Kenneth O. Hill and Gerald Meltz. "Fiber Bragg grating technology fundamentals and overview". In: *Journal of Lightwave Technology* 15.8 (1997), pp. 1263–1276.

[184] AK Dahle. "Aluminum Alloys, Heat Treatment of". In: *Encyclopedia of Materials: Science and Technology* (2011), pp. 111–113.

[185] MakeItFrom.com: Material Properties Database. *EN AC-46000 Cast Aluminum.* `https://www.makeitfrom.com/material-properties/EN-AC-46000-46000-F-AlSi9Cu3Fe-Cast-Aluminum`. (2020).

[186] German Copper Institute. *Material data sheets - CuSn4.* `https://www.kupferinstitut.de/wp-content/uploads/2019/11/CuSn4-1.pdf`. (2019).

[187]   *Testing of metallic materials - Tensile test pieces*. Standard DIN 50125:2016-12. DIN-Normenausschuss Materialprüfung, (2016).

[188]   Andrea Stadler. "Simultaneous temperature and strain measurement with fiber Bragg gratings in cast aluminum components". Masters Thesis. Munich University of Applied Sciences, (2020).

[189]   Wikipedia. *Work hardening.* `https://en.wikipedia.org/wiki/Work_hardening`. (2022).

[190]   Hottinger Baldwin Messtechnik GmbH. *Applying the Wheatstone Bridge Circuit - Technical Information.* `https://www.hbm.com/en/7163/wheatstone-bridge-circuit/`. (2022).

# Acknowledgment

# Publications

## Journal

1. **Q. Bian**, C. Bauer, A. Stadler, F. Buchfellner, M. Jakobi, W. Volk, A. W. Koch, and J. Roths, "Monitoring strain evolution and distribution during the casting process of AlSi9Cu3 alloy with optical fiber sensors," J. Alloy. Compd. 935, 168146 (2023)

2. **Q. Bian**, F. J. Dutz, M. Lindner, F. Buchfellner, A. Stadler, M. Jakobi, A. W. Koch, and J. Roths, "Regenerated Fiber Bragg Gratings in Large Mode Area Fibers for High-temperature Sensing," J. Light. Technol. (2023)

3. **Q. Bian**, A. Podhrazsky, C. Bauer, A. Stadler, F. Buchfellner, R. Kuttler, M. Jakobi, W. Volk, A. W. Koch, and J. Roths, "Temperature and external strain sensing with metal-embedded optical fiber sensors for structural health monitoring," Opt. Express 30, 33449–33464 (2022).

4. **Q. Bian**, C. Bauer, A. Stadler, M. Lindner, M. Jakobi, W. Volk, A. W. Koch, and J. Roths, "In-situ high temperature and large strain monitoring during a copper casting process based on regenerated fiber Bragg grating sensors," J. Light. Technol. 39, 6660–6669 (2021).

5. F. Buchfellner, **Q. Bian**, W. Hu, X. Hu, M. Yang, A. W. Koch, and J. Roths, "Temperature-decoupled hydrogen sensing with Pi-shifted fiber Bragg gratings and a partial palladium coating," Opt. Lett. 48, 73–76 (2023).

6. F. Buchfellner, A. Stadler, **Q. Bian**, M. Hennesen, A. Zeisberger, A. W. Koch, and J. Roths, "Generalized and wavelength-dependent temperature calibration function for multipoint regenerated fiber Bragg grating sensors," Opt. Express 30, 44769–44784 (2022).

7. J. Lu, Y. Yu, S. Qin, M. Li, **Q. Bian**, Y. Lu, X. Hu, J. Yang, Z. Meng, and Z. Zhang, "High-performance temperature and pressure dual-parameter sensor based on a polymer-coated tapered optical fiber," Opt. Express 30, 9714–9726227 (2022).

8. K. Wang, X. Dong, M. H. Köhler, P. Kienle, **Q. Bian**, M. Jakobi, and A. W. Koch, "Advances in optical fiber sensors based on multimode interference (MMI): a review," IEEE Sensors J. 21, 132–142 (2020).

9. D. Wang, Y. Yu, Z. Lu, J. Yang, Z. Yi, **Q. Bian**, J. Zhang, S. Qin, J. Weng, S. Yao, Y. Lu, X. Hu, and Z. Meng, "Design of photonic crystal fiber to excite surface plasmon resonance for highly sensitive magnetic field sensing," Opt. Express 30, 29271–29286 (2022).

10. J. Lu, Z. Zhang, Y. Yu, S. Qin, F. Zhang, M. Li, **Q. Bian**, M. Yin, and J. Yang, "Simultaneous Measurement of Seawater Temperature and Pressure With Poly-dimethylsiloxane Packaged Optical Microfiber Coupler Combined Sagnac Loop," J. Light. Technol. 40, 323–333 (2021).

11. X. Hu, W. Hu, J. Dai, H. Ye, F. Zhang, M. Yang, F. Buchfellner, **Q. Bian**, B. Hopf, and J. Roths, "Performance of Fiber-Optic Hydrogen Sensor Based on Locally Coated $\pi$-Shifted FBG," IEEE Sensors J. 22, 23982–23989 (2022).

12. D. Wang, Z. Yi, G. Ma, B. Dai, J. Yang, J. Zhang, Y. Yu, C. Liu, X. Wu, and **Q. Bian**, "Two-channel photonic crystal fiber based on surface plasmon resonance for magnetic field and temperature dual-parameter sensing," Phys. Chem. Chem. Phys. 24, 21233–21241 (2022).

## Conference

1. **Q. Bian**, C. Bauer, A. Stadler, F. Buchfellner, M. Jakobi, W. Volk, A. W. Koch, and J. Roths, "Investigation of strain behavior during aluminum casting process with regenerated fiber Bragg grating arrays," in Optical Fiber Sensors, (Optica Publishing Group, 2022), pp. W2–4.

2. **Q. Bian**, C. Bauer, A. Stadler, M. Jakobi, A. W. Koch, and J. Roths, "Multipoint temperature monitoring based on a regenerated fiber Bragg grating temperature sensor array in copper casting," in Sensors and Smart Structures Technologies for Civil, Mechanical, and Aerospace Systems 2021, vol. 11591 (SPIE, 2021), pp. 172–177.

3. A. Stadler, M. Lindner, **Q. Bian**, G. Hamann, C. Bauer, W. Volk, M. Jakobi, A. W. Koch, and J. Roths, "Decoupled temperature and strain measurement with regenerated fiber Bragg gratings during an aluminum casting process," in Sensors

and Smart Structures Technologies for Civil, Mechanical, and Aerospace Systems 2021, vol. 11591 (SPIE, 2021), pp. 482–488.

4. F. Buchfellner, S. Fiedler, M. Danalache, C. Daniel, **Q. Bian**, B. Trautwein, U. Hofmann, and J. Roths, "Micro-Indentation on Bovine and Human Cartilage with Phase-shifted Fiber Bragg Gratings in PM Fibers," in Optical Fiber Sensors, (Optica Publishing Group, 2022), pp. Th1–4.

5. K. Wang, X. Dong, M. H. Köhler, P. Kienle, **Q. Bian**, M. Fink, M. Jakobi, and A. W. Koch, "Optical fiber sensors based on multimode interference using square-core fiber for temperature measurement," in Photonic Instrumentation Engineering VIII, vol. 11693 (SPIE, 2021), pp. 120–126.